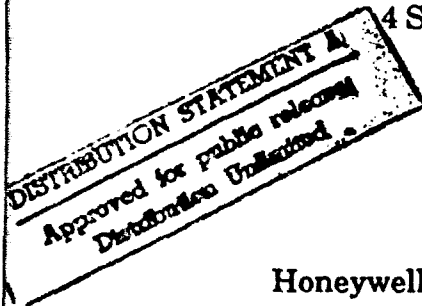AD-A260 589

|||||||||||||||||||||||||||||||

Final Report

Monolithic Integration of Semiconductor and Superconductor Components

Contract No. N00014-90-C-0226
ARPA Order No. 7534

4 September 1990 - 30 September 1992

DTIC
SELECTE
NOV 16 1992
B

Paul W. Kruse
Burgess R. Johnson

Honeywell Sensor and System Development Center
10701 Lyndale Avenue South
Bloomington, MN 55420

31 October 1992

The views and conclusions contained in this document are those of the authors and should not be interpreted as necessarily representing the official policies, either expressed or implied, of the Defense Advanced Projects Agency, Office of Naval Research or the U.S. Government.

92 11 13 013

92-29518
|||||||||||||||||||||||||||||

Final Report

Monolithic Integration of Semiconductor and Superconductor Components

Contract No. N00014-90-C-0226
ARPA Order No. 7534

4 September 1990 - 30 September 1992

Paul W. Kruse
Burgess R. Johnson

Honeywell Sensor and System Development Center
10701 Lyndale Avenue South
Bloomington, MN 55420

31 October 1992

The views and conclusions contained in this document are those of the authors and should not be interpreted as necessarily representing the official policies, either expressed or implied, of the Defense Advanced Projects Agency, Office of Naval Research or the U.S. Government.

Material Inspection and Receiving Report	1. Proc. Instrument Iden (Contract) N00014-90-C-0226	(Order) No.	6. Invoice No Date	7. Page 1 of 8. Acceptance Point

2. Shipment No.	3. Date Shipped	4. B/L. TCN	5. Discount Terms
	06 Nov 199_		

9. Prime Contractor	Code		10. Administered By	Code	

11. Shipped From (if other than 9)	Code	FOB:	12. Payment Will Be Made By	Code	
			DFAS Columbus Center DFAS Columbus Division PO Box 9225 Columbus, OH 47215-225		

13. Shipped To	Code		14. Marked For	Code	
Office of Naval Research Dept of the Navy 800 North Quincy St Arlington, VA 2221 7-5000			Wallace Smith Code Ref Contract N00014-90-C-0226		

15. Item No.	16. Stock/Part No. Description (Indicate number of shipping containers, type of container, container number)	17. Quantity Ship/Rec'd*	18. Unit	19. Unit Price	20. Amount
CLIN 000	Research to integrate semiconductor electronics with infrared sensors based on superconducting transition edge bolometers to make a 16 pixel 4x4 two-dimensional infrared staring array		LO		
CLIN 0002 Acct	Final Report		LO	NSP	0.0

21. **Procurement Quality Assurance**

A. Origin

☐ PQA ☐ Acceptance of listed items has been made by me or under my supervision and they conform to contract, except as noted herein or on supporting documents.

Date _____ Signature of Auth. Govt Rep.

Typed Name and Office

B. Destination

☐ PQA ☒ Acceptance of listed items has been made by me or under my supervision and they conform to contract, except as noted herein or on supporting documents.

Date _____ Signature of Auth. Govt Rep.

Typed Name and Office

22. **Receiver's Use**

Quantities shown in column 17 were received in apparent good condition except as noted

Date Received _____ Signature of Auth Govt Rep

Typed Name and Office

* If quantity received by the Government is the same as quantity shipped, indicate by (✓) mark, if different, enter actual quantity received below quantity shipped and encircle

23. Contractor Use Only

Material Inspection and Receiving Report	1. Proc. Instrument Iden (Contract) N00014-90-C-0226	(Order) No	6. Invoice No. Date	7. Page	of
				8. Acceptance Point	

2. Shipment No. SSI 0002	3. Date Shipped 06 Nov 1992	4. B/L TCN		5. Discount Terms	

9. Prime Contractor	Code		10. Administered By	Code

11. Shipped From (if other than 9)	Code	FOB:	12. Payment Will Be Made By	Code
			DFAS Columbus Center DFAS CO/Gateway Division PO Box 9225 Columbus OH 43218-9225	

13. Shipped To	Code	14. Marked For	Code
Office of Naval Research Dept of The Navy 800 North Quincy St. Arlington, VA 22217-5000		Code Ref Contract N00014-90-C-0226	

15. Item No.	16. Stock/Part No. Description (Indicate number of shipping containers, type of container, container number)	17. Quantity Ship/Rec'd*	18. Unit	19. Unit Price	20. Amount
CLIN 0001	Research to integrate semiconductor electronics with infrared sensors based on superconducting transition edge bolometers to make a 16 pixel 4x4 two-dimensional infrared staring array		L		
CLIN 0003 A003	Final Report		LT	NC	

21.	Procurement Quality Assurance		22.	Receiver's Use
	A. Origin	B. Destination		Quantities shown in column 17 were received in apparent good condition except as noted
	☐ PQA ☐ Acceptance of listed items has been made by me or under my supervision and they conform to contract, except as noted herein or on supporting documents.	☐ PQA ☒ Acceptance of listed items has been made by me or under my supervision and they conform to contract, except as noted herein or on supporting documents.		

Date Received _____ Signature of Auth. Govt Rep

Typed Name and Office

Date	Signature of Auth. Govt Rep.	Date	Signature of Auth. Govt Rep.
Typed Name and Office		Typed Name and Office	

* If quantity received by the Government is the same as quantity shipped, indicate by (✓) mark, if different, enter actual quantity received below quantity shipped and encircle

23. Contractor Use Only

Final Report

Monolithic Integration of Semiconductor and Superconductor Components

Contract No. N00014-90-C-0226
ARPA Order No. 7534

4 September 1990 - 30 September 1992

Paul W. Kruse
Burgess R. Johnson

Honeywell Sensor and System Development Center
10701 Lyndale Avenue South
Bloomington, MN 55420

31 October 1992

Program Manager: Paul W. Kruse   Phone #: 612/887-4441

Principal Investigator: Burgess Johnson   Phone #: 612/887-4505

Section Head: David W. Nielsen   Phone #: 612/887-4576

Department: Norman A. Foss   Phone #: 612/887-6424

ii

Table of Contents

List of Figures

List of Figures - Continued

List of Figures - Continued

List of Figures - Continued

List of Tables

Executive Summary

Honeywell Sensor and System Development Center (SSDC) was awarded DARPA contract N00014-90-C-0226, "Monolithic Integration of Semiconductor and Superconductor Components" on 4 September 1990. Office of Naval Research is the contracting agency. The technical work was to be completed 30 June 1992. Honeywell requested and received approval for a three month no-cost extension. The technical work was completed 30 September 1992. The original award was for $562,022. An additional award of $89,310 was received, increasing the total value to $651,332.

The objective of the contract was to conduct research to integrate semiconductor electronics with infrared sensors based upon high transition temperature superconducting microbolometers to make a 16 pixel (4x4) two-dimensional infrared staring array. This technology should enable us to eventually fabricate large area, high performance IR arrays using conventional silicon IC processing technology for cost-effective systems. Deliverables included quarterly reports, this final report, and a 16 pixel (4x4) two-dimensional superconducting microbolometer array including transistor switches at the pixels and drive electronics mounted in a Dewar. All items were delivered.

Under a previous DARPA/ONR contract[*] and Honeywell internal funding, Honeywell had investigated the deposition by ion beam sputtering of thin films of the high temperature superconductor $YBa_2Cu_3O_{7-x}$ (YBCO) on buffer layer thin films of yttria stabilized zirconia (YSZ) on thin films of Si_3N_4 on three-inch (7.62 cm) diameter silicon substrates. Using conventional silicon processing technology plus a final KOH anisotropic etch, individual pixels and linear arrays of transition edge superconducting microbolometers had been prepared and evaluated with excellent results. In the present contract, bipolar transistors were fabricated in the silicon substrates prior to microbolometer fabrication, arranged so that each pixel consisted of a YBCO superconducting microbolometer connected in series with a bipolar transistor.

The bipolar transistor substrates were prepared at Honeywell's MICRO SWITCH silicon process fabrication facility in Richardson, TX. The transistor substrates were fabricated at Honeywell expense and donated to the contract at no cost to the contract. Under the contract, Honeywell SSDC hired Mary Weybright, a Stanford University graduate student expert in the design of cryogenic bipolar transistors, to work with MICRO SWITCH to modify their bipolar process in order to optimize the transistor performance for operation in the 70 K - 90 K temperature interval. A process run was carried out at MICRO SWITCH which included six variations ("splits") of the transistor design. These were evaluated at Honeywell SSDC before and

---

[*] DARPA/ONR contract N00014-88-C-0394, "High Temperature Superconducting Film Development for Advanced IR Sensors," 15 April 1988 through 14 July 1991, $1,472,505.

after completion of the processing of the superconducting microbolometers on the substrates. The best design had a leakage current of ~100 picoamps and a current gain (h_{fe}) of 31 at 77 K, after completion of microbolometer processing. These values are sufficiently good to allow the successful operation of very large (100,000 pixel) two-dimensional superconducting microbolometer focal plane arrays.

Under this contract, Honeywell SSDC carried out two processing runs to fabricate superconducting microbolometers. These runs enabled us to identify the critical processing compatibility steps and to identify the potential solutions to fabricating fully functional monolithic arrays. The process for fabricating superconducting microbolometer arrays contains many steps, the final one being a KOH anisotropic etch. The YBCO must be passivated against the KOH etchant. In the first run, the objective was to fabricate microbolometers without transistors in the substrate, to demonstrate that the YBCO could be successfully passivated against the KOH etchant and that microbolometers could be successfully fabricated. The YBCO was attacked by the KOH on the microbolometers and on the wire bond pads. These problems were solved in a subsequent Honeywell - funded process run. After the successful fabrication of microbolometers, a process run was carried out under the contract to fabricate 4x4 microbolometer arrays with transistors in the substrate at each pixel. Two of the wafers in this process run had YBCO deposited by laser ablation at the Jet Propulsion Laboratory (JPL) in order to explore the effects of microbolometer processing on YBCO films with superconducting properties superior to those of films grown at Honeywell. After completion of the microbolometer processing, good performance of the transistors was demonstrated at low temperature (77 K). However, the superconductor was degraded in this process run, and the KOH attacked the YBCO at the Au/YBCO contacts. Neither of these problems are major obstacles. Each has an identified potential solution. However, contract funds were inadequate to carry out a third process run incorporating the proposed changes.

Honeywell verified the cryogenic operation of the combination of the superconducting microbolometer and the bipolar transistors by wire bonding a superconducting microbolometer from a partially successful array with transistors from another array. The combination operated successfully as an infrared sensor that could be switched on and off with the transistor at the proper operating temperature.

Honeywell subcontracted to the Department of Physics and Astronomy of the University of Minnesota a study directed by Prof. Allen Goldman of electrical noise at the superconducting transition edge of YBCO. Because the noise appears at the low temperature foot of the superconducting resistive transition, whereas the bolometers operate at the midpoint of the transition, this excess noise is not expected to be a major problem in superconducting microbolometer focal plane arrays.

2

As a result of work performed under this contract, three papers were published in conference proceedings, four invited talks were given at scientific meetings, and nine contributed talks were given at scientific meetings.

1.0 Introduction

Honeywell Sensor and System Development Center was awarded DARPA/ONR contract N00014-90-C-0226, "Monolithic Integration of Semiconductor and Superconductor Components" on 4 September 1990. The contract award was for $562,022. An additional award of $89,310 was later received, increasing the total to $651,332. The technical work under the contract was to be completed 30 June 1992. Honeywell requested and received approval for a three month no-cost extension. Thus the technical work was completed on 30 September 1992; this report will be delivered on 31 October 1992.

The objective of the contract was to conduct research to integrate semiconductor electronics with infrared sensors based upon high transition temperature superconducting microbolometers to make a 16 pixel (4x4) two-dimensional infrared staring array. Deliverables included quarterly reports, a final report, and a 16 pixel (4x4) two-dimensional superconducting microbolometer array including transistor switches at the pixels and drive electronics mounted in a Dewar.

In order to understand Honeywell's approach to developing a 4x4 superconducting microbolometer focal plane array, some background is necessary. Under Army Night Vision and Electro Optics Directorate (NVEOD) and Defense Advanced Research Planning Agency (DARPA) funding, between 1985 and 1991, Honeywell developed uncooled microbolometer infrared focal plane arrays based upon Si microstructure technology. The initial two-year program, known as ASP, resulted in the development of 64x64 pixel uncooled metal film bolometer arrays. ASP was followed by HIDAD (High Density Array Development), a 4.5 year program which resulted in the development of 240x336 pixel uncooled semiconductor film bolometer arrays. The responsivity of a microbolometer depends directly upon the temperature coefficient of resistance of the detecting material. It had been shown that the temperature coefficient of resistance of the high T_c superconductor $YBa_2Cu_3O_{7-x}$ (YBCO) at the transition edge of about 90 K was 100 times higher than that of semiconductors. Therefore, it should be possible to improve the noise equivalent temperature difference of a YBCO superconducting transition edge microbolometer focal plane array by as much as 100 times over that of an uncooled semiconductor array. Furthermore, much of the silicon microstructure technology developed by Honeywell under the ASP and HIDAD contracts would be applicable to that of a superconducting microbolometer array.

Thus Honeywell proposed and received from DARPA through Office of Naval Research (ONR) contract N00014-88-C-0394, "High Temperature Superconducting Film Development for Advanced IR Sensors." Under this contract ("DARPA-1") Honeywell successfully prepared single pixel and linear arrays of thin film superconducting microbolometers based upon the superconducting transition edge of YBCO.

Honeywell's approach to HIDAD was to use Si microstructure technology in which the resistive thermally sensitive material resided upon a Si_3N_4 membrane suspended over the silicon substrate. This provided the greatest thermal isolation of any known approach, yet was compatible with standard Si processing technology. Furthermore, HIDAD arrays were prepared on 4 inch diameter Si wafers to facilitate high volume production if such should be required. Thus, Honeywell's approach to superconducting microbolometer development under contract N00014-88-C-0394 required that all development be compatible with silicon microstructure technology.

What this meant in practice was that from the very beginning of contract N00014-88-C-0394 it was decided that the superconducting YBCO films must be deposited upon Si_3N_4 membranes formed on silicon wafers. At each pixel the Si underlying the membrane would be etched away. The state of the art of YBCO film development was such that excellent films could be prepared on small (say, 1 cm), lattice matched, single crystal substrates such as $SrTiO_3$. Honeywell had to develop a process for preparing films on non-lattice matched polycrystalline film substrates. Because the YBCO films were not superconducting when deposited directly on the Si_3N_4 films, an intermediate layer of yttria stabilized zirconia (YSZ) was deposited upon the Si_3N_4, the YBCO being deposited upon that. Furthermore, these films on their silicon substrates had to be stress balanced over the temperature range from the growth temperature to the operating temperature, i.e., from about 730°C to about 80 K. If the films were not stress balanced, they would curl up like a potato chip when the silicon underneath them was etched away.

By the end of Contract N00014-88-C-0394, Honeywell had shown that $YBa_2Cu_3O_{7-x}$ superconducting thin films could be prepared by ion beam sputtering on thin films of YSZ over thin films of Si_3N_4 on Si substrates. The superconducting transition edge was not as sharp as that obtained when the YBCO films are deposited on lattice matched substrates but it was sufficiently steep. The next step, carried out under contract N00014-90-C-0226 ("DARPA-2"), was to integrate transistor switches with the microbolometers such that each pixel comprised a series combination of YBCO microbolometer and transistor. Thus a 4x4 array, chosen for demonstration purposes, would require a 4x4 array of transistors. The technical challenge was to integrate the microbolometers with the transistors. Bipolar transistors were chosen for the investigation.

The integration problem was as follows. The transistors must be implanted in the Si substrates before the YBCO is deposited, which meant that the transistors must withstand a temperature of 730°C. Furthermore, the transistors must operate successfully at the transition edge of the YBCO film, roughly 80 K. Successful operation meant that the transistor leakage current must be of the order of nanoamps or lower so that in large arrays hundreds of them could be coupled to the same column line, and their

5

current gain (h_{fe}) must be of the order of 20 or higher so that their on-resistance in series with the microbolometer was negligible.

Honeywell SSDC had the bipolar transistor arrays fabricated at Honeywell's MICRO SWITCH silicon integrated circuit facility in Richardson, Texas. Mary Weybright, a graduate student at Stanford University who is pursuing a Ph.D thesis in cryogenic transistor technology, was hired as a consultant. She worked directly with MICRO SWITCH to modify their standard bipolar process to meet the above requirements. Her report is included in Section 4 of this report.

As under contract N00014-88-C-0394, Honeywell subcontracted studies of electrical noise at the transition edge of YBCO thin films to the University of Minnesota for work which was carried out under the direction of Prof. Allen M. Goldman in the Department of Physics and Astronomy. This was done in order to lay the foundation for optimizing the fabrication process so as to maximize the signal-to-noise ratio of the microbolometer. A report prepared by Prof. Goldman and his colleagues can be found in Section 5 of this report.

2.0 Growth of Superconducting Films

2.1 Introduction

All of the YBa$_2$Cu$_3$O$_7$ (YBCO) films grown at Honeywell under this contract were grown by ion beam sputtering on 3-inch silicon wafers. In order to fabricate large imaging arrays of microbolometers efficiently by standard silicon processing techniques, it is important to deposit the YBCO films on large area substrates. This is one of the primary reasons that ion beam sputtering was chosen to deposit the YBCO films.

A double buffer layer of Si$_3$N$_4$ and yttria - stabilized zirconia (YSZ) was used for the YBCO films on silicon wafers. The choice of buffer layer was dictated by the microbolometer requirements. Despite the amorphous nature of the the Si$_3$N$_4$, YBCO films have been grown which have a high enough temperature coefficient of resistance and low enough level of electrical noise to provide high sensitivity in a large imaging array of microbolometers.

The noise studies carried out under subcontract at the University of Minnesota were mostly performed on films of DyBa$_2$Cu$_3$O$_7$ grown by ozone - assisted MBE at the University of Minnesota. Two wafers in the second process run under this contract had YBCO films grown by laser ablation at the Jet Propulsion Laboratory (JPL). The growth techniques for the films grown at the University of Minnesota and at JPL will not be discussed in this report.

2.2 Ion Beam Sputtering Deposition System

The ion beam sputtering deposition system is shown schematically in Figure 2.1. Except for a few modifications, this was the same chamber described in the final report for contract #N00014-88-C-0394, "High Temperature Superconductor Film Development for Advanced IR Sensors", submitted to DARPA/ONR on September 14, 1991.

The water - cooled cylindrical chamber was 63.5 cm in diameter and 56 cm long, and was equipped with an Ion Tech Model 1500 ion gun capable of 350 mA beam current at 15 kV. The beam diameter was approximately 15 cm. For most of the YBCO films grown under this contract, the ion beam current was 25 mA and the beam voltage was 1000 Volts. Xenon was used as the sputter gas because its heavy mass prevents resputtering of the deposited film. Oxygen and ozone were admitted to the chamber to oxidize the YBCO film. The ozone was injected through quartz nozzles near the growing film. The chamber was pumped by a cryopump having 1500 liters/sec pumping speed for air (CTI Cryo Torr - 8). The base pressure was typically 5 x 10^{-7} Torr.
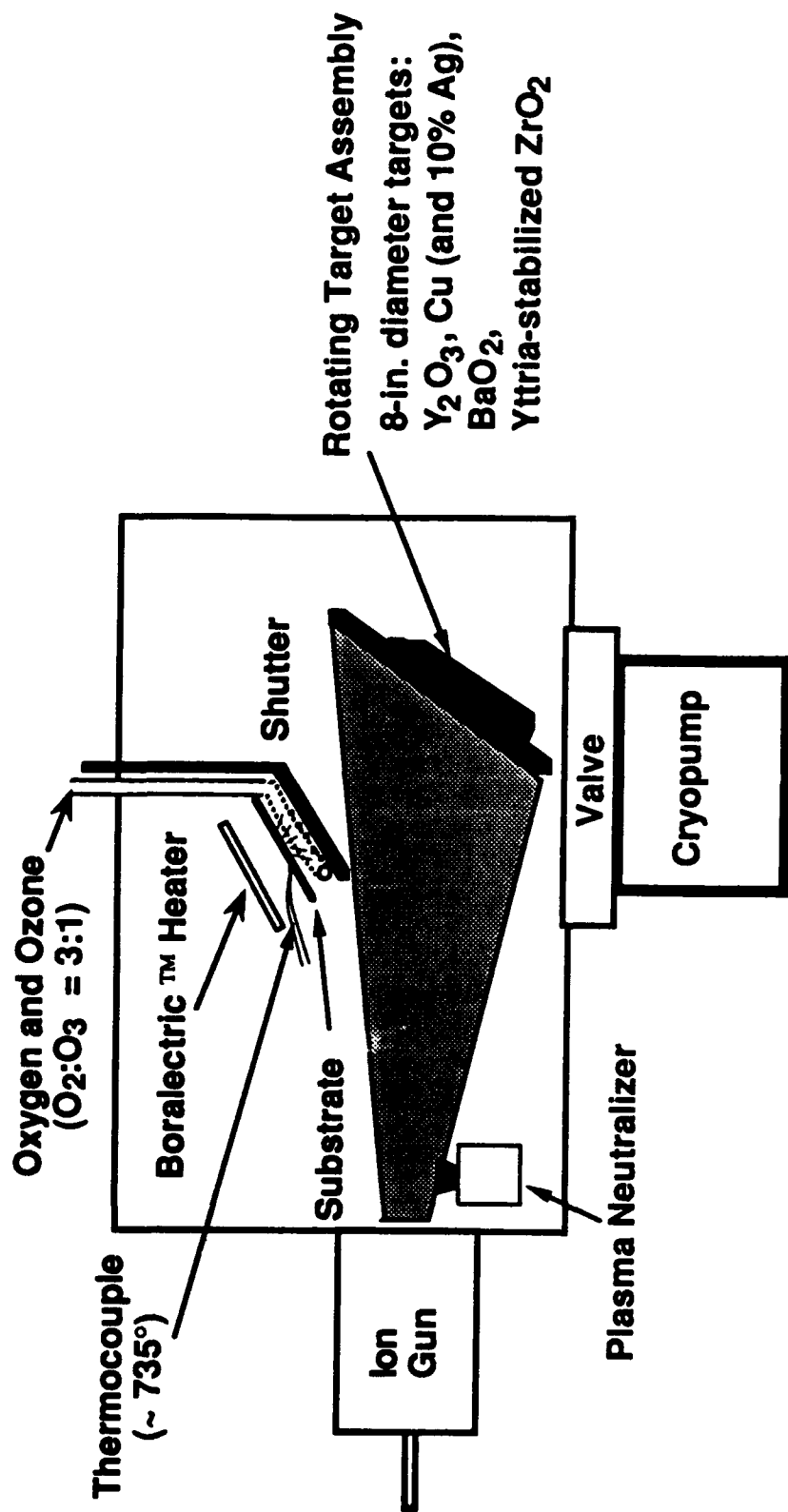
Figure 2.1: Schematic diagram of the ion beam sputter chamber used to grow films of YBCO, as well as YSZ and gold.

8

The ion beam impinged on a rotating target assembly containing four targets (each 20 cm in diameter and 0.63 cm thick): Y_2O_3, BaO_2, Cu, and YSZ. For some of the films, a piece of silver foil held by a silver rod was placed on the copper target, in an attempt to dope the YBCO films with silver and reduce the electrical noise in the films. When gold was deposited on top of the freshly grown YBCO film, for low resistance electrical contacts to the YBCO, a gold target replaced the YSZ target. The targets were mounted on a copper platter 50.8 cm in diameter. The copper platter was rotated by a stepper motor which was controlled by a computer to precisely control the dwell time of the ion beam on each target. In this way, the stoichiometry of the YBCO films was controlled. The stoichiometry was measured by Direct Coupled Plasma - Atomic Emission Spectroscopy (DCP-AES), or Inductively Coupled Plasma - Mass Spectroscopy (ICP-MS) at the University of Minnesota Geochemistry Laboratory.

Because the sputter rate of copper is much faster than that of Y_2O_3 and BaO_2, it was necessary to minimize the time the ion beam spent on the copper target. This was accomplished by stopping the platter only while the ion beam was sputtering Y_2O_3 and BaO_2. The copper target was sputtered only during the time that the platter was being rotated to change the positions of the Y_2O_3 and BaO_2 targets.

The dwell times of the ion beam on each target were adjusted as needed to obtain the desired film stoichiometry. Adjustments were also necessary when the oxygen and ozone gas pressures were changed. As the oxygen and/or ozone pressure was increased, it was found that longer dwell times on the Y_2O_3 and BaO_2 targets were necessary. This is consistent with a slower copper sputter rate in a more oxidizing environment, due to formation of copper oxide on the surface of the copper target.

The following is an example of the typical timing for the target dwell times. For the films grown on wafers in the second microbolometer process run under this contract, typical sputtering times for each target during a single cycle through the targets were: Y_2O_3, 3.48 sec; BaO_2, 4.71 sec; and copper, 1.94 sec. These times include the time that the target assembly was in motion and the beam was sweeping over a target or over the surface of the copper platter. For this typical example, the total time required to cycle through all three targets was only 10.13 sec. The average deposition rate of YBCO was only 0.3 Å/sec. Thus, one monolayer of c-axis oriented YBCO with a c-axis lattice spacing of 11.7 Å was deposited in 39 sec. During this time, the ion beam cycled through all the targets about four times. Thus, although the deposition of the elements Y, Ba, Cu was sequential, there was good mixing of the elements during the time required to deposit a monolayer of c-axis oriented YBCO.

The 3-inch silicon wafers onto which the YBCO films were deposited were heated radiatively by a Boralectric[TM] heater (Union Carbide) which consisted of a pyrolitic graphite heater element encased in boron nitride. The temperature of the wafer was measured with a thermocouple pressed against the backside of the wafer. The wafer could be rotated approximately 180° while the film was deposited, to provide a more uniform film.

2.3 Choice of Buffer Layers

The choice of buffer layer was dictated by the microbolometer requirements. Silicon nitride is the material of choice for fabricating microbolometers by silicon micromachining because of its mechanical strength, low thermal conductivity, and resistance to many etchants. Hence, the YBCO films grown under this contract were grown on double buffer layers of Si_3N_4 and YSZ. The Si_3N_4 film, typically 3000 Å thick, was deposited onto the 3 - inch silicon wafer by sputtering, then the YSZ film, typically 600 Å thick, was deposited in-situ by ion beam sputtering immediately before the YBCO deposition.

The disadvantage of this choice of buffer layers is that the sputtered Si_3N_4 films used for silicon micromachining, and for the work under this contract, are amorphous. Hence, YBCO films grown on Si_3N_4/YSZ buffer layers have no preferred in-plane orientation of the crystalline axes. This results in YBCO films with superconducting properties inferior to that of films grown on single crystal substrates such as $SrTiO_3$ or $LaAlO_3$. Nevertheless, a Honeywell - funded microbolometer process run showed that microbolometers fabricated from YBCO films on Si_3N_4/YSZ buffer layers have responsivity and noise performance adequate for fabrication of very sensitive large imaging arrays of microbolometers. The superconducting properties of the films grown under this contract are presented below.

2.4 Film Growth Conditions and Results

The resistance as a function of temperature is shown in Figures 2.2 and 2.3 for three films which are representative of the range of growth parameters used for YBCO films grown under this contract. The temperature coefficient of resistance (TCR), defined as $(dR/dT)/R$, as a function of temperature for these three films in the superconducting transition region is shown in Figure 2.4. Some properties and growth conditions of these three films are summarized in Table 2.1. The film with the best superconducting properties (HTS-145), has an onset of the superconducting resistive transition at ~89 K, the midpoint is at ~82.5 K, and zero resistance is reached at ~74 K. The temperature coefficient of resistance at the midpoint is 0.32 K^{-1}. For a large imaging array of superconducting microbolometers, a TCR of about 0.3 K^{-1} is desired for good performance. A gold film was grown in-situ over this YBCO film, to form low resistance electrical contacts to the YBCO. The superconducting properties were measured after the gold film was removed by wet etching in gold etch solution consisting of KI and I_2 in water [1].

The x-ray spectrum of film HTS-145, shown in Figure 2.5, shows that the c-axis is oriented perpendicular to the substrate. This orientation was observed for almost all the YBCO films grown under this contract.

10
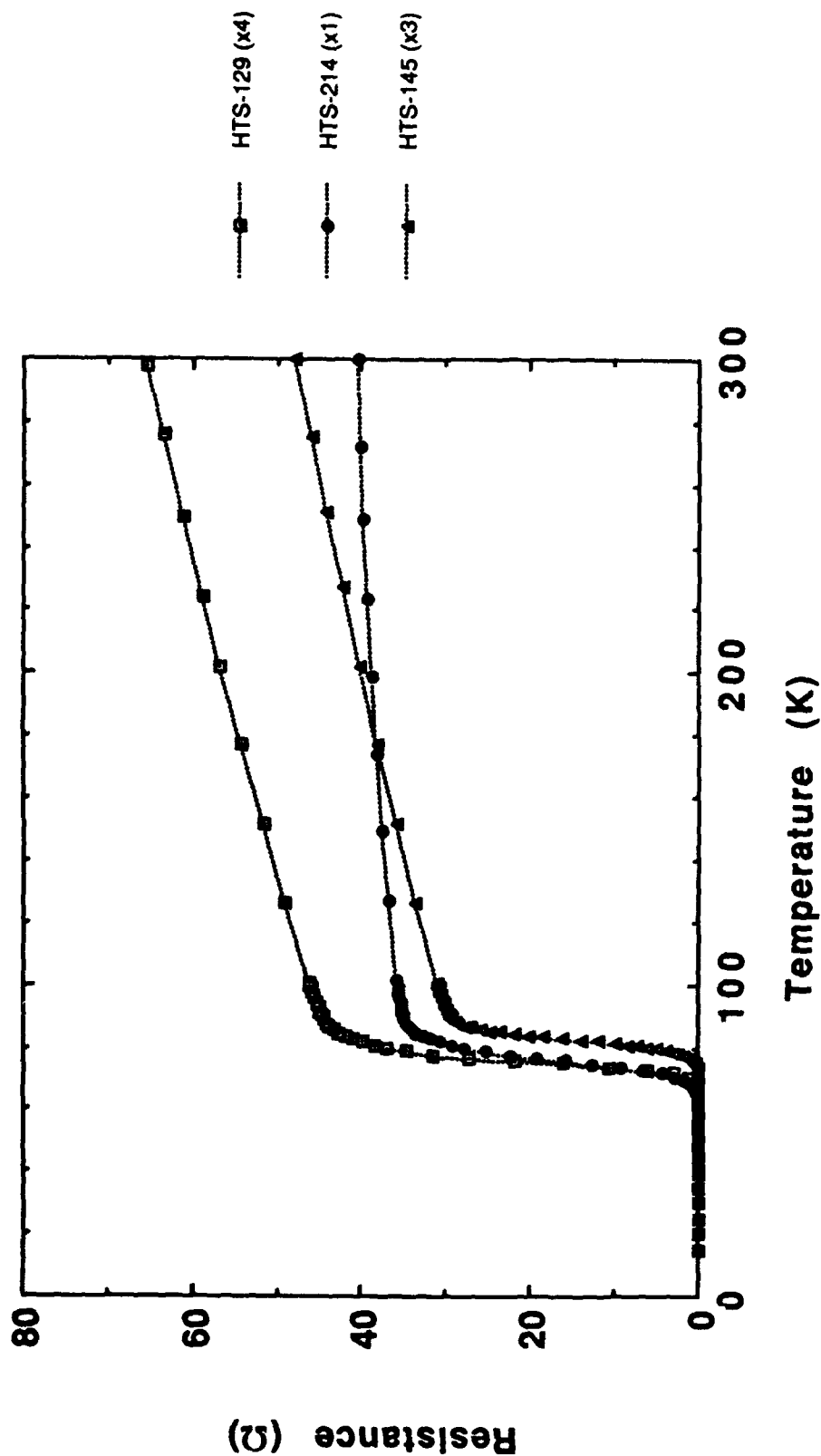
Figure 2.2: Resistance as a function of temperature from 300 K to below T_c for three YBCO films representing the range of growth parameters used in the films grown under the contract. The resistances of HTS-129 and HTS-145 have been multiplied by appropriate factors to provide easier comparison between the three films. The resistance plotted here is not to be confused with the sheet resistance.
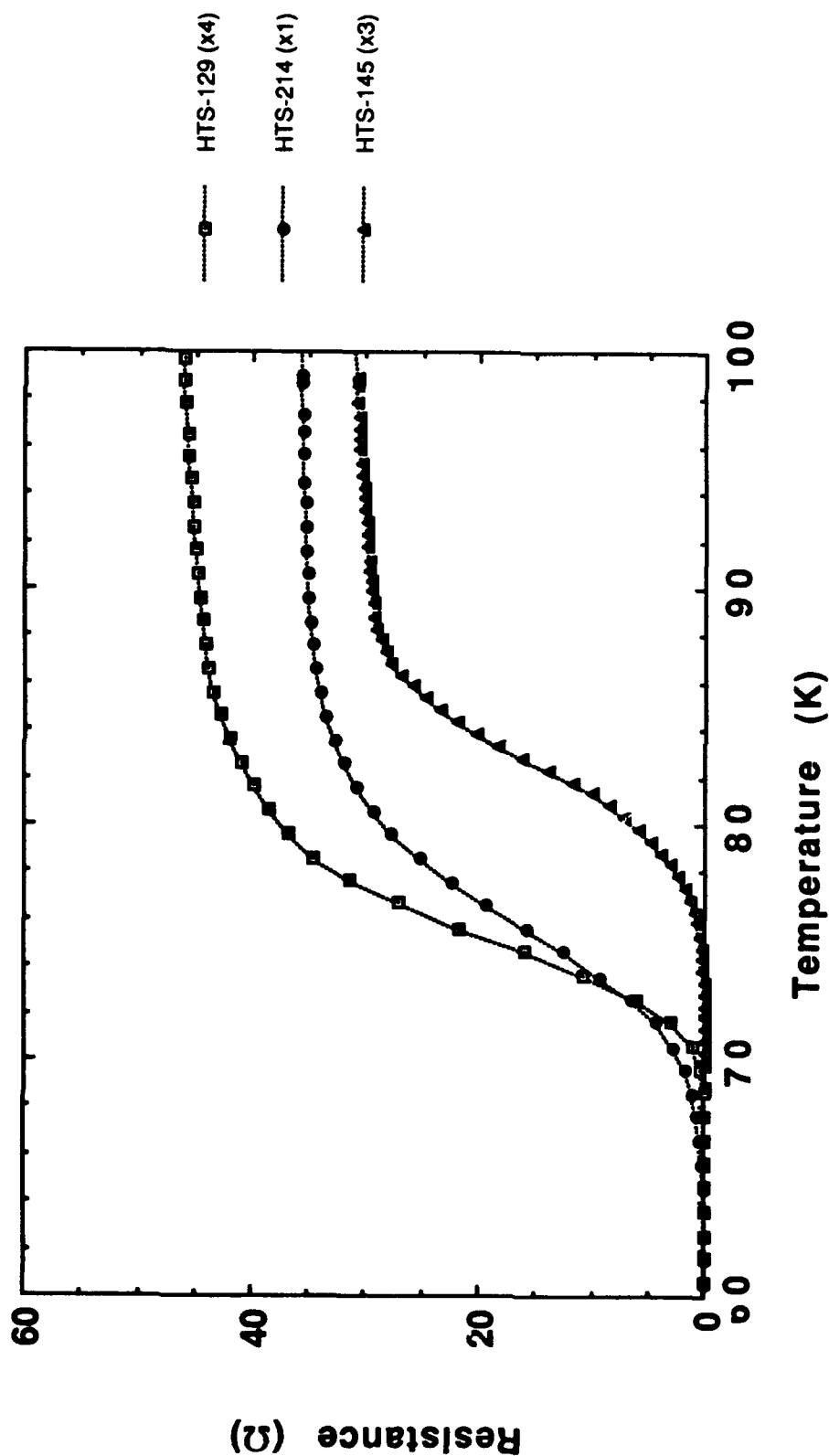
Figure 2.3: Resistance as a function of temperature in the superconducting transition region for three YBCO films representing the range of growth parameters used in the films grown under the contract. The resistances of HTS-129 and HTS-145 have been multiplied by appropriate factors to provide easier comparison between the three films. The resistance plotted here is not to be confused with the sheet resistance.
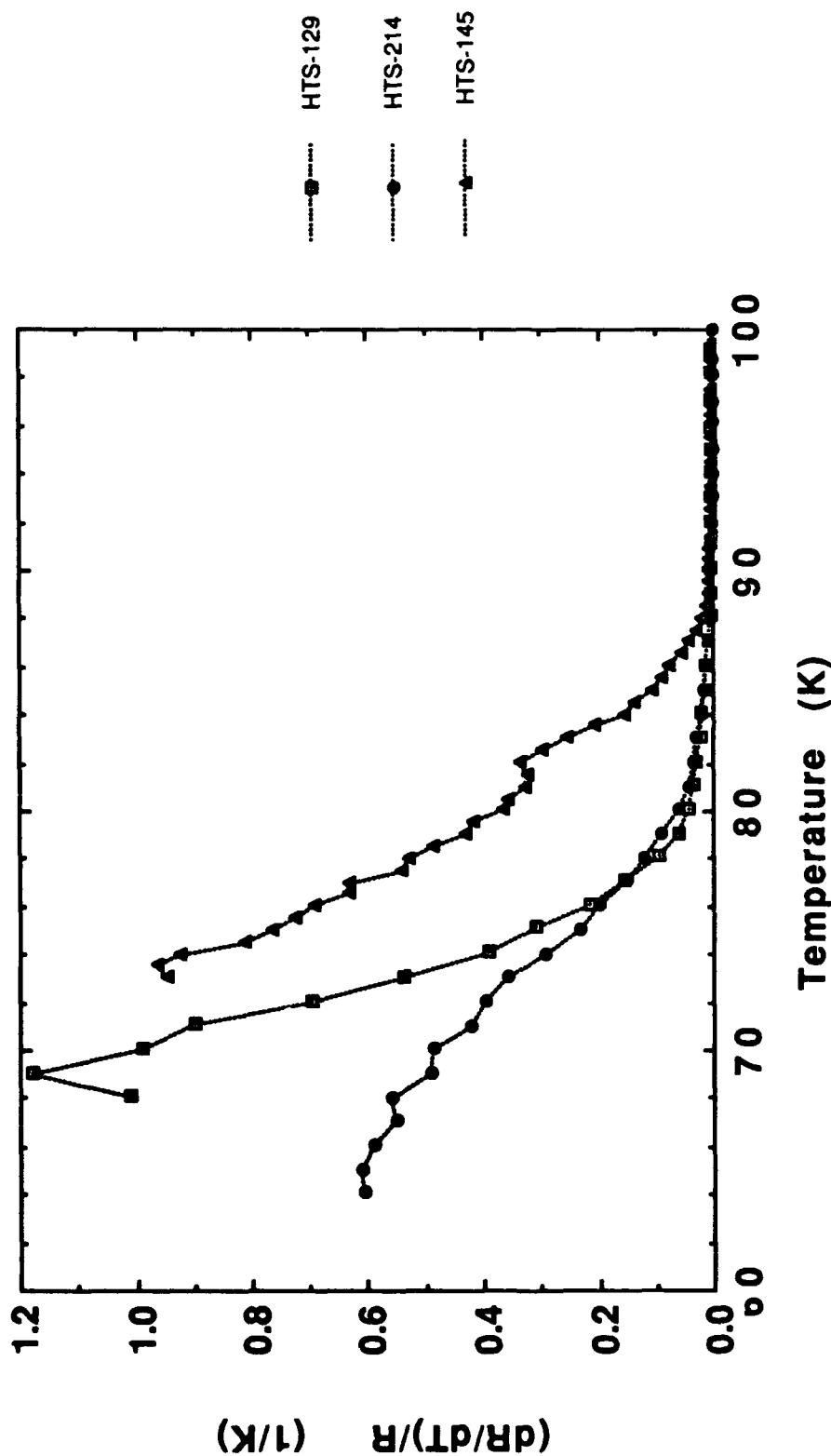
Figure 2.4: The temperature coefficient resistance (TCR) as a function of temperature in the superconducting transition region for three YBCO films representing the range of growth parameters used in the films grown under the contract. Data in the tail of the transition are not displayed because noise makes the data in that region meaningless.

13
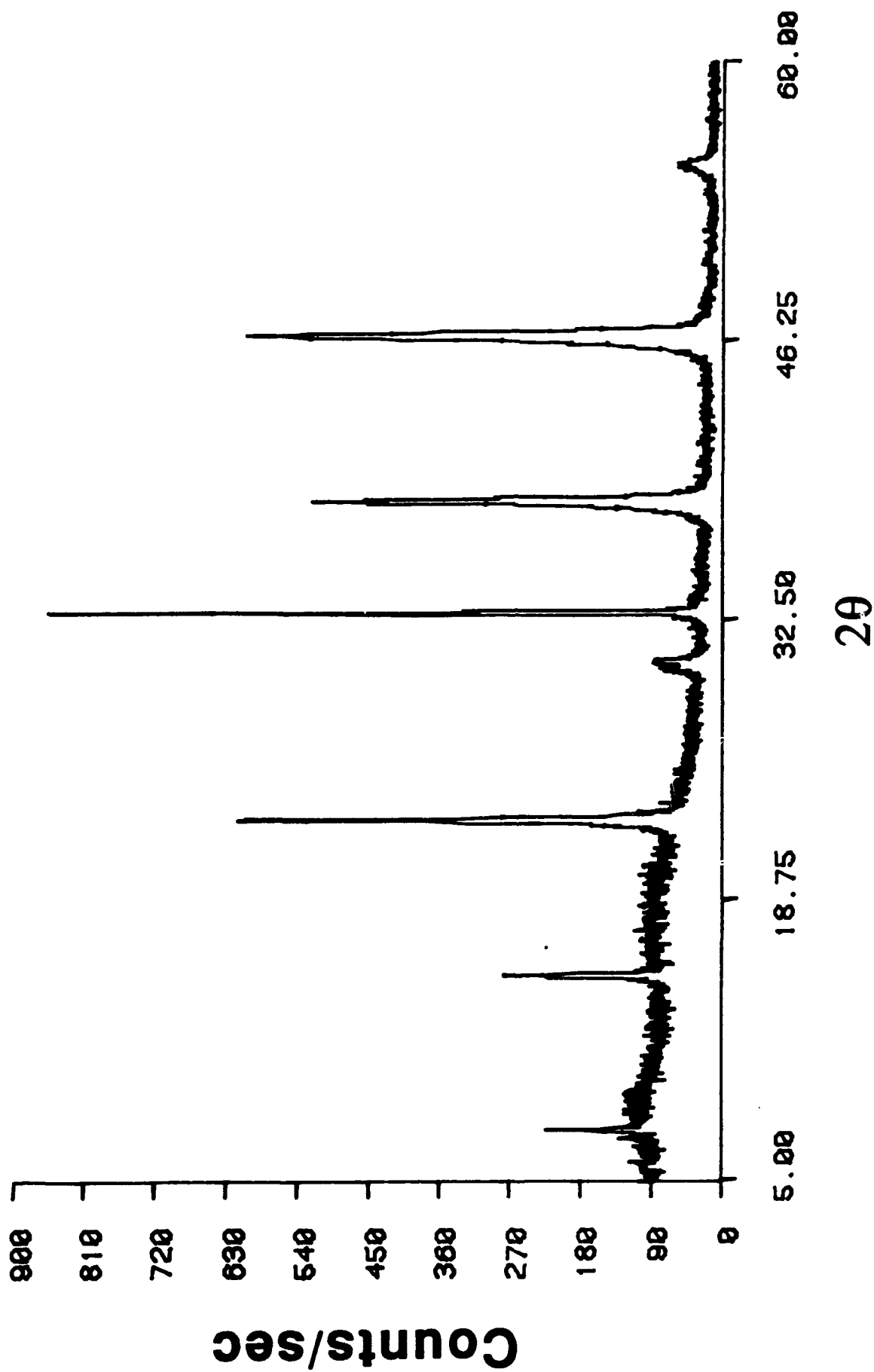
Figure 2.5: X-ray spectrum of HTS-145. The narrow peak at 33° is the silicon (200) peak from the substrate. The c-axis orientation of the YBCO film is clearly seen.

14

Table 2.1
Properties and growth conditions of three films representing the range of growth parameters used for films grown under the contract.

Property	HTS-129	HTS-145	HTS-214
Sheet resistance at room temperature (middle of wafer)	25 Ω	40 Ω (after removing gold)	33 Ω
Range of sheet resistance over the wafer	25 Ω to 58 Ω	unknown	33 Ω to 44 Ω
T_c onset (mid-wafer)	88 K	89 K	87 K
T_c midpoint (mid-wafer)	76.5 K	82 K	76 K
T_c (R=0) (mid-wafer)	67 K	74 K	59 K
Temperature coefficient of resistance (TCR) at T_c midpoint	$0.19\ K^{-1}$	$0.32\ K^{-1}$	$0.20\ K^{-1}$
Y:Ba:Cu (middle of wafer)	1.0:2.36:2.98	1.0:1.72:2.54	1.0:1.98:3.31
Ag/Cu molar ratio	0.0	0.046	0.0

Growth Conditions

	HTS-129	HTS-145	HTS-214
Growth temperature	730°C	720°C	700°C (with transistors)
O_2 partial pressure	0.35 mTorr	0.42 mTorr	1.31 mTorr
O_3 partial pressure	0.08 mTorr	0.10 mTorr	0.10 mTorr
H_2O partial pressure	0.0	0.0	0.01 mTorr

The growth conditions for film HTS-145 were as follows. Before growing the YBCO, a layer of sputtered Si3N4 3000 Å thick was deposited onto the 3 - inch silicon wafer. A YSZ buffer layer 600 Å thick was then deposited by ion beam sputtering under the following growth conditions:

Growth temperature: 720°C
Growth time: 60 minutes
Oxygen flow rate: 8 sccm
                         (corresponds to a chamber partial pressure of 3.5 x 10⁻⁴ Torr)
No ozone flow.

After the YSZ deposition, the chamber was opened, and the YSZ target was replaced with a gold target. The YBCO film (2000 Å thick) was then deposited by ion beam sputtering under the following conditions:

Growth temperature: 720°C
Growth time: 90 minutes
Oxygen flow rate: 9.5 sccm
                         (corresponds to a chamber partial pressure of 0.42 x 10⁻⁴ Torr)
Ozone manifold pressure: 1300 mTorr
                         (corresponds to a chamber partial pressure of 0.10 x 10⁻⁴ Torr)

Y2O3 target sputter time: 2.59 sec
BaO2 target sputter time: 2.95 sec
Cu sputter time: 1.25 sec
Silver: 8.35 square inches of silver foil on copper target.

After deposition, the film was cooled to 200°C in 1 hour with the ion beam on and oxygen and ozone flowing at the same rates used during YBCO film growth. A gold film ~1000 Å thick was then deposited onto the YBCO film by ion beam sputtering without breaking the vacuum, in order to make low resistance electrical contacts to the YBCO.

The molar ratios of the elments in film HTS-145 were Y:Ba:Cu = 1.0 : 1.72 : 2.54. The molar ratio of silver to copper was about 0.046. The gold film was contaminated with a small amount of copper, because the ion beam sputtered some of the copper platter surrounding the gold target. Because the ICP-MS analysis measured the amount of copper in the YBCO and in the gold, it was neceesary to correct for this to determine the copper composition of the YBCO.

The surface of film HTS-145 was somewhat rough, with particles somewhat less than one micron in size on the surface. These are believed to be associated with the rather high silver content of the film (Ag/Cu = 0.046), since this rough morphology was seen on other films with similar quantities of silver. In the case of extreme roughness, this is a serious problem for microbolometer fabrication, since the YBCO film must be passivated against the KOH etchant that is used to etch away the silicon from underneath the thermally isolated microbolometer. However, all the microbolometers that have been successfully fabricated at

Honeywell have had some degree of surface roughness. An example of surface roughness on part of a patterned YBCO meander line from the second process run on this contract is shown in Figure 2.6.

In the course of optimizing the YBCO film growth conditions, many variations of the growth conditions were used. The results of some of these variations will be discussed below.

Excess barium and modest oxygen pressure during film growth produced YBCO films with low sheet resistance at room temperature, but with superconducting transitions that were not quite as good as film HTS-145. An example of such a film is HTS-129, whose resistance and TCR as functions of temperature are given in Figures 2.2, 2.3, and 2.4. The sheet resistance of this film was only 25 Ω at room temperature (measured in the middle of the wafer). The molar stoichiometry of this Ba - rich film was Y:Ba:Cu = 1.0 : 2.36 : 2.98. As can be seen by comparing the resistance vs. temperature curves of HTS-145 and HTS-129 in Figure 2.3, the transition temperature of HTS-145 is significantly higher than HTS-129, despite the lower room temperature sheet resistance for HTS-129. Both films were about the same thickness (2000 Å).

Large increases in the oxygen pressure did not produce films with superior superconducting transitions. However, a higher oxygen pressure during growth generally increased the uniformity of the room temperature resistance over the 3 - inch wafer, perhaps due to increased scattering of ions and the resultant increased spreading of the ion beam. Film HTS-214 was grown in an oxygen pressure 3 to 4 times higher than HTS-145 or HTS-129. As shown by the data on the range of room temperature resistances over the surface of the wafer in Table 2.1, film HTS-214 is significantly more uniform than the other two films mentioned above. However, HTS-214 has a superconducting transition which is inferior to that of HTS-145 and HTS-129, as illustrated in Figures 2.2, 2.3, and 2.4.

A small amount of water vapor was used during growth of HTS-214, because results from an earlier film (HTS-210) had indicated improved superconducting properties when water vapor was used during growth. This film had T_c onset = 91.5 K, and T_c midpoint = 83 K, but the TCR at the midpoint was only 0.16 K^{-1}. It should be noted that HTS-210 was grown on a silicon test wafer, whereas HTS-214 was grown on a wafer with monolithic transistors. The thermocouple on the back of the wafer during YBCO growth indicated 740°C for HTS-210, but only 700°C for HTS-214. In both cases, the growth temperature was believed to be close to optimum. Apparently, the transistors, PtSi contacts, etc. changed the heat transport to the front side of the wafer where the YBCO was being deposited.

The reason for the lack of consistently improved superconducting properties with higher oxygen pressures is not clear. The ICP-MS analysis of some of our films grown with 30 sccm oxygen fow rate showed small quantities (~1%) of tungsten, which could originate from oxidation of the filament in the ion gun. However, Auger depth profiling showed no evidence of tungsten.
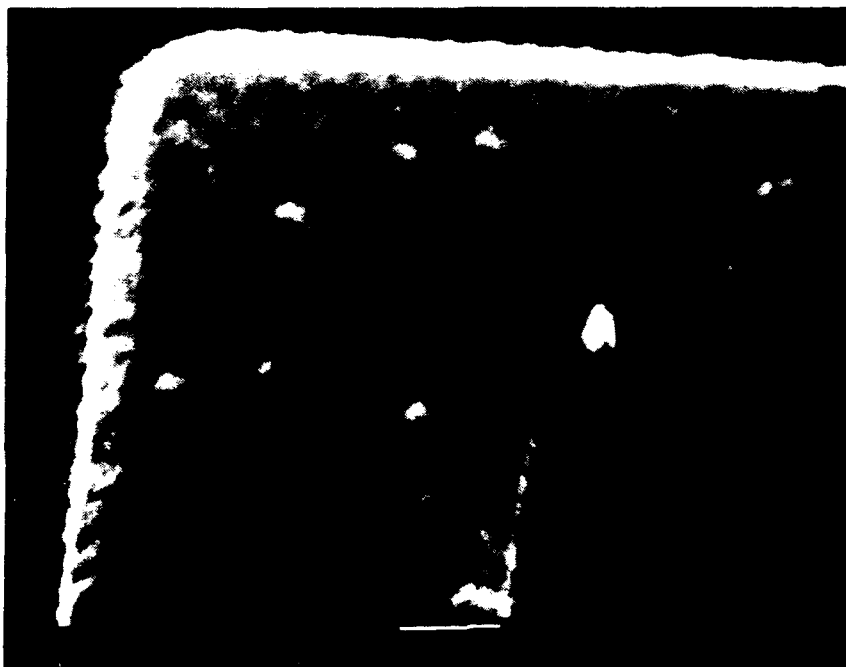
Figure 2.6: A patterned meander line of YBCO passivated by Si_3N_4. Note the roughness of the YBCO film.

The YBCO films for the second process run under this contract were grown under conditions similar to those used to grow film HTS-214. There were two reasons for this. First, the superconducting transition of HTS-145 was only rarely reproduced. The cause of this irreproducibility is not known. Films with superconducting transitions similar to HTS-129 were also difficult to reproduce at the time that the second microbolometer process run was beginning. Second, films such as HTS-214 which were grown in high oxygen pressure had the attractive feature of uniformity, as indicated by the room temperature resistance. Uniformity of the sensing elements is an important aspect of high performance imaging arrays.

2.5 Summary

The primary problem with growing films for use in microbolometers is that the most desirable technology for fabrication of microbolometers involves the use of amorphous layers of Si_3N_4. The YBCO superconductor must be deposited after the Si_3N_4 deposition, in order to protect the bottom side of the YBCO from being etched when the silicon is removed from underneath the microbolometer by the chemical etchant. Because of the amorphous nature of the Si_3N_4, the YBCO cannot be deposited epitaxially, and inferior superconducting properties result. However, much of the performance of a microbolometer relies on the thermal isolation of the microstructure, not on the sensitivity of the thermally sensitive material on the microstructure. As the temperature coefficient of resistance is increased, eventually a point is reached where temperature fluctuation noise arising from heat flow in the microstructure from the YBCO film to the silicon substrate becomes the dominant noise source. If the temperature coefficient of resistance is increased further, the signal and the noise increase at the same rate, and the signal to noise ratio does not increase. For Honeywell's thermally isolated microstructures and anticipated large imaging array operating parameters, this crossover point in the temperature coefficient of resistance is at about 0.3 K^{-1}. Films with superconducting transitions this sharp have been grown on double buffer layers of yttria - stabilized zirconia and amorphous Si_3N_4. Some of these results have been reported above. However, these results have not been obtained consistently. More work needs to be done to understand the ion beam sputtering film growth process on the YSZ/Si_3N_4 double buffer layers in order to grow YBCO films with consistently high temperature coefficients of resistance.

References

1. W. Eidelloth and R.L. Sandstrom, Applied Physics Letters 59, 1632 (1991).

3.0 Microbolometer Fabrication

3.1 Introduction

Two process runs were carried out to fabricate microbolometers under this contract. At the start of the contract, a reproducible process for fabricating high - T_c superconductor microbolometers had not yet been demonstrated. So, the objective of the first process run was to fabricate microbolometers with a process that would be reproducible. Transistors were not fabricated in this run. The microbolometers and the pads in this first process run were attacked by the KOH etchant, so no working devices were fabricated. These problems were resolved in a subsequent Honeywell - funded process run which was successful in producing working superconductor microbolometers.

The second process run funded by the contract combined the transistors fabricated at Honeywell expense by Honeywell's MICRO SWITCH Division with the successful microbolometer fabrication process demonstrated in the Honeywell - funded process run. Modifications to the microbolometer fabrication process were made to produce low - resistance contacts to the $YBa_2Cu_3O_7$ (YBCO) superconductor. Two of the wafers in this process run had YBCO film deposited at the Jet Propulsion Laboratory (JPL) by laser ablation. The YBCO on these two wafers had superconducting properties superior to those of the YBCO grown at Honeywell. This second process run demonstrated that the transistors can survive the microbolometer processing and still show good performance at low temperature (~77 K). The microbolometers were mechanically intact. However, the superconductor in this second processing run was degraded during processing, and it did not exhibit a superconducting transition.

3.2 First Process Run

The objective of the first microbolometer process run was to fabricate microbolometers with a process that would be reproducible. Transistors were not fabricated in this run. In previous work at Honeywell under DARPA/ONR contract #N00014-88-C-0394, "High Temperature Superconductor Film Development for Advanced IR Sensors", high - T_c superconductor microbolometers had been fabricated. The fabrication process that was used in that work involved first etching the microstructure for the bolometer and subsequently depositing the superconductor. The virtue of that process is that the superconductor does not need to be passivated against the KOH etchant used to remove the silicon from underneath the microstructure. However, the extremely good thermal isolation of the microstructure can produce a very large temperature difference between the microstructure and the substrate during deposition of the superconductor. Furthermore, as the emissivity of the superconductor film changes during deposition, a change in the temperature of the microstructure is produced. Since the quality of the superconductor film is very sensitive to the temperature during deposition, it is very difficult to deposit superconductor films reproducibly on previously etched microstructures.

20

In the first process run under this contract, the objective was to fabricate microbolometers by first depositing the superconductor, then passivating the superconductor with films of SiO_2 and Si_3N_4, and finally removing the silicon from underneath the microbolometer by etching in aqueous KOH solution. The mask set (#5228) used for this process run was the same one used in the work performed under contract #N00014-88-C-0394. This mask has 1x12 element linear arrays with a variety of different microbolometer shapes, a 2x32 array, and a 1x64 array. The step - by - step process sequence for the first process run is given in Table 3.1.

Two processing problems prevented successful devices from being produced in the first process run. The first problem involved etching of the SiO_2 passivation layer in the KOH solution. The SiO_2 layer was sandwiched between the top layer of Si_3N_4 and the YBCO, or (in areas where there was no YBCO) between the top layer of Si_3N_4 and the layer of Si_3N_4 forming the bottom of the the thermally isolated membrane. Thus, the SiO_2 was mostly protected from the KOH etchant. However, the SiO_2 layer was exposed at the edge of the via cut that allowed the KOH etchant to have access to the silicon. This allowed the KOH etchant to etch away the SiO_2 and delaminate the top half of the microbolometer from the bottom half (see Figure 3.1). In the Honeywell - funded process run and the second process run under this contract, no SiO_2 layer was deposited, and this problem was not encountered.

The second problem was etching of the pads by the KOH solution. An oxygen plasma was used to reoxidize the superconductor after the SiO_2 deposition. This caused an oxide, believed to contain silver, to be formed at the edges of the ohmic metal stack (Ag/TiW/Cr) in the pad areas. This oxide grew as sponge-like structures at the edge of the pad areas. The rough morphology of these structures made it impossible for the subsequent Si_3N_4 layer to passivate them. Thus, the KOH etchant etched away the superconductor underneath the pads. This problem was corrected in the subsequent two process runs by using gold rather than silver as the ohmic metal to make contacts to the YBCO. Gold does not form an oxide in the oxygen plasma used to reoxidize the YBCO.

3.3   Mask Set for 4x4 Arrays

A mask set (#5288) was designed and purchased for fabrication of the 4x4 arrays of microbolometers with monolithic transistors at each pixel. It was designed for use with 3-inch wafers. This mask set was used for fabrication of the transistors and the microbolometers.

The primary cell is 5.18 mm x 5.18 mm. It is shown in Figures 3.2 and 3.3. It contains ten 4x4 arrays. These arrays have four different transistor layouts (labeled A,B,C,D) and five different types of microbolometers (labeled 1,2,3,4,5). The microbolometers have a variety of support leg lengths and widths, and a variety of superconductor line widths and lengths. All the etch pits in the arrays have dimensions 105 x 122 μm, with thermally isolated regions measuring approximately 69 μm x 115 μm. Each array is labeled by a letter followed by a

Table 3.1
Step-by-step process sequence for the first process run (without transistors).

Start: 3 - inch silicon (100) wafers

Process Step	Purpose
Deposit Si_3N_4	Bottom of thermally isolated membrane
Ion beam sputter depositions:	
300 Å yttria - stabilized zirconia (YSZ) at 700°C to 735°C	Buffer layer
2100 Å YBCO at 700° to 735°C	Superconductor
100 Å to 300 Å YSZ at ~150°C	Passivation layer
Pattern YSZ/YBCO/YSZ by ion milling	Define electrical paths and pads
Deposit Ag/TiW/Cr on pads	Ohmic contacts to YBCO, diffusion barrier, plasma etch stop.
Deposit SiO_2	Passivation layer
Oxygen plasma	Re-oxidize YBCO
Deposit Si_3N_4	Passivation layer
Plasma etch via cuts on pads	Allows pad metal contact to YBCO
Deposit TiW/Au	Pad metal
Wet etch TiW/Au	Define pads
Plasma etch via cuts into silicon	Allows KOH etchant to reach the silicon.
Etch in hot aqueous KOH	Form thermally isolated microbolometers.
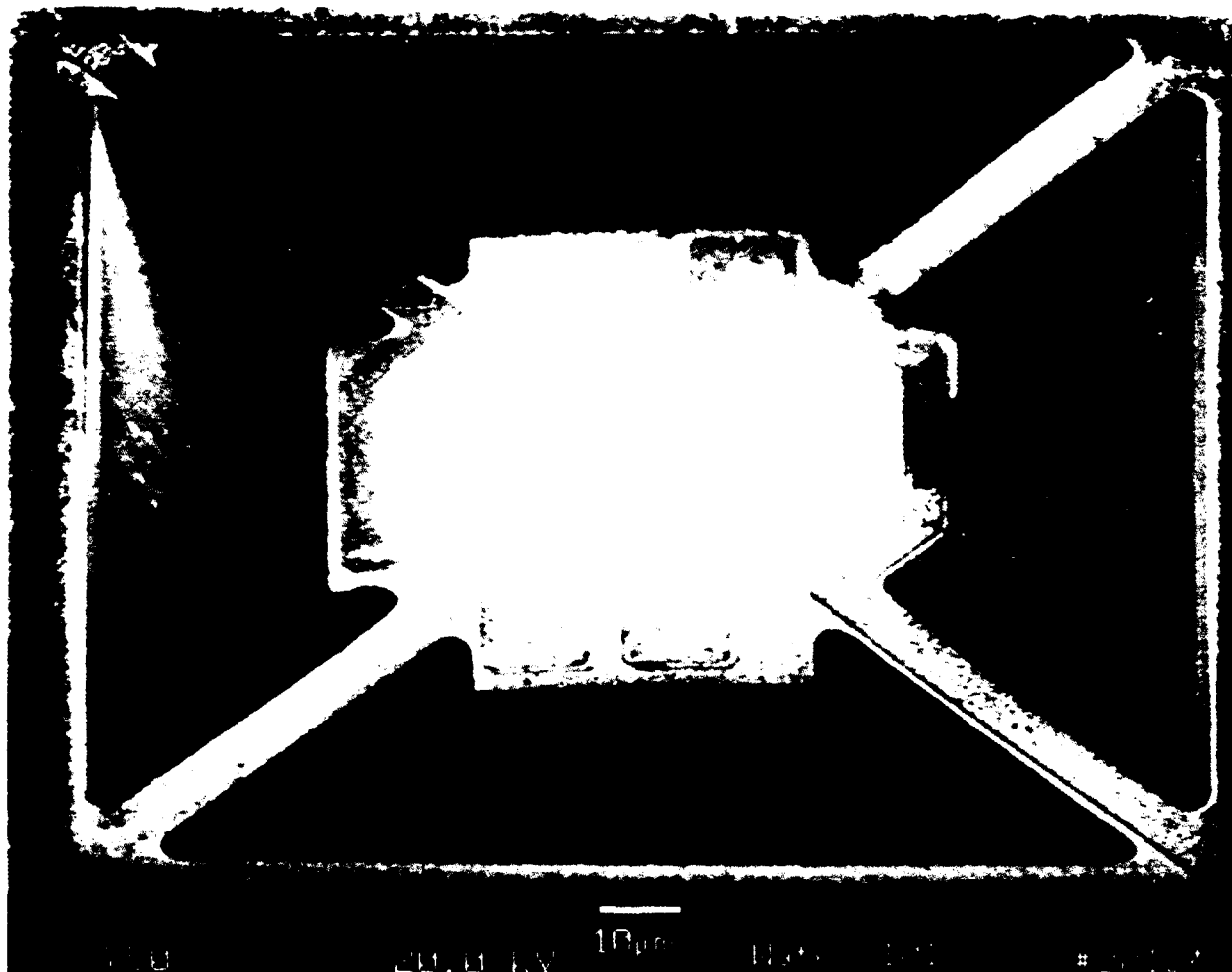
Figure 3.1: An etched thermally isolated membrane suspended above an etch pit in silicon. This structure was fabricated in the first process run. The delaminated bottom surface of the structure has the appearance of a shadow under the support legs. The top layer of the support leg in the upper left of the picture has broken away completely. The superconductor meander line is visible on the top surface of the membrane.
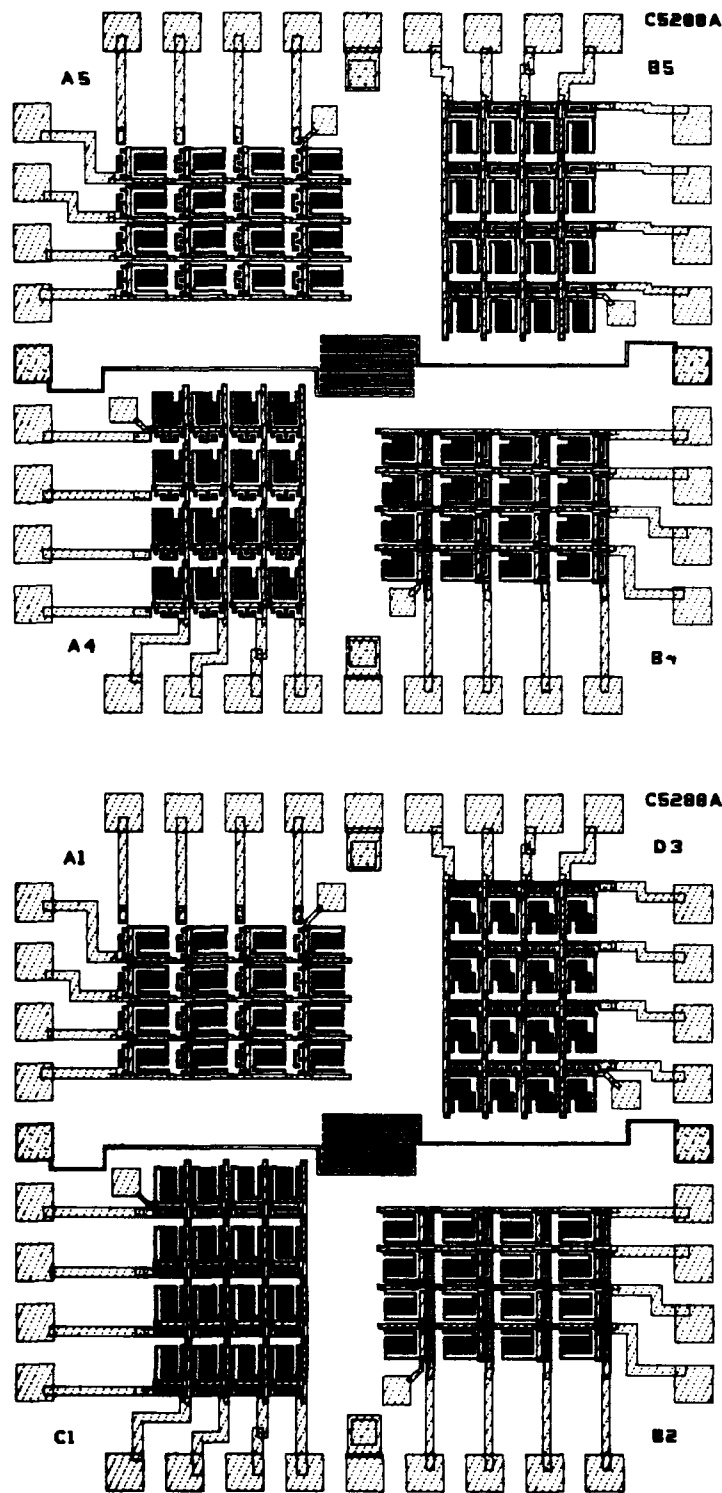
Figure 3.2: Left half of the primary cell of mask set #5288, used to fabricate 4x4 microbolometer arrays.
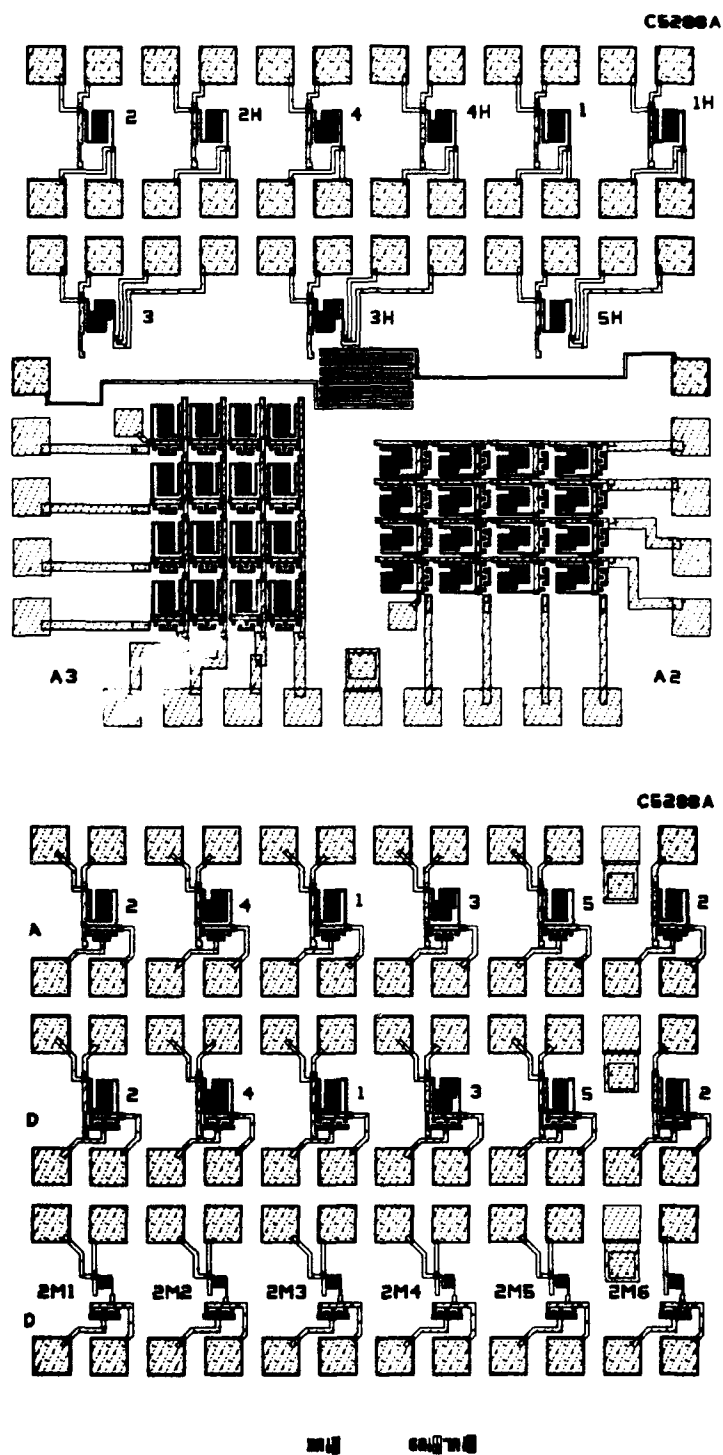
Figure 3.3: Right half of the primary cell of mask set #5288, used to fabricate 4x4 microbolometer arrays.

number (visible in Figures 3.2 and 3.3) designating the transistor type and microbolometer type used in the array.

The primary cell also contains single microbolometers representing all five types of microbolmeters and thermally heat - sunk meander lines identical to those on the microbolometers. Three large heat - sunk YBCO meander lines are provided as sensitive temperature sensors, to stabilize the substrate temperature in close proximity to the arrays. Additional single microbolometers wired with adjacent transistors are also present. Some of these single microbolometers have etch pits only 50 μm on a side. This is the typical size of a pixel in a large imaging array.

The mask set also contains a test cell (see Figures 3.4 and 3.5) which has the same size as the primary cell, and is located at 13 approximately evenly spaced locations over the area of the 3 - inch wafer. The structures visible in Figure 3.4 are a 4x4 array with multiplexers on the rows and columns, a number of transistor test structures (contact resistance, epi layer resistance, etc.), and transistor fabrication process test structures. The structures visible in Figure 3.4 are thermal conductivity test structures, superconductor lines of various widths with four electrical contacts (for measurements of sheet resistance and noise), 4-probe structures to measure contact resistance between the superconductor and the ohmic metal making electrical contact to the sutpercondutor, alignment marks, various kinds of single transistors, several microbolometers only 50 μm on a side, 4-probe structures to measure contact resistance between the superconductor ohmic metal and the pad metal, several fabrication process test structures, and an artist's rendition of Mr. Super Conductor in action.

3.4 Second Process Run Procedure

The objective of the second process run under this contract was to integrate monolithic bipolar transistors with superconductor microbolometers to produce 4x4 arrays with a transistor switch at each pixel to address individual pixels. The mask set described above was used for this purpose. The transistors were fabricated at Honeywell expense by Honeywell's MICRO SWITCH Division and donated to the contract at no expense to the contract. The transistor fabrication is described in Section 4 of this report.

The microbolometer fabrication process used in this process run was a modification of the process used in the Honeywell - funded process run. Working microbolometers with high sensitivity were successfully produced in that process run. However, the electrical contacts to the YBCO superconductor in that process run had significant resistance and were very noisy. Hence, for the 4x4 array process run, gold was deposited in-situ immediately after the YBCO deposition. This technique has been used successfully by other workers to achieve low resistance contacts to YBCO films [1]. This required several other changes in the microbolometer process sequence.

Microbolometer processing was carried out on eight wafers. To measure the performance of microbolometers containing higher quality YBCO films than were available at Honeywell, the YBCO on two of these wafers (#15 and #18) was

26
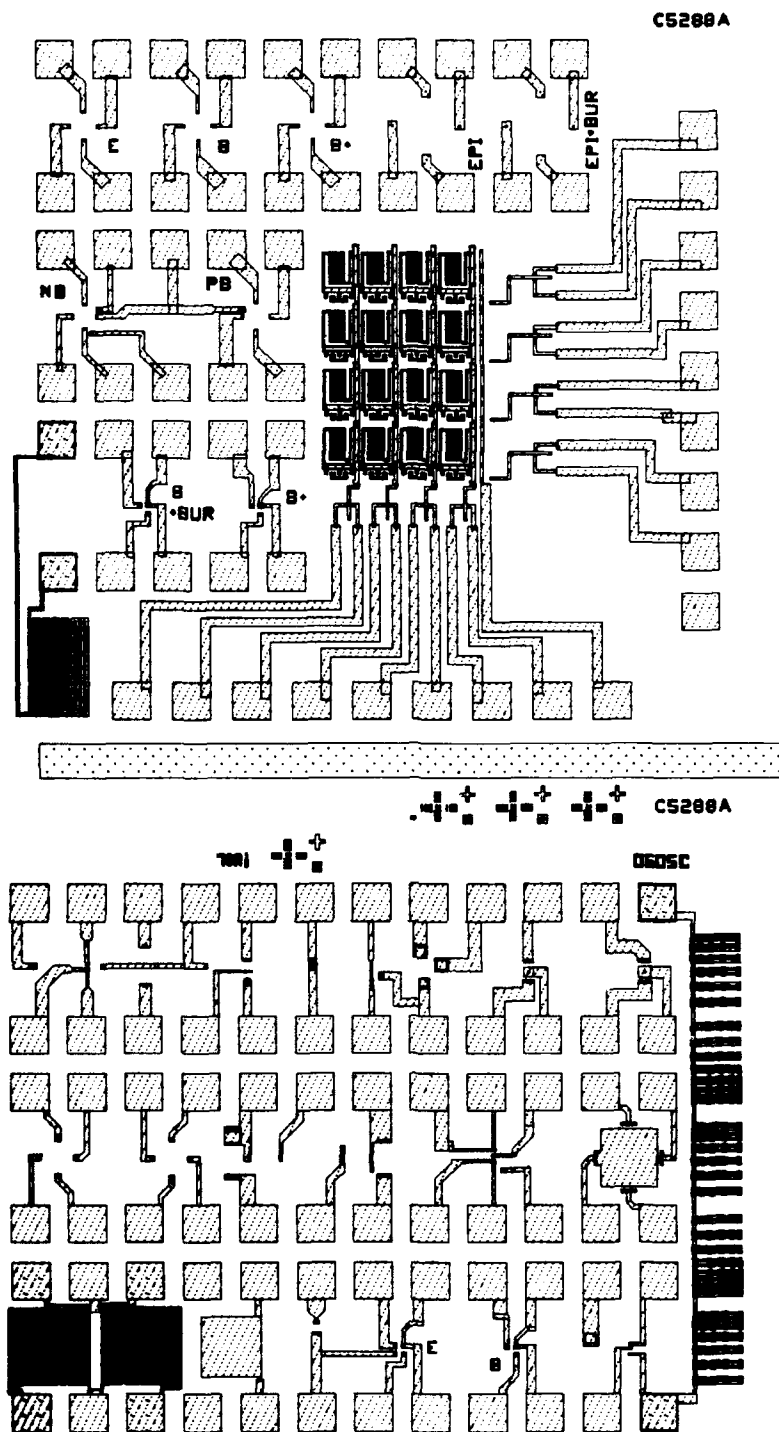
Figure 3.4: Left half of the test cell of mask set #5288. This half contains a 4x4 array with multiplexers, transistor test structures, and transistor process test structures.
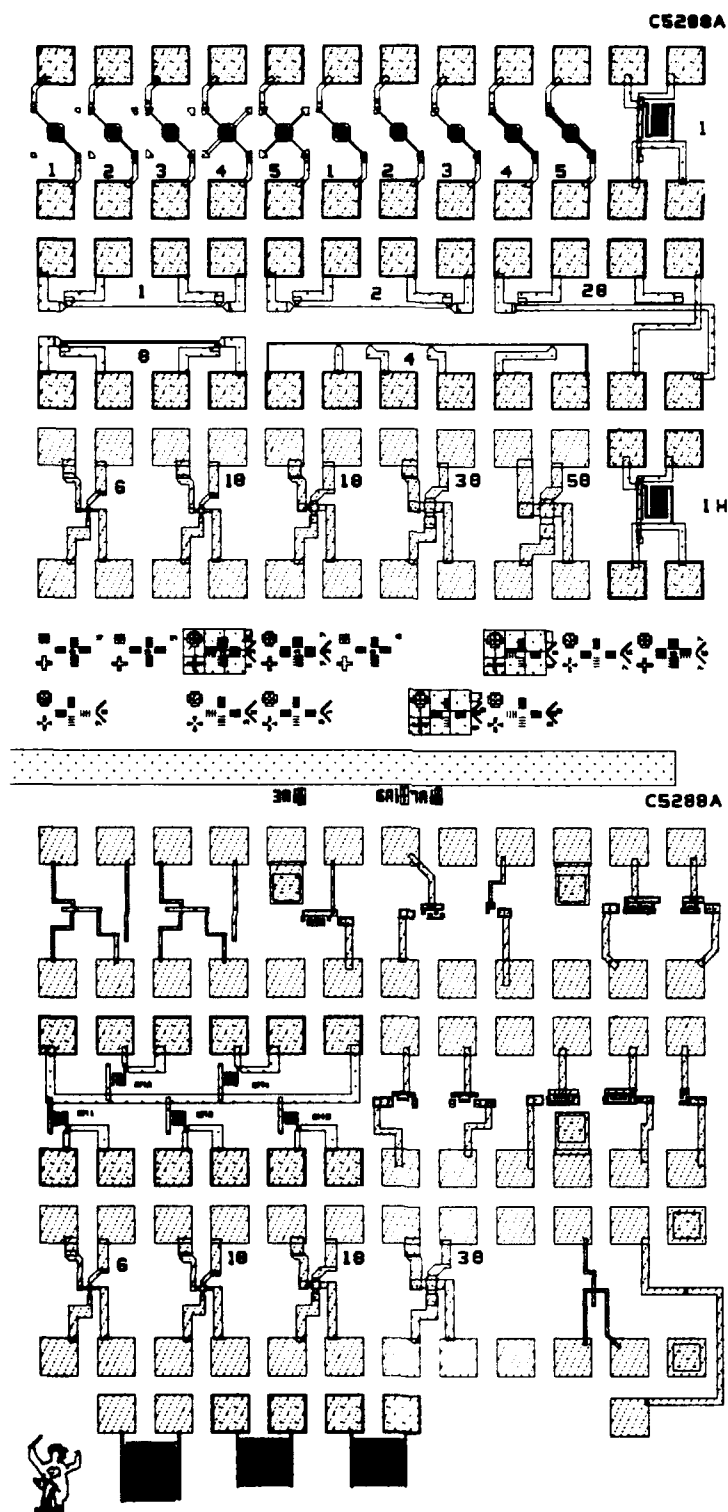
Figure 3.5: Right half of the test cell of mask set #5288. This half contains test structures to measure thermal conductivity, superconductor resistance and noise, and contact resistance, as well as single transistors.

deposited by laser ablation at the Jet Propulsion Laboratory (JPL). The Si$_3$N$_4$ and YSZ on these two wafers was deposited at Honeywell by the same methods used on all the other wafers in the process run.

The process sequence for microbolometer fabrication in the second process run is given in Table 3.2. This process sequence is approximately the same as that used in the Honeywell - funded process run that produced operational microbolometers, with three substantial exceptions. First, a layer of gold was deposited in-situ immediately after the YBCO deposition to produce an electrical contact to the YBCO which had low resistance and low noise. This gold layer was patterned before the YSZ passivation layer was deposited on top of the YBCO. Second, to allow the pad metal to make electrical contact to the transistors, a via cut to the PtSi transistor contacts was performed by plasma etching before the pad metal deposition. Third, at the very end of the process, a rapid thermal anneal was performed to repair radiation damage in the transistors which occurred during processing.

3.5   Second Process Run Results

Operational 4x4 microblometer arrays were not produced in the second process run because of degradation of the YBCO during processing. The transistors performed very well at low temperatures (77 K) after undergoing the entire microbolometer processing sequence. Results on the transistor performance are given in Section 4.

The degradation of the YBCO began early in the microbolometer processing. The room temperature sheet resistance provided a measure of the quality of the YBCO films during microbolometer processing. Before the process run began, while optimizing the YBCO film growth parameters, it was observed that a loose correlation existed between room temperature resistance and superconducting properties such as T$_c$ and the sharpness of the transition. For the YBCO films grown in the second process run, it was not practical to measure the sheet resistance immediately after growth because the low sheet resistance of the 1000 Å thick layer of gold contact metal shorted out the YBCO. However, YBCO films grown at Honeywell immediately before the films for the second process run were grown had a typical sheet resistance of 36 Ω/square immediately after growth, a typical superconducting transition midpoint temperature of ~ 76 K, and a typical transition midpoint temperature coefficient of resistance of 0.17 K^{-1}. The growth parameters for the films used in the second process run were similar to those used for these films, so it is likely that the superconducting properties were similar. The room temperature resistance of the YBCO films grown at JPL was very non-uniform due to the inability of the JPL laser ablation system to cover a 3-inch wafer uniformly, and the small size of the substrate heater used in the JPL deposition system.

After the superconductor had been patterned, the resistance of the YBCO was measured in meander lines similar to those in the 4x4 array pixels and in a 4 μm x 400 μm test structure. The YBCO resistance was typically ~100 Ω/square, indicating that significant degradation of the YBCO had occurred. The damage

Table 3.2
Step-by-step process sequence for the second process run (with transistors).

Start: 3 - inch silicon (100) wafers with monolithic bipolar transistors (PtSi contacts, thermal SiO_2 passivation)

Process Step	Purpose
Deposit Si_3N_4	Bottom of thermally isolated membrane
Ion beam sputter deposit:	
600 Å yttria - stabilized zirconia (YSZ)	Buffer layer
YBCO/Au Deposition:	
Honeywell (ion beam sputtering, wafers #3, 5, 11, 17, 20, 24):	
2000 Å YBCO at 700° to 735°C	Superconductor
1000 Å gold at ~200°C	Ohmic contact metal to YBCO
JPL (wafers #15 and 18):	
laser ablation: 2000 Å YBCO at ~775°C	Superconductor
sputtering: 1000 Å gold	Ohmic contact metal to YBCO
Deposit TiW	Adhesion layer
Pattern Au/TiW by ion milling	Define electrical contacts to YBCO
Oxygen plasma	Re-oxidize YBCO
Deposit YSZ	Passivation layer
Pattern YSZ/YBCO/YSZ by ion milling	Define YBCO electrical paths.
Oxygen plasma	Re-oxidize YBCO
Deposit Si_3N_4	Passivation layer
Deposit and pattern NiCr	IR absorber layer on microbolometers
Deposit Si_3N_4	Passivation layer
Plasma etch via cuts on contacts to YBCO	Allows pad metal contact to YBCO.
Plasma etch via cuts on PtSi contacts	Allows pad metal contact to PtSi.
Deposit and pattern TiW/Au	Pad metal
Plasma etch via cuts into Si	Allows KOH etchant to reach silicon.
Etch in hot aqueous KOH	Form thermally isolated microbolometers.
Rapid thermal anneal	Repair radiation damage in transistors.

occurred uniformly in the patterned YBCO lines, as evidenced by the fact that the sheet resistance was approximately independent of the width of the patterned line.

After completion of all the microbolometer processing steps except the KOH etching and the rapid thermal anneal, the YBCO sheet resistance had increased further. The YBCO films grown at Honeywell showed typical sheet resistances varying from 200 to 300 Ω/square on wafer #24, to 700 to 1500 Ω/square on wafer #20, to >100 kΩ/square on wafers #3 and #11. In low temperature measurements of YBCO films grown at Honeywell, films with these values of room temperature resistance typically have greatly depressed superconducting transitions, if any transition exists at all.

Just before etching in the KOH, the wafers with YBCO deposited at JPL also showed high values of sheet resistance (e.g. 150 to 500 Ω/square in the central portion of wafer #18) indicating that the YBCO on these wafers had degraded, too.

It should be noted that in the Honeywell - funded process run, no significant degradation in room temperature resistance of the YBCO was seen during microbolometer processing, and the superconducting properties of the finished microbolometers were similar to those of freshly grown films. Two possible explanations can be proposed for the degradation of the YBCO in the second process run funded under this contract.

First, the superconducting properties of the YBCO films immediately after growth were not quite as good in the second process run as in the Honeywell - funded process run. The electrical properties of the films used in the Honeywell - funded process run and the second process run are compared in Table 3.3. Many workers have found that YBCO films with superior electrical properties are less susceptible to processing damage. However, the YBCO films grown at JPL also showed high sheet resistance after microbolometer processing. Before microbolometer processing, at the best location on the 3 - inch silicon wafer, these films had superconducting properties superior to the films grown at Honeywell. Films grown at JPL using growth conditions and substrates similar to those used for the films processed in the second processing run showed a typical superconducting transition midpoint at ~87 K. Thus, it seems unlikely that the initial condition of the YBCO films was responsible for the degradation during microbolometer processing.

The second possible explanation for the degradation is the changes in the microblometer processing that were made in the second process run to accomodate the improved YBCO electrical contact process. In the Honeywell - funded process run, the YSZ passivation layer was deposited in-situ immediately after the YBCO deposition. In the second process run, the gold contact metal was deposited in-situ on top of the YBCO. The gold was then patterned before the YSZ passivation layer was deposited. Thus, the YBCO was exposed to processing chemicals and the atmosphere before being coated with the YSZ passivation layer. Assuming the gold acted as a good passivation layer, the only chemical that the YBCO was exposed to (except on the edges of patterned lines) was butyrolactone.

31

Table 3.3
A comparison of electrical properties of YBCO films in the Honeywell - funded process run and the second process run funded by the contract.

Property	Honeywell - funded value (typical)	Second Process run value (typical)
Room temperature sheet resistance	30 Ω/square	36 Ω/square
T_c midpoint	79 K	76 K
Temperature coefficient of resistance at the transition midpoint	0.24 K^{-1}	0.17 K^{-1}

Our previous experience with butyrolactone has been that it does not significantly degrade YBCO. It is possible that the superconductor was damaged when the gold contact metal was removed by ion milling. This may have removed some YBCO and damaged the remaining upper surface of the YBCO film.

If the YBCO degradation was due to patterning of the gold contact metal, there are two approaches that can be taken to solve the problem. Either the in-situ gold contact process can be altered, or an ex-situ contact process can be developed.

It may be possible to alter the in-situ process by using different types of photoresist and developer which are less harmful to the YBCO. Chemical damage could also be prevented with higher quality YBCO films. A thicker layer of gold contact metal would provide additional protection for the YBCO against chemical damage.

Alternatively, an ex-situ process may provide adequately low contact resistance if care is taken in preparing the YBCO surface with a chemical etch or a sputter etch before the contact metal is deposited. If such a process is used, the YBCO would be passivated with YSZ deposited in-situ, to provide immediate protection for the freshly grown YBCO film. At some later point in the microbolometer fabrication process, the YBCO passivation layers would be removed, perhaps by ion milling. The damaged YBCO surface would then be cleaned by either a wet etch (e.g. EDTA or Br-alcohol) or a sputter etch, or both. The contact metal (either Ag or Au) would then be deposited onto the YBCO. Success using this technique has been reported in the literature [1,2]. A contact formed in this way may not have a resistance as low as that of an in-situ contact, but the specific contact resistances reported in the literature for ex-situ contacts (10^{-5} to 10^{-6} Ω-cm^2) would be low enough for use with a microbolometer which is not operating in the superconducting state. The noise in such contacts would have to be measured.

The electrical contacts to the YBCO in the second process run showed contact resistance low enough to meet the requirements for the pixels in a large two - dimensional imaging array of superconducting microbolometers. The contact resistance between the YBCO and the gold was measured using four - probe structures designed for this purpose. These measurements were performed after all microbolometer processing had been completed except the etch in KOH solution. Typically, the contact resistance on wafers with YBCO grown at Honeywell was 1 to 3 Ω on a 18 μm x 18 μm contact. This implies a specific contact resistance of 3 to 9 x 10^{-6} Ω - cm^2. For each pixel in a large imaging array, this would result in a contact resistance of 6 to 18 Ω for the two contacts measuring approximately 10 μm x 10 μm. This is to be compared with the likely pixel resistance of 1 to 5 kΩ.

There was some etching of the YBCO underneath the Au/YBCO contacts, for the first wafer pieces etched in KOH solution. The etching occurred due to inadequate passivation by the gold pad metal. The gold pad metal is exposed to the KOH solution during etching. To provide good passivation at the edges of the via cuts on the Au/YBCO contacts, the gold pad metal should be sputter deposited with a voltage bias during deposition. However, this was not done initially because of

fears that the YBCO would degrade further due to overheating. As a result, the KOH was able to etch the YBCO underneath the contacts, at the edges of the contacts, causing the contact to delaminate at the edges.

This problem of the etching of the YBCO on the Au/YBCO contacts was solved by depositing a second layer of pad metal gold with a voltage bias during sputtering. The success of this technique is illustrated by the results of etching the upper half of wafer #18 in KOH solution (the YBCO on wafer #18 was deposited at JPL). This wafer piece contained 4x4 arrays with up to 13 of the 16 pixels being electrically continuous (see Figure 3.6). The current gain of the transistors on this wafer piece after processing was as high as 21 at 77 K, which is adequate for a large imaging array. Thus, only the degradation of the YBCO during microbolometer processing prevented the arrays on this wafer from being a good demonstration of the integration of YBCO microbolometers with monolithic bipolar transistors.

Most of the microbolometers were mechanically intact after etching in the KOH solution, even though the electrical resistance was too high to be measured on many pixels. The pixels with a measurable electrical resistance typically had resistances of 200 to 500 kΩ on wafer #18. A scanning electron microscope picture of a single pixel in a 4x4 array, with microbolometer and transistor, is shown in Figure 3.7.
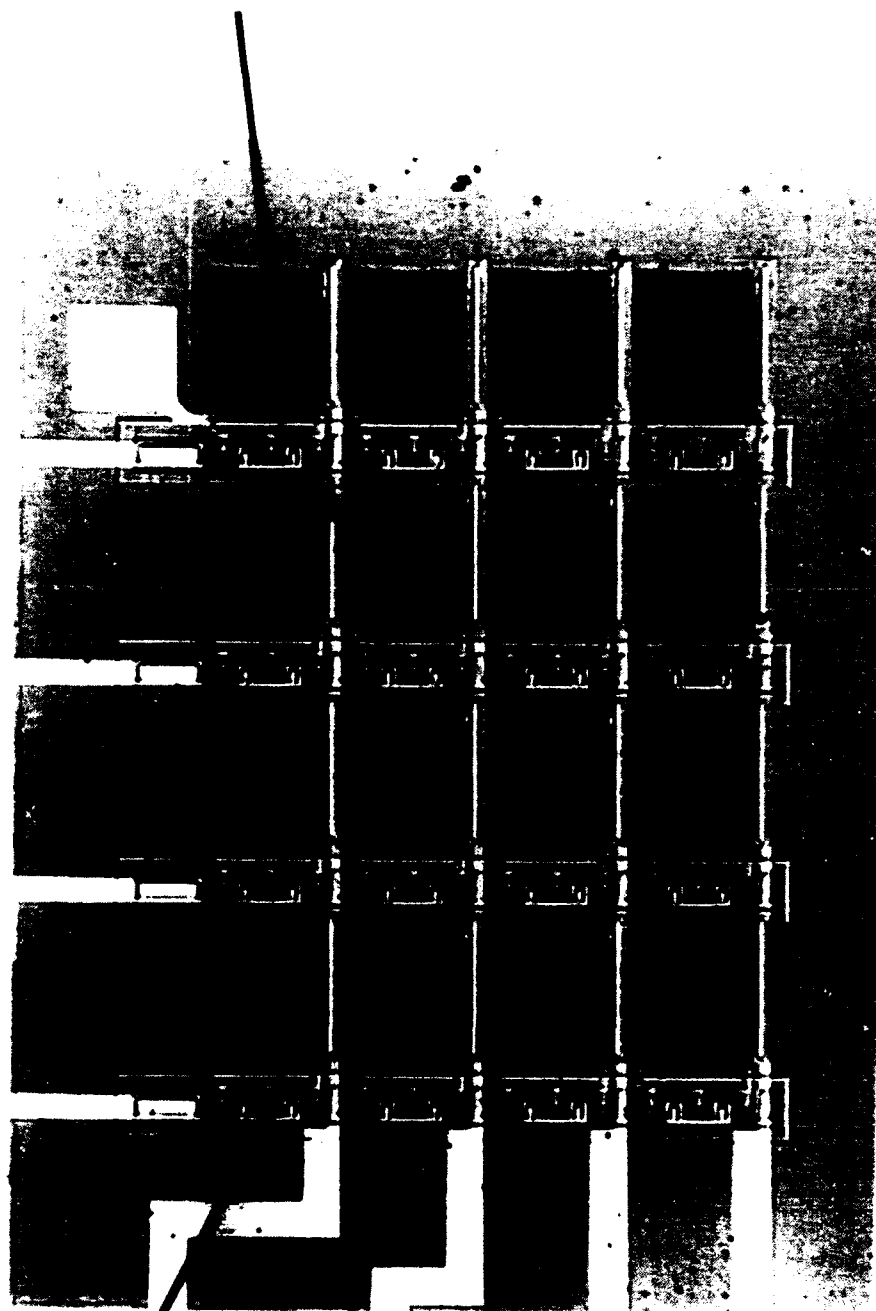
Figure 3.6: Optical microscope picture of a 4x4 microbolometer array (wafer #18, die B5, Array A2). Arrays similar to this one in the same area of wafer #18 had as many as 13 of 16 pixels electrically continuous at room temperature. The superconductor on this wafer was grown at the Jet Propulsion Laboratory.
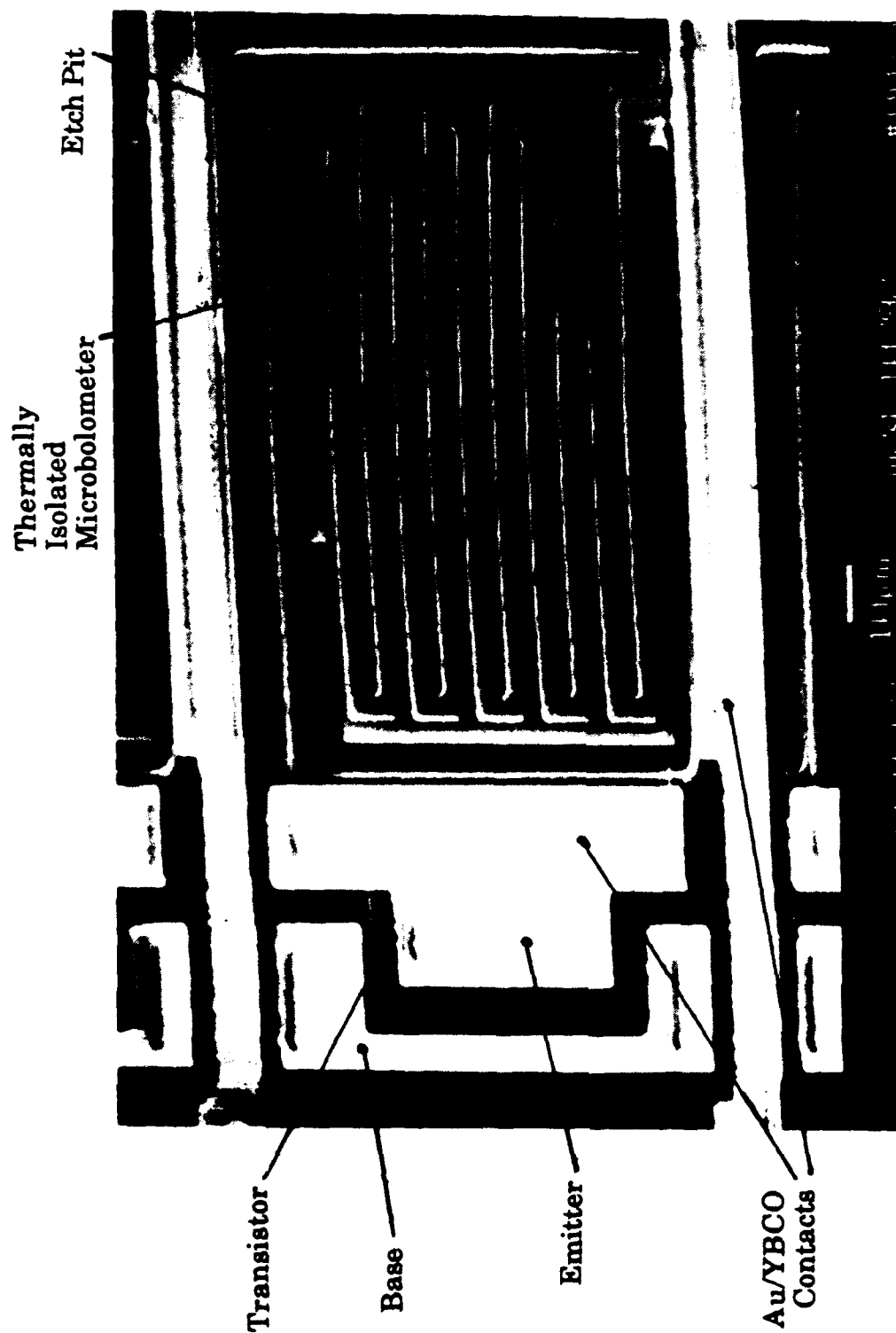
Figure 3.7 : Scanning electron microscope picture of a single pixel in a 4x4 microbolometer array (wafer #24), showing the microbolometer suspended over an etch pit in the silicon wafer, and the transistor. The transistor layout is type B (large contact-emitter stripe), as discussed in Section 4 of this report.

References

1. J.W. Ekin, A.J.Panson, B.A. Blankenship, Applied Physics Letters $\underline{52}$, 331 (1988).
2. M.S. Wire, R.W. Simon, J.A. Liune, K.P. Daly, S.B. Coons, A.E. Lee, R. Hu, J.F. Burch, C.E. Platt, IEEE Transactions on Magnetics $\underline{27}$, 3106 (1991).

4.0 Transistor Fabrication and Impact of Microbolometer Processing

4.1 Introduction

The two major concerns regarding transistors for a high - T_c superconducting microbolometer imaging array are the ability of the transistors to operate at low temperature, and the ability of the transistors to survive the superconductor deposition and the microbolometer fabrication processing steps. Bipolar transistors were chosen for this program because they were thought to be more capable than FET's of surviving the microbolometer processing steps. The performance of bipolar transistors (e.g. the current gain) at low temperature is not as good as at room temperature (in contrast to FET's). However, at the typical operating temperature of a $YBa_2Cu_3O_7$ (YBCO) superconducting transition edge microbolometer (between 77 K and 90 K) bipolar transistors can have significant current gain. In the work performed under this contract, the performance of bipolar trnsistors was shown to meet the requirements for use as switches to address individual pixels in a large imaging array, even after completion of all microbolometer processing.

The high deposition temperature of the YBCO superconductor is sometimes thought to be a serious limitation to monolithic integration of semiconductor electronics with YBCO devices. In fact, many transistor processing steps occur at much higher temperature than the superconductor deposition. The ohmic contacts to the transistor are the only serious concern at the YBCO film *deposition temperature*. This problem can be overcome by using refractory silicides such as PtSi or WSi_2 for the ohmic contacts. PtSi was chosen for the ohmic contacts for this program, because it is a more common material on semiconductor processing lines than is WSi_2. WSi_2 can withstand higher temperatures than PtSi, but the results obtained with PtSi were satisfactory.

The transistors used in the work performed on this contract were fabricated at Honeywell's MICRO SWITCH Division. The transistors were fabricated at Honeywell expense and donated to the contract at no cost to the contract. Mary Weybright, a graduate student working for Prof. Plummer at Stanford University, was hired as a consultant to determine how to modify MICRO SWITCH's standard Opto2 bipolar transistor fabrication process for optimized low temeperature (~77 K) performance. Mary Weybright's thesis work is on the performance of bipolar transistors at low temperatures. Mary Weybright recommended seven process splits for the 24 wafers which were fabricated by MICRO SWITCH. In addition, the mask layout provided four different layouts of the transistors.

The transistor performance was quite good at low temperature, even after the transistors had been through the entire microbolometer processing sequence. One of the processing splits produced transistors with current gain as high as 31 at 77 K. This current gain meets the requirements for a large focal plane imaging array of superconducting microbolometers. The leakage current (also an important performance parameter in a large imaging array) was found to be negligible.

This section of the report was written with substantial contributions from Mary Weybright.

4.2 MICRO SWITCH Fabrication Run

The transistors used on this contract were fabricated at Honeywell's MICRO SWITCH Division at Honeywell expense and donated to the contract at no cost to the contract. It is preferred to use PNP rather than NPN transistor switches at each pixel in a microbolometer array. For this reason, the focus of the work on this program was to optimize the low temperature performance of the PNP transistor. However, MICRO SWITCH's standard Opto2 process is optimized primarily for NPN performance.

Table 4.1 lists MICRO SWITCH's standard Opto2 process flow. The NPN has a buried layer collector with about 6.5 μm of n-type epitaxial silicon (epi) grown on top. The NPN base is formed by a boron implant into the epi and a subsequent drive-in. Afterwards phosphorus is diffused from $POCl_3$ to form the emitter. The NPN extrinsic base is the same as its intrinsic base. The PNP transistor emitter is formed by the NPN intrinsic base implant and diffusion. The n-type epi is the PNP base, and the p-type substrate forms the PNP collector. The PNP extrinsic base region is formed by the n-type epi and the collector plug or sinker diffusion from $POCl_3$. The PNP collector is contacted from the top side.

A total of 24 wafers was processed through the entire Opto2 process in this lot. The wafers were divided into 6 splits as outlined in Table 4.2. Wafers 1 through 3 (the split labeled "1001") followed the standard Opto2 process flow and provided a control set used for comparison with previous Opto2 lots and the non-standard splits in this run.

Three splits were fabricated like the control split, but with a p-type contact implant for the purpose of improving the low temperature contact resistance of p-type regions. The PNP emitter dose varied among these three splits. The contact implant improves room temperature PNP current gain by increasing the emitter Gummel number (the number of impurities per unit area) but may decrease low temperature current gain if the doping is high enough to produce bandgap narrowing. Bandgap narrowing in the emitter of bipolar transistors is the main cause of poor low temperature current gain. The purpose of the three contact implant splits was to determine the optimal PNP emitter doping in the presence of the p-type contact implant. Three wafers (the split labeled "1000") were fabricated like the standard, but with the p-type contact implant. Four wafers (the split labeled "1200") followed the standard process but received half the PNP emitter dose and the p-type contact implant. This emitter was expected to give good contact resistance and at the same time improve the low temperature current gain by reducing bandgap narrowing in the majority of the emitter. To further investigate the optimal emitter doping, four wafers (the split labeled "1100") received a PNP emitter dose twice as high as the standard process, and the p-type contact implant.

39

Table 4.1
MICRO SWITCH standard Opto2 bipolar IC process sequence.

Process Step	Procedure
Substrate	Si <100> $N_A \approx 4 \times 10^{15}$ cm^{-3}
Oxidation	Grow 8000Å SiO$_2$
Buried Layer Lithography	Mask 1
Strip Oxide	Wet Etch
Buried Layer Implant	Sb, 150 KeV
Buried Layer Drive-in	Diffusion
Strip Oxide	Wet Etch
Field Oxide	Grow 6500Å SiO$_2$
Isolation Temperature Schedule	1090°C Deposition, Diffusion
Sinker Deposition Temperature Schedule	1000°C Deposition
Sinker Diffusion	Diffusion
Strip Oxide	Wet Etch
Re-grow 2450Å Field Oxide	975°C Oxidation
NPN Base/PNP Emitter Implant	Boron implant
Implant Anneal and Drive-in	Diffusion
Resistor Diffusion	Diffusion
Strip Oxide	Wet Etch
Diffusion	Diffusion
Deposit POCl$_3$	600Å
NPN Emitter Diffusion	Diffusion

Table 4.2
Wafer splits in the MICRO SWITCH transistor fabrication process run.

Split	Wafer #'s	PNP Emitter	PNP Base
1001 - Control	1, 2, 3	5.2×10^{14} cm^{-2}	2.3×10^{15} cm^{-3}, 6.5μm
0001 - Higher Base Dose	4, 5, 6, 10, 11, 12	Same as Control	1×10^{16} cm^{-3}, 5.5μm
1011 - Special NPN Emitter	21, 22, 23, 24	Same as Control Except Different Diffusion Temperature	Same as Control Except Lower Dose Extrinsic Base
1000 - Contact Implant	7, 8, 9	Same as Control Plus p-type Contact Implant	Same as Control
0000 - Contact Implant and Higher Base Dose	None		
1100 - Contact Implant and Higher Emitter Dose	13, 14, 15, 16	1×10^{15} cm^{-2} with p-type Contact Implant	Same as Control
1200 - Contact Implant and Lower Emitter Dose	17, 18, 19, 20	2.6×10^{14} cm^{-2} with p-type Contact Implant	Same as Control

41

One split (the split labeled "0001") was added to improve base resistance and investigate the preferred range of PNP base dose. These six wafers followed the standard process but had a base formed by $1x10^{16}$ cm^{-3}, 5.5 μm thick epi in place of the standard $2.2x10^{15}$ cm^{-3}, 6.5 μm thick epi.

The final split (the split labeled "1011") used a special NPN emitter in which the POCl$_3$ was deposited at a lower temperature and the phosphorus was diffused at a higher temperature. This NPN emitter was meant to have a lower emitter dose and was primarily for the investigation of optimal NPN emitters.

The masks contained four different transistor layouts. These were labeled as follows: A (small contact-emitter stripe), B (large contact-emitter stripe), C (large contact-sinker stripe), and D (small contact-sinker stripe). Due to a mask layout error, type C was not functional. Schematic diagrams of the four layouts are shown in Figure 4.1. The contact size (large or small) refers to the emitter contact size. The large contact devices had one large PNP emitter contact, whereas the small contact devices had three small PNP emitter contacts. The "sinker stripe" devices had a PNP base contact with NPN emitter diffusion and sinker diffusion over an area consisting of two small contact regions and a stripe connecting them. The "emitter stripe" devices were similar to the sinker stripe devices, except that there was only emitter diffusion (no sinker diffusion) in the stripe connecting the two small PNP base contact regions.

4.3   MICRO SWITCH Fabrication Run and PNP Room Temperature Measurements

Two errors were made in the implementation of the transistor fabrication run. First, wafers meant to have a $1x10^{16}$ cm^{-3}, 5.5 μm thick epi and the p-type contact implant were made without the contact implant. This was not a terrible loss to the run because these wafers (wafers #10, 11, 12), along with wafers #4 through 6, have this non-standard epi. Devices from wafers #7 through 9 followed the standard Opto2 processing with the addition of the contact implant. Expected results of the missing split could be extrapolated if desired from the measured results on these two sets of devices.

The second error was the use of the PtSi contact mask for the p-type contact implant. In this step, boron was inadvertently implanted into the PNP n-type base contact region and the NPN emitter and collector contacts. Fortunately, the phosphorus in the PNP base contact region appears to have compensated the boron so that the extrinsic base is n-type. Since the NPN devices were not measured, the impact of this error on NPN devices was not determined.

The current gain measured at V_{ce} = 4 volts and I_b = 4 μA was used to make a straightforward comparison of the performance of transistors on different wafers. Unless stated otherwise, all the current gain measurements in this report were made under these conditions. Table 4.3 compares typical room temperature results from DC measurements of the PNP's from the different

PNP Emitter

**Sinker Diffusion
(for contact to
PNP base)**

(a)

NPN Emitter Diffusion

(b)

(c)

(d)

100 μm
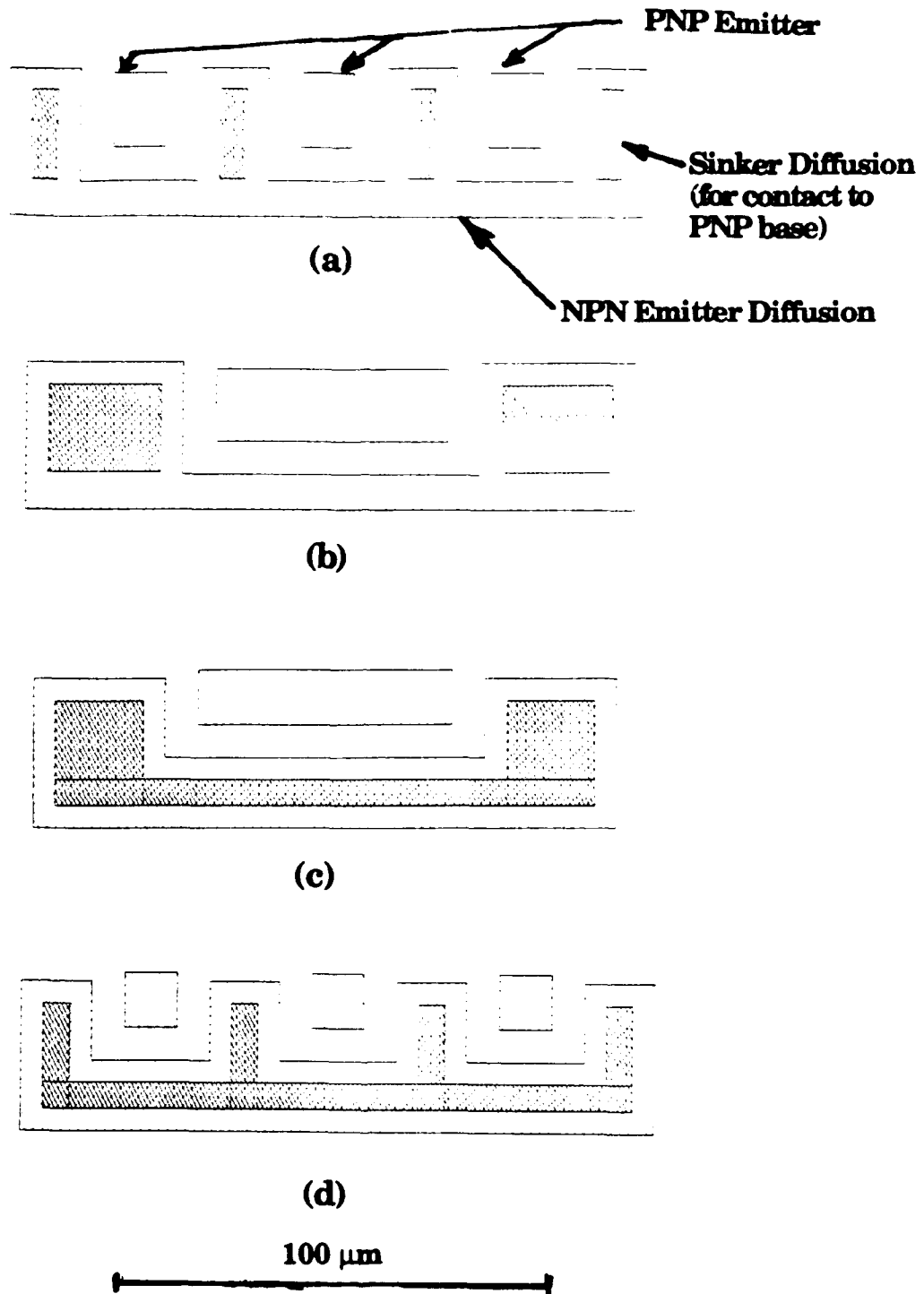
Figure 4.1   The four PNP transistor layouts on the mask set. (a) type A (small
contact-emitter stripe), (b) type B (large contact-emitter stripe), (c)
type C (large contact-sinker stripe), (d) type D (small contact-sinker
stripe). Only the base and emitter are shown. The collector is the
wafer substrate. Contact to the collector is made with a pad
elsewhere on the die.

43

Table 4.3
Room temperature vertical PNP results from transistors with the type B (large contact-emitter stripe) layout.

Split	Relative I_c vs. V_{be}	Relative I_b vs V_{be}	Average h_{fe} ($V_{ec} = 4.0$ V, $I_b = 4.0$ μA)
1001 - Control			71
0001 - Higher Base Dose	Less than Control	Like Control	19
1011 - Special NPN Emitter	Like Control	Less than Control, Better Ideality	111
1000 - Contact Implant	Like Control, but Resistive E-C Short	Less than Control	152
1100 - Contact Implant and Higher Emitter Dose	Like Control, but Resistive E-C Short	Less than Control; like Contact Implant Split	178
1200 - Contact Implant and Lower Emitter Dose	Like Control, but Resistive E-C Short	Less than Control; like Contact Implant Split	129

splits, using transistors with layout type B (large contact-emitter stripe).
Nearly all of the initial characterizations of the transistors at room temperature
were performed on the transistors with this layout.

Examining the data from the control wafers in Table 4.3 gives a comparison of
the results obtained with the type B transistor layout for the PNP's to the results
typically obtained in the standard Opto2 process. Figures 4.2 and 4.3 show
typical Gummel plots of the PNP collector and base current for one of the
control wafers (wafer #3) and for a wafer from a previous Opto2 run.
Throughout this report the previous Opto2 run will be referred to as Opto2 and
devices from wafers #1 through 3 will be referred to as control devices. The
differences between Opto2 and control vertical PNP devices are the layout and
the lack of a forming gas anneal of the control PNP's.

Two main results are evident from the Gummel plots: 1) The Opto2 PNP's have
less low bias emitter-base leakage current. 2) The Opto2 devices have a higher
DC current gain, h_{fe}. The control PNP's have higher emitter-base leakage
current because they did not have a forming gas anneal. This low temperature
anneal in a hydrogen ambient is normally used to passivate the dangling bonds
at the silicon-SiO_2 interface in the emitter-base depletion region. It was omitted
from this process run because the superconductor processing that follows the
transistor fabrication is done at 700°C so any hydrogen would escape during
this step. Furthermore, the forming gas anneal cannot be done after the
superconductor processing because the hydrogen would damage the
superconductor.

The control PNP's have a lower h_{fe} than the Opto2 PNP's because of the
different layouts. Two - dimensional device simulations of the Opto2 and the
control vertical PNP structures using PISCES show two reasons for the
different current gains (Figures 4.4 and 4.5). First, in the Opto2 vertical PNP
structure, the parasitic lateral PNP has a shorter neutral base width than the
intrinsic vertical device. This allows a significant number of holes to be injected
from the emitter periphery into the lateral base and be collected by the collector.
This augments the collector current for a given bias. In the control vertical
PNP, the lateral base width is larger and the extrinsic base portion is more
heavily doped than the vertical base so there is no injection of holes from the
emitter into the extrinsic base. Even if the Opto2 and control devices had the
same emitter area, the difference in lateral geometry would result in the Opto2
PNP having higher room temperature collector current for a given bias
condition.

The second reason that the new vertical PNP's have a lower current gain is the
difference in the emitter contact areas of the two structures. A significant
portion of the base current is due to injection into the emitter and recombination
at the emitter contact. This is "short emitter" current. The new vertical PNP
has six times the emitter contact area per unit emitter area. Again, 2-D device
simulations verify that this increases the base current in the new PNP's and
thus decreases their current gain. Although decreasing the emitter contact
area would increase current gain, this would also increase emitter resistance
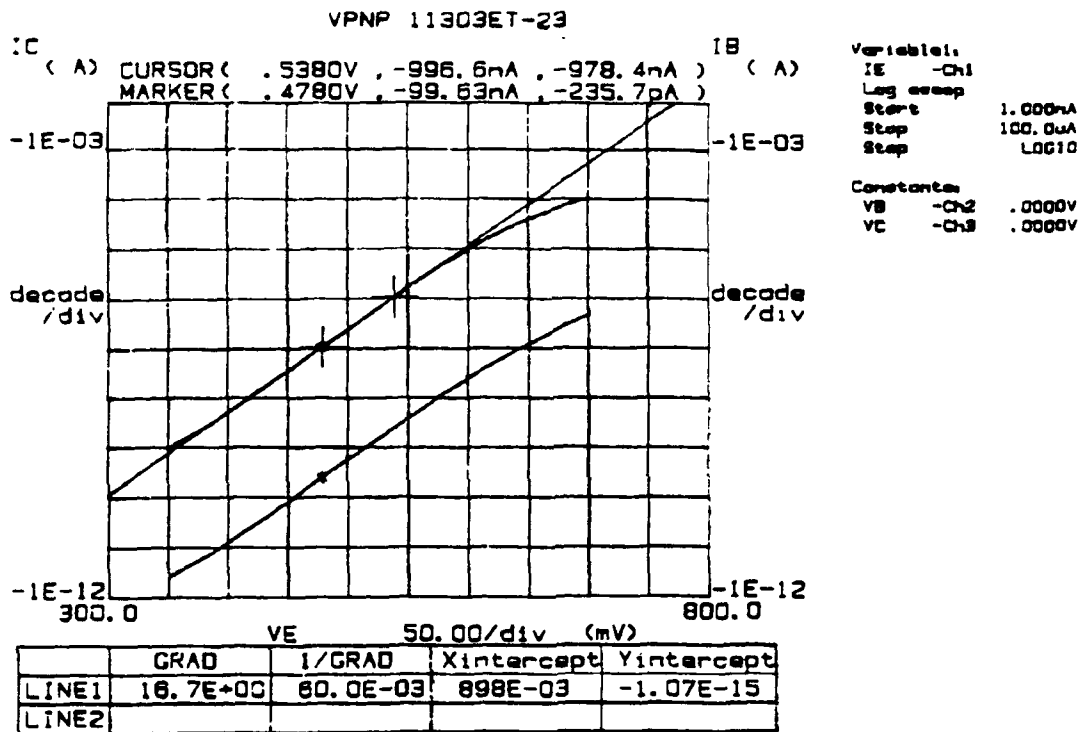
Figure 4.2: Typical Gummel plot for Opto2 vertical PNP at room temperature. The emitter dimensions are 13 μm x 13 μm. Wafer 11303ET-23. (Data from Wayne Killian, Honeywell MICRO SWITCH Optoelectronics, Richardson, TX).

Current (A)

1.00E+00
1.00E-01
1.00E-02
1.00E-03
1.00E-04
1.00E-05
1.00E-06
1.00E-07
1.00E-08
1.00E-09
1.00E-10
1.00E-11
1.00E-12
1.00E-13

0   0.1   0.2   0.3   0.4   0.5   0.6   0.7   0.8   0.9   1

Vemitter

♦ Ib

□ Ic

Gummel Number:
1.5 x 10^{12} cm^{-2}
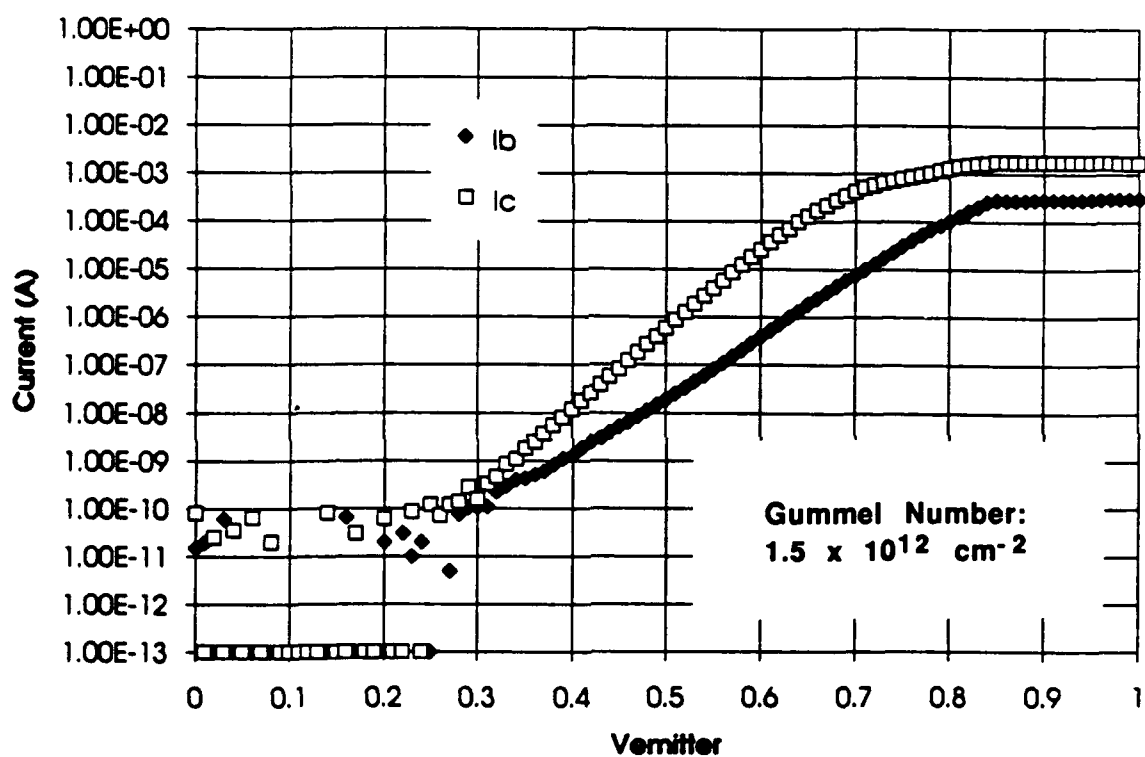
Figure 4.3: Typical Gummel plot for vertical PNP with layout type B from the MICRO SWITCH process run for this contract at room temperature. The emitter dimensions are 53 μm x 16.5 μm. Wafer #3.

47
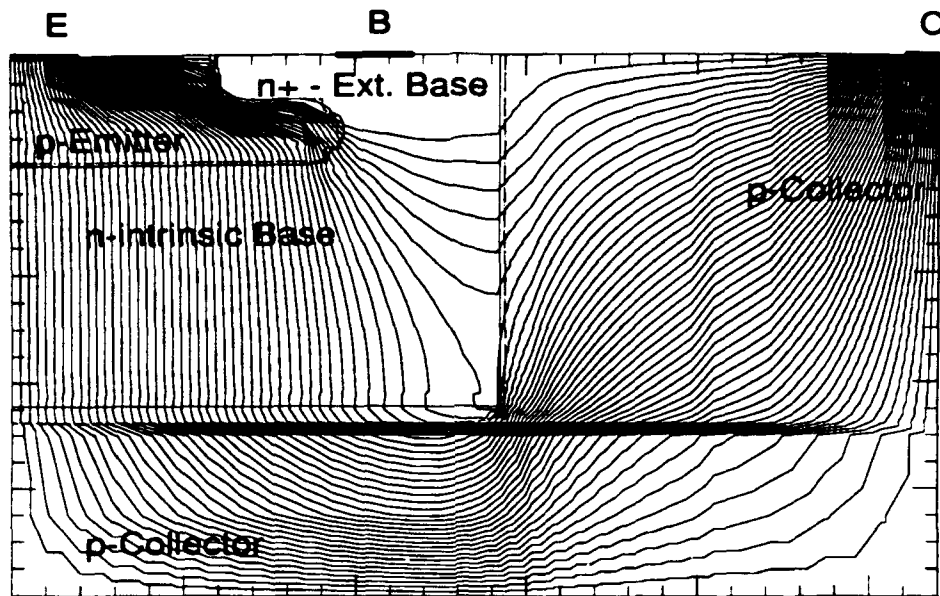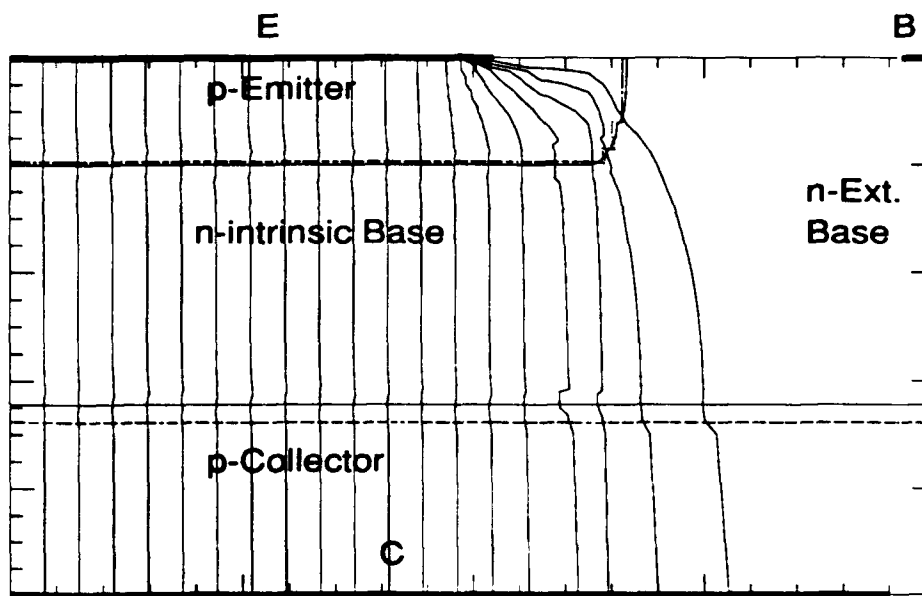
Figure 4.4: PISCES simulation results of hole current flow in half of the emitter/base/collector cross section. (a) Opto2 vertical PNP. 2% of the hole current flows between adjacent lines. Note the hole flow from the emitter into the collector. (b) Vertical PNP from the process run for this contract. 5% of the hole current flows between adjacent lines. There is no hole flow from the emitter into the extrinsic base. $V_{eb} = 0.6$ V, $V_{bc} = 0$ V, $T = 300$ K.
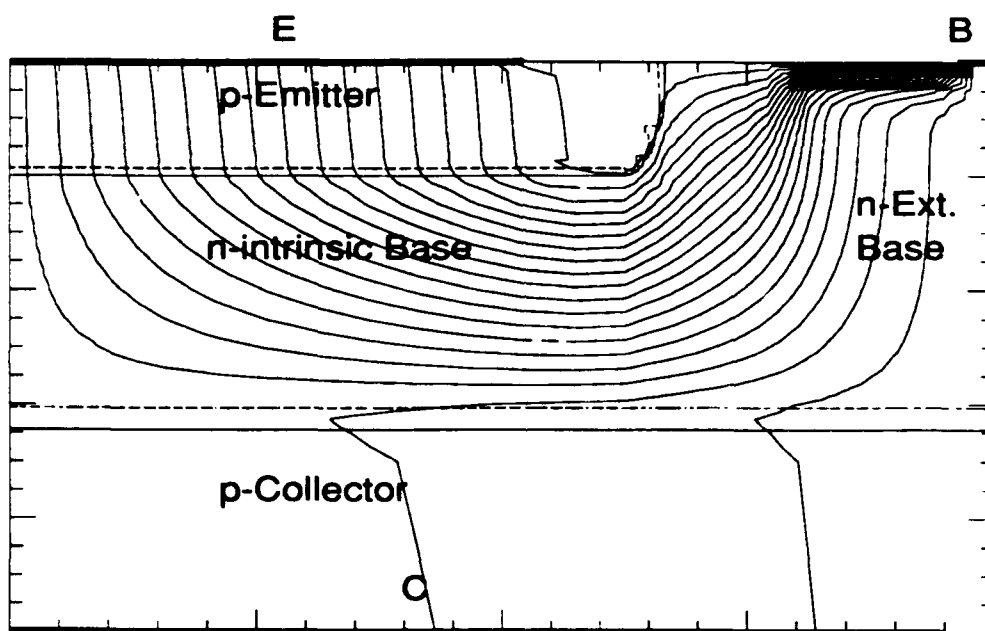
Figure 4.5: PISCES simulation results of electron current flow in half of the emitter/base/collector cross section of the vertical PNP from the process run for this contract. 5% of the electron current flows between adjacent lines. Note that the electron flow is beneath the emitter contact. V_{eb} = 0.6 V, V_{bc} = 0 V, T = 300 K.

which decreases switching speed and decreases the maximum collector current. In general, it is probably best to maximize the emitter contact size, but further study would allow the choice of optimal emitter contact size for the PNP.

As expected, the boron contact implant reduced the room temperature base current in the vertical PNP compared to devices without the implant because of the higher emitter Gummel number. Most of the devices with a contact implant have emitter - to - collector resistive shorts. This can be seen in the low bias region of the Gummel plots. See Figure 4.6 for an example. The isolation and superconductor processing appear to remove these shorts, but their source remains a mystery. Table 4.4 lists possible mechanisms for the emitter - collector shorts with the supporting and conflicting evidence for each hypothesis. It seems unlikely that the shorts are between the emitter and collector pads across the surface of the wafers, because the collector pad is many hundreds of microns away from the emitter contact. Another possible explanation for the shorts is that the measurement station used to make the Gummel plots may have had a short between the emitter and collector probes. However, it seems improbable that this short would have coincidentally occurred only in the measurement of the contact implanted devices.

There are a number of other important pieces of information that can be obtained from the 300 K data. First, the leakage current of the measurement system itself is approximately $1x10^{-11}$ A to $1x10^{-10}$ A. For most devices, the actual leakage current is at or below this limit, so the split with the best leakage current cannot be determined from this room temperature data.

The devices with the highest room temperature current gain were from the split with twice the normal PNP emitter (NPN base) dose and with a PNP emitter contact implant (the split labeled "1100"). This is because the PNP emitter Gummel number is highest for this split. The problem with this split is that there are emitter-collector shorts after the MICRO SWITCH processing (but before the superconductor deposition and microbolometer processing) as discussed above. The high value of h_{fe} at room temperature does not imply that this device would have the highest low temperature h_{fe} because bandgap narrowing in the emitter can in some cases lower the current gain below that of a device with a more lightly doped emitter at low temperature.

The current gain can be improved somewhat by reverse biasing the base-collector junction as seen in the transistor I_e vs. V_{ce} curves (Figure 4.7). Since the base is lightly doped, the depletion region extends into the base and shortens the neutral base width with increasing reverse bias on the base-collector junction.

The devices with the special NPN emitter (the split labeled "1011") had the best I_b vs. V_{be} ideality. This is especially important because non-idealities in I_b, although insignificant at the normal room temperature operating bias of a bipolar transistor, can dominate the low temperature DC characteristics of the device and significantly reduce the current gain. In fact, the transistors on the one wafer from this split that went through the entire microbolometer process
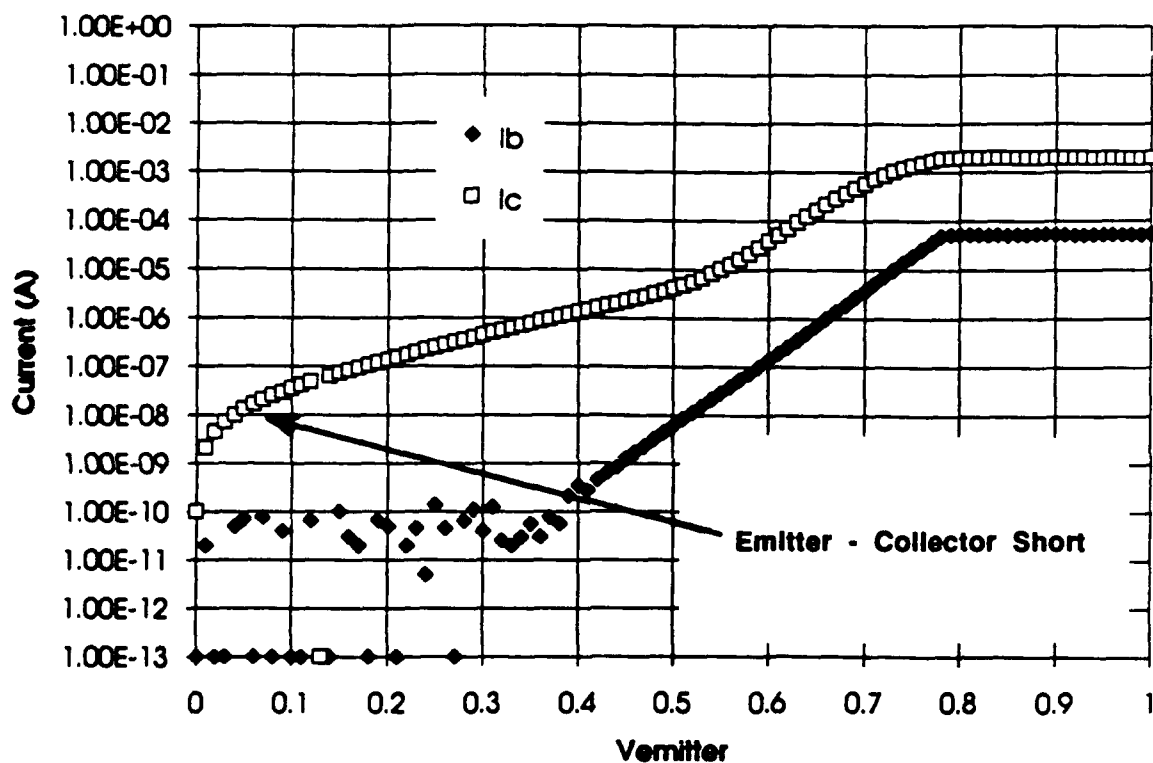
Figure 4.6: Typical Gummel plot for vertical PNP with layout type B from wafer #13 at room temperature. The emitter dimensions are 53 μm x 16.5 μm. Note the collector-emitter resistive short at low V_{eb}.

51

Table 4.4
Possible emitter-collector short mechanisms for the PNP transistors.

Mechanism	Supporting Evidence	Conflicting Evidence
PtSi spiking through emitter and base to collector due to excess stress from contact implant.	E-C short only on devices with contact implants.	1. Base is not shorted to collector on all but one device. 2. Short appears to go away after further processing.
PtSi short between emitter and collector pads on surface.		1. Collector pad is far from emitter pad so would expect base to be shorted to emitter and collector too, but it is not. 2. Would expect to see this problem even on wafers without contact implant.
Short is in measurement equipment not device.		All contact implanted devices have E-C shorts and all devices without contact implant do not.
Emitter and collector diffusions overlap.		1. Collector plug diffusion is very far from emitter diffusion. 2. This problem would occur for even non-contact implant splits.
Contact implant is implanted in over-lapping regions.	Would only occur on contact implanted wafers.	E-C shorts are likely to disappear with further processing.

3.00E-04

2.50E-04

2.00E-04

Ie 1.50E-04

1.00E-04

5.00E-05

0.00E+00

-5.00E-05

Ileak=-1.7e-10 Amp

0   -1   -2   -3   -4   -5

Vce

- Ib=0uA
- Ib=-1uA
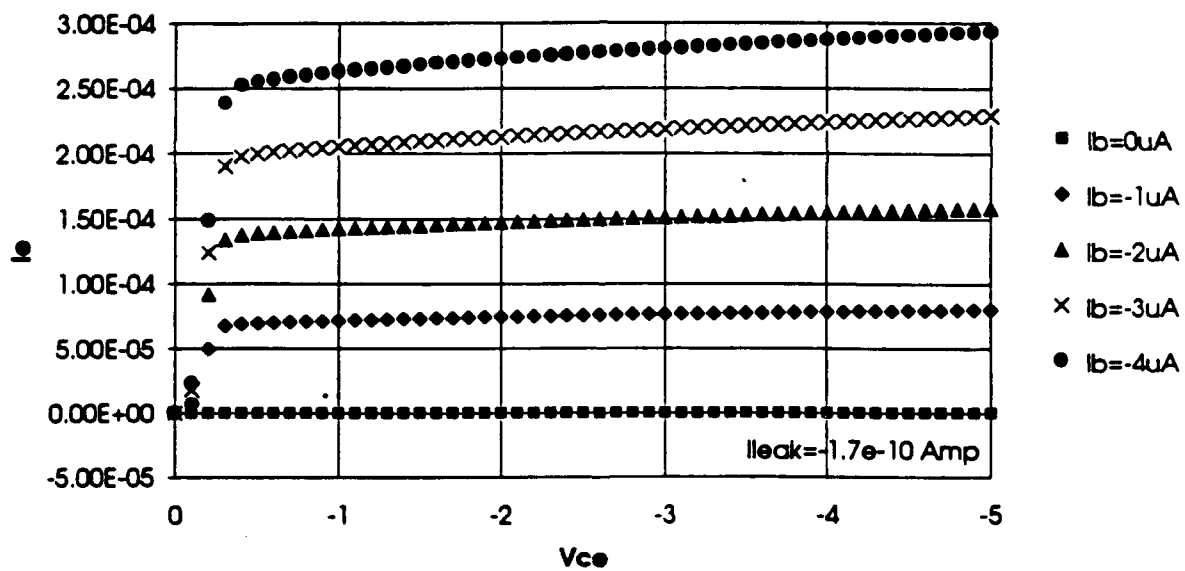- Ib=-2uA
- Ib=-3uA
- Ib=-4uA

Figure 4.7: Typical transistor I-V curves for a vertical PNP with layout type B from wafer #3 at room temperature. The emitter dimensions are 53 μm x 16.5 μm. Note the Early effect.

sequence (wafer #24) had higher current gain after microbolometer processing than any of the other wafers that went through the microbolometer processing. The reason for the more ideal devices in this split is not clear. This emitter was deposited at a lower temperature (850°C rather than 975°C) and diffused at a higher temperature (1000°C rather than 975°C). The NPN emitter doping is contained within the n-type epi of the PNP extrinsic base so it should not greatly impact the emitter-base leakage current. It may be that the higher temperature of the special NPN diffusion cycle annealed damage at the emitter-base junction and/or moved the emitter-base junction away from traps at the surface or in the bulk. The next step in analyzing this improvement would be to determine whether the non-ideal base current is perimeter or area dependent. Comparing base current measurements of transistors with different emitter-base perimeter to area ratios can help discern the source of leakage currents.

4.4 Impact of Microbolometer Processing on the Transistors

The complete microbolometer processing sequence (including the YBCO superconductor deposition) was carried out on eight of the wafers. Tests of individual steps of the microbolometer processing sequence were carried out on the rest of the wafers.

During microbolometer processing, all the wafers showed large decreases in current gain. After completion of all the microbolometer processing steps except the KOH etch and the rapid thermal anneal, the current gain for the transistors with the type B layout (large contact-emitter stripe) was typically between 1 and 10 at room temperature on almost all the wafers (wafers #3, 5, 11, 15, 17, 18, 20). The only exception was wafer #24, which showed current gains ranging from 15 to 30 at room temperature.

At low emitter-base bias, the decrease in room temperature current gain during microbolometer processing was due to an increase in emitter-base leakage current and the base current overall (Figure 4.8). This was true for wafers with and without the p-type contact implant, but the effect seemed to be somewhat worse for devices with the p-type contact implant.

An anneal experiment was conducted to determine the impact of the temperature cycle of the superconductor deposition with and without an underlying layer of Si_3N_4. The results of this experiment are compared in Figures 4.9 and 4.10. It appears that either the deposition of Si_3N_4 or the temperature cycle with the Si_3N_4 covering the devices contributes most to the degradation of current gain. Since the Si_3N_4 is sputter deposited at a low temperature, it seems most likely that the degradation in I_b is due to sputter damage. Because of the thick underlying SiO_2, it is most probable that traps are created in the silicon near the silicon-SiO_2 surface by ultra-violet radiation.

The etch in the KOH solution did not significantly change the current gain. However, after the etch in the KOH solution, a rapid thermal anneal (RTA) at 380°C for 10 sec in air caused the current gain to increase dramatically. On

—— Wafer 5 - after Microswitch (no p-contact implant)
—— Wafer 5 - before Metal Pads (no p-contact implant)
— - — Wafer 20 - after Microswitch (p-contact implant)
— - — Wafer 20 - before Metal Pads (p-contact implant)

Before Pad Metal

After MICRO SWITCH Processing
(before microbolometer processing)

$Ib(A)$

10^{-5}
10^{-6}
10^{-7}
10^{-8}
10^{-9}
10^{-10}

0.40   0.45   0.50   0.55

Veb (V)
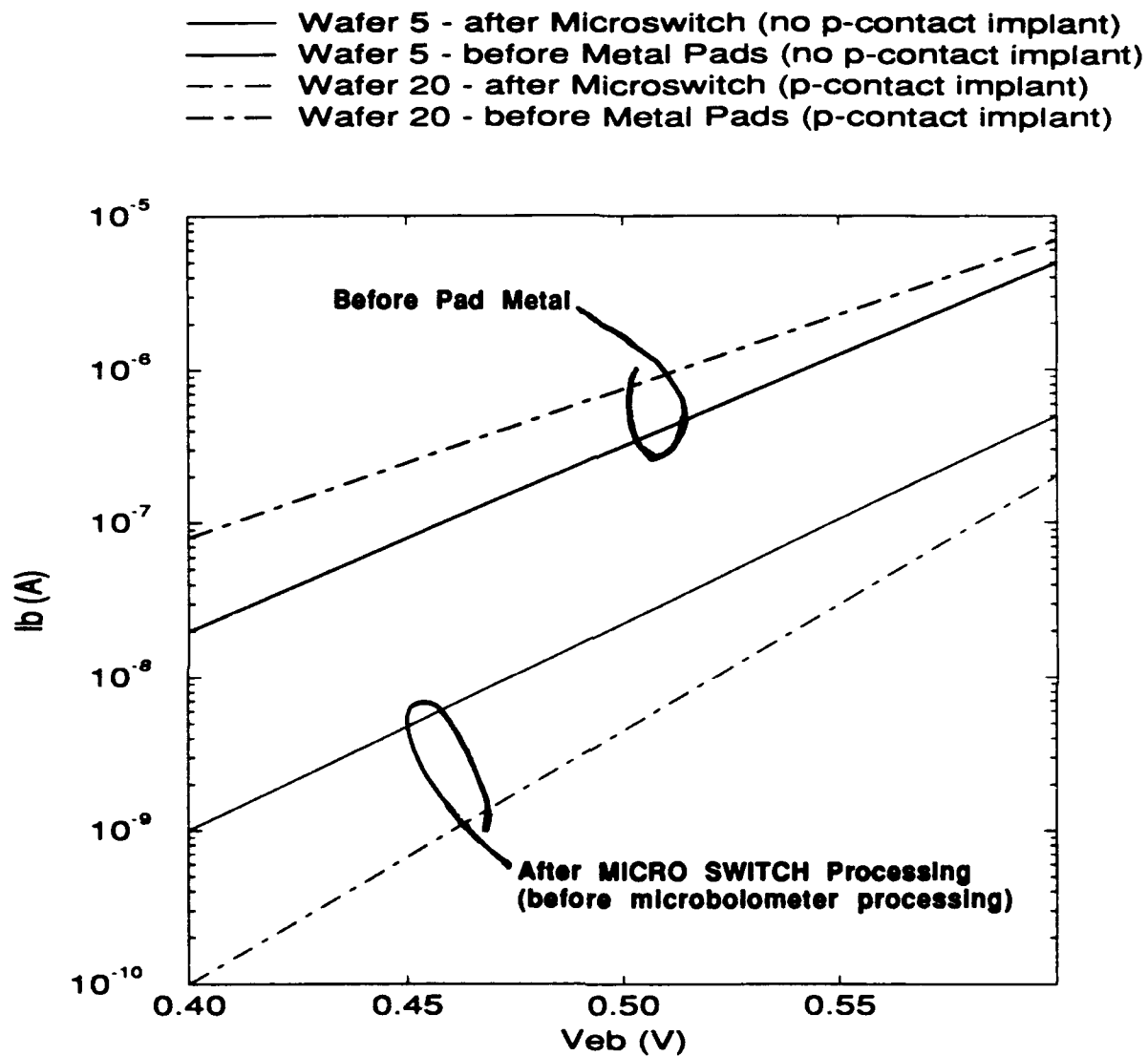
Figure 4.8: Impact of microbolometer processing (up to just before pad metal
deposition) on room temperature PNP base current. The transistor
from wafer #5 has higher base current before microbolometer
processing because of the lower emitter Gummel number. Devices
with and without the p-type contact implant suffered base current
increases and ideality degradation during microbolometer
processing.

55
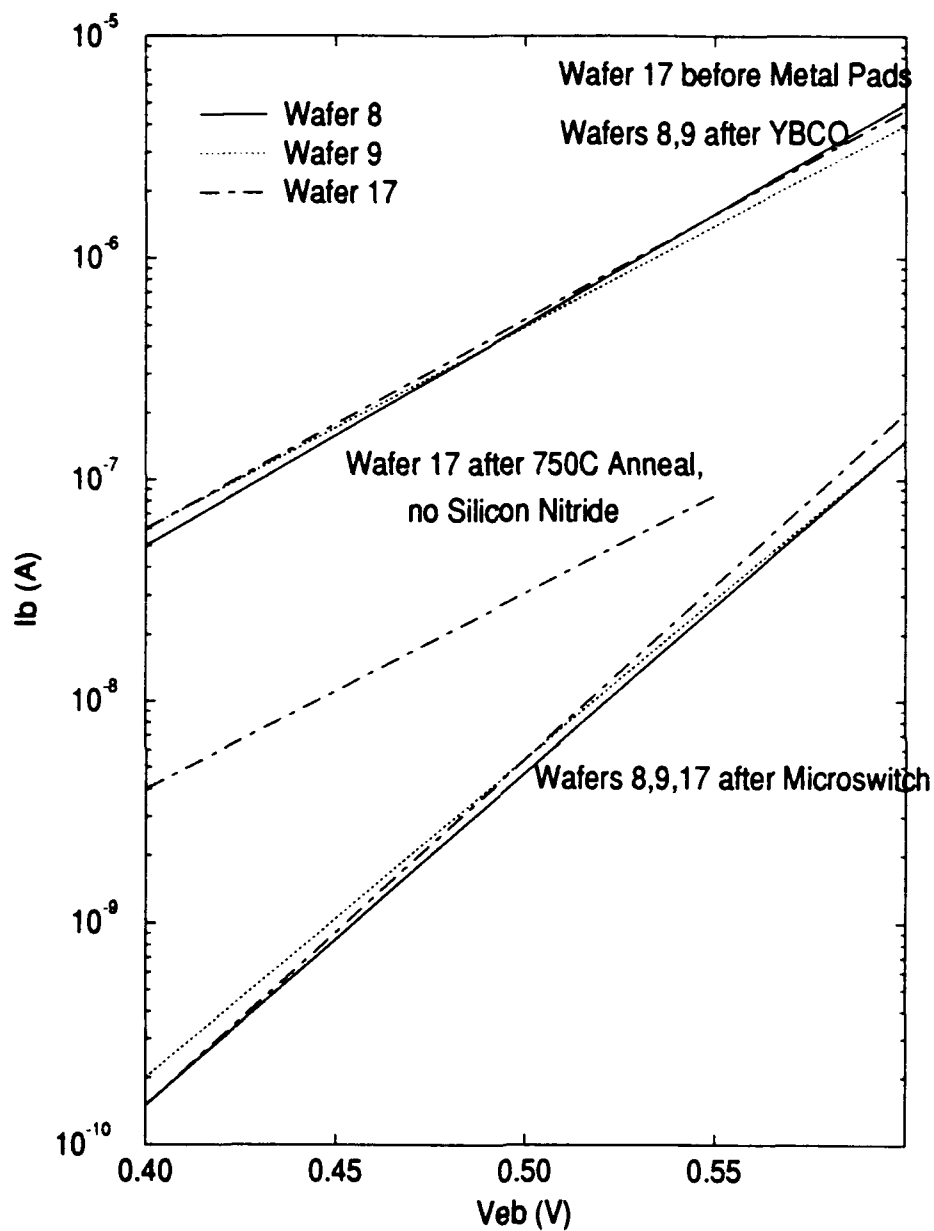
Figure 4.9: Impact of microbolometer processing on room temperature PNP base current for wafers #8, 9, and 17. The 750°C, 4 hour anneal without any other microbolometer processing degrades the base current ideality. This anneal alone does not account for the increase in base current seen by devices which go through the silicon nitride deposition, superconductor deposition, and patterning.

---- Wafer 13 - after Microswitch (p-contact implant)
---- Wafer 13 - after 750C 4hr, with Nitride (p-contact implant)
·········· Wafer 23 - after Microswitch (no p-contact implant)
·········· Wafer 23 - after 750C 4hr, no Nitride (no p-contact implant)
— - — Wafer 24 - after Microswitch (no p-contact implant)
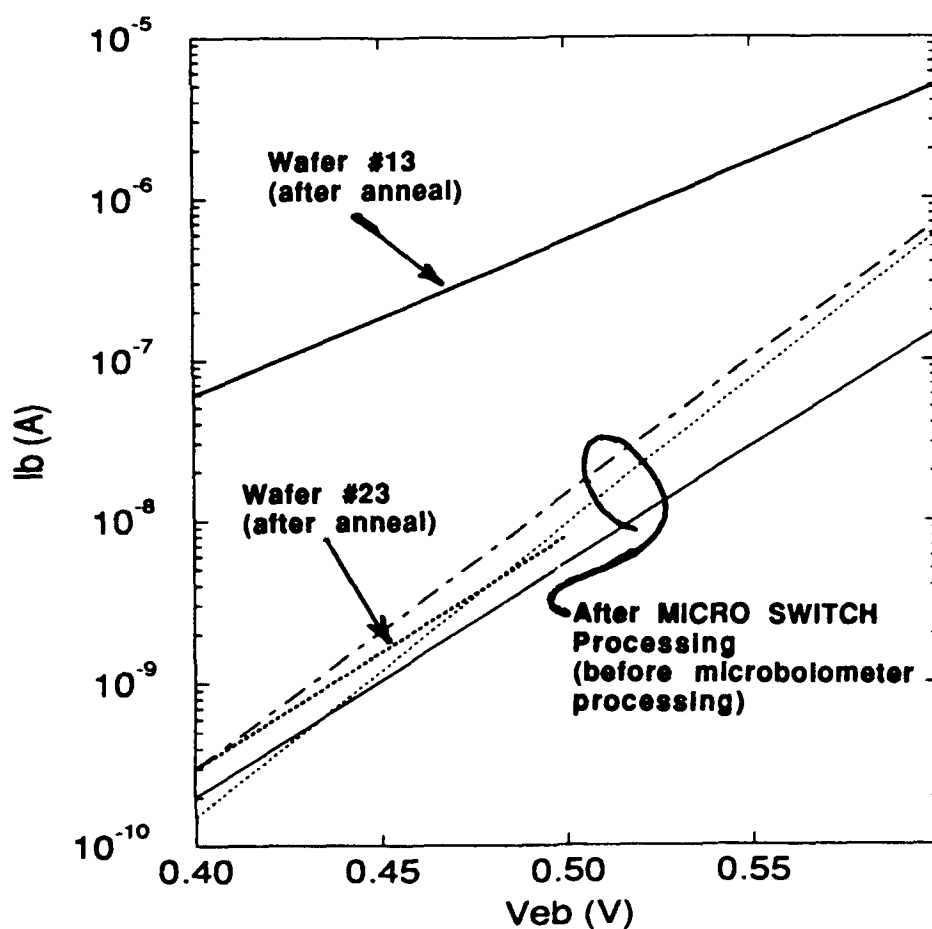
Figure 4.10: Impact of the superconductor temperature cycle (here represented by a 750°C 4 hour anneal) and the first silicon nitride deposition in the microbolometer process sequence on the PNP base current at room temperature.

wafer #18, the room temperature current gain of the transistors with the type A layout (small contact-emitter stripe) increased from approximately 3 to as high as 180. For the transistors on this wafer with the type B layout (large contact-emitter stripe), the current gain increased from a range of 6 to 12 before the RTA to as high as 113 after the RTA. On wafer #24, the current gain of the transistors with the type B layout increased from a range of 15 to 30 before the RTA to as high as 110 after the RTA.

The RTA appeared to reduce the base current and improve the base current ideality. The most likely mechanism for the improvement is the completion of dangling bonds at the silicon-SiO$_2$ interface with hydrogen as would occur in a forming gas anneal. Although hydrogen was not purposely introduced during the RTA, it may exist within the metal layers on top of the silicon such as can happen with Al or in the form of water vapor in the annealer.

Measurements of devices with different emitter perimeter to emitter area ratios allow determination of emitter-base leakage current sources. The measurements on a fully processed wafer, wafer #18, which had half the standard NPN base dose and a p-type contact implant, give insight into the base current components. After completion of the entire microbolometer processing sequence, including the RTA in air at 380°C for 10 seconds, non-ideal base current at room temperature and 77 K is primarily perimeter dependent. The non-ideal emitter-base leakage at 77 K is due to Shockley-Hall-Read (SHR) recombination in the emitter base depletion region at the Si-SiO$_2$ interface. The ideal portion of the base current is primarily area dependent. This provides further evidence that the degradation of the base current with microbolometer processing was due to the formation of traps at the Si-SiO$_2$ interface.

Gummel plots taken before and after a 750°C anneal on a PNP transistor on wafer #23 indicate that the superconductor deposition may increase emitter or base resistance. This resistance increase was not seen in PNP's from wafer #13 or 17. All three wafers had the p-type contact implant in p-type and n-type regions. It may be that there was poor contact between the measurement probes and wafer #23 devices during the post-anneal measurements. This is a common measurement problem. On the other hand, the lower NPN special emitter dose in combination with the erroneous p-type contact implant into the PNP extrinsic base may be at fault. It may be that the lower emitter dose in the extrinsic base is greatly compensated by the erroneous p-type contact implant into that region. The 750°C anneal may have lowered the extrinsic base surface concentration enough to increase the contact resistance.

4.5 Low Temperature Measurements

Measurements of the bipolar transistors at low temperature (77 K) showed that the transistor performance meets the requirments for a large two - dimensional imaging array of superconducting microbolometers. Simulations of such an array, carried out under Honeywell funding, have shown that a current gain of 20 is adequate for such an array. Current gains in excess of this (as high as 31) are reported below. The leakage current of the transistors was negligible at

77 K. This is important in a large imaging array, to avoid crosstalk between pixels.

The low temperature current gain was measured before microbolometer processing on wafer #16. Gold pads for wire bonding were deposited and patterned. This caused some reduction in the room temperature current gain, from ~180 to ~120 on the transistors with layout B (large contact-emitter stripe). No RTA was performed after the metallization. At 70 K, transistors with layout type B showed a current gain of 16.5.

Low temperature measurements were performed on wafer #18 after all microbolometer processing was completed, including a RTA. At 77 K, the die that was measured showed a current gain of 20.6 for a transistor with the type A layout (small contact-emitter stripe) and 13.7 for a transistor with the type B layout (large contact-emitter stripe). The Gummel plot and transistor I-V curves are shown in Figure 4.11 for the type A transistor. The transistors from wafers #16 and 18 which have been measured at low temperature exhibit low V_{eb} bias leakage current and some non-ideal collector current. The emitter-collector shorts are not evident even though these devices had the p-type contact implant. The non-ideal collector current at 77 K and 70 K may be due to freeze-out in the base and the changes in transport mechanisms at low temperature. The emitter-base leakage current appears to be perimeter dependent SHR recombination in the emitter-base depletion region near the silicon-SiO$_2$ interface as discussed in the previous section.

Wafer #24 exhibited the best low temperature performance, as well as the best room temperature performance of all the wafers that completed the microbolometer processing. A die from this wafer was measured at low temperature after completion of all microbolometer processing, including the RTA. At 77 K, the current gain was measured on all three of the measurable PNP transistor types. The data are summarized in Table 4.5. Transistor type D had the highest current gain, with a current gain slightly higher than type A. As on wafer #18, type B had the lowest current gain. The Gummel plot and transistor I-V curves at 77 K for the type D transistor on wafer #24 are shown in Figure 4.12.

The two transistor layouts that gave the best 77 K current gain (types A and D) both have the small - contact emitter with three 12 μm x 16.5 μm emitter regions. It appears that the small - contact emitter transistors have a higher current gain for two reasons. First, the base resistance is lower for the small - contact emitter so that the base current does not roll over as soon as for the single large - contact emitter transistor (type B). Second, the small area of the contacts in the small - contact emitter devices may reduce base current as discussed earlier.

The leakage current was measured on all three transistor types on wafer #24 at 77 K. With V_{ec} = 4.0 volts, I_e was measured and found to be negligible (~< 100 pA) for V_{bc} = 3.0 to 4.0 volts, for all three transistor types. For V_{bc} ~< 3.0 volts,

(a)

(b)
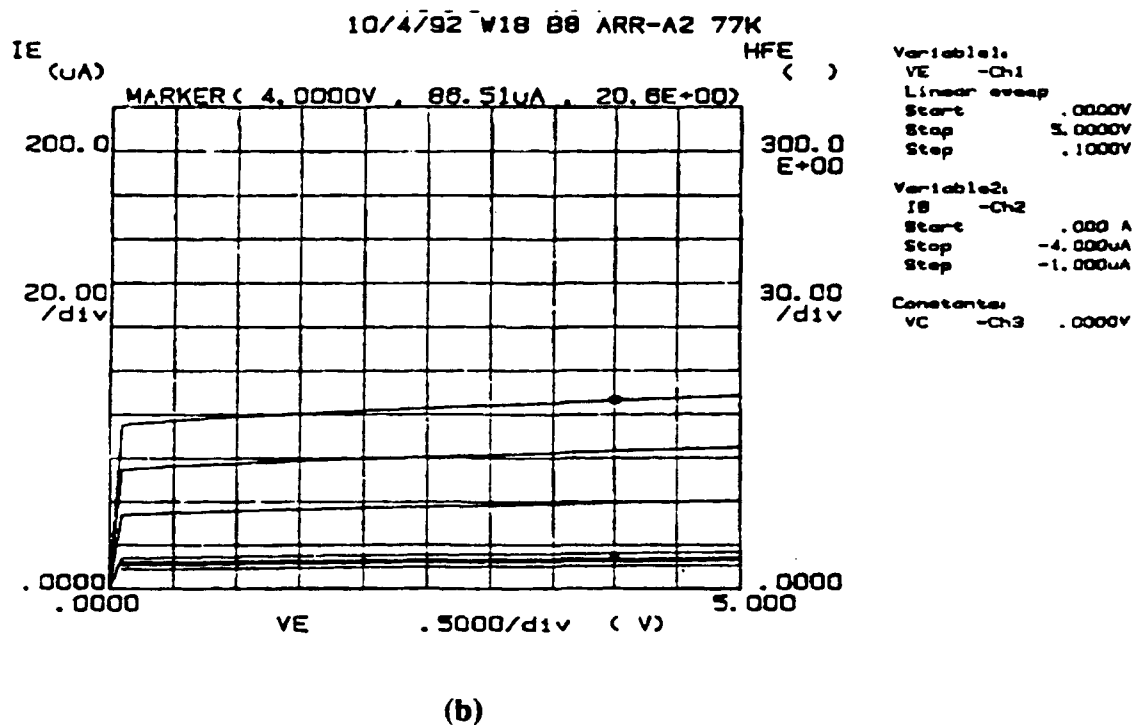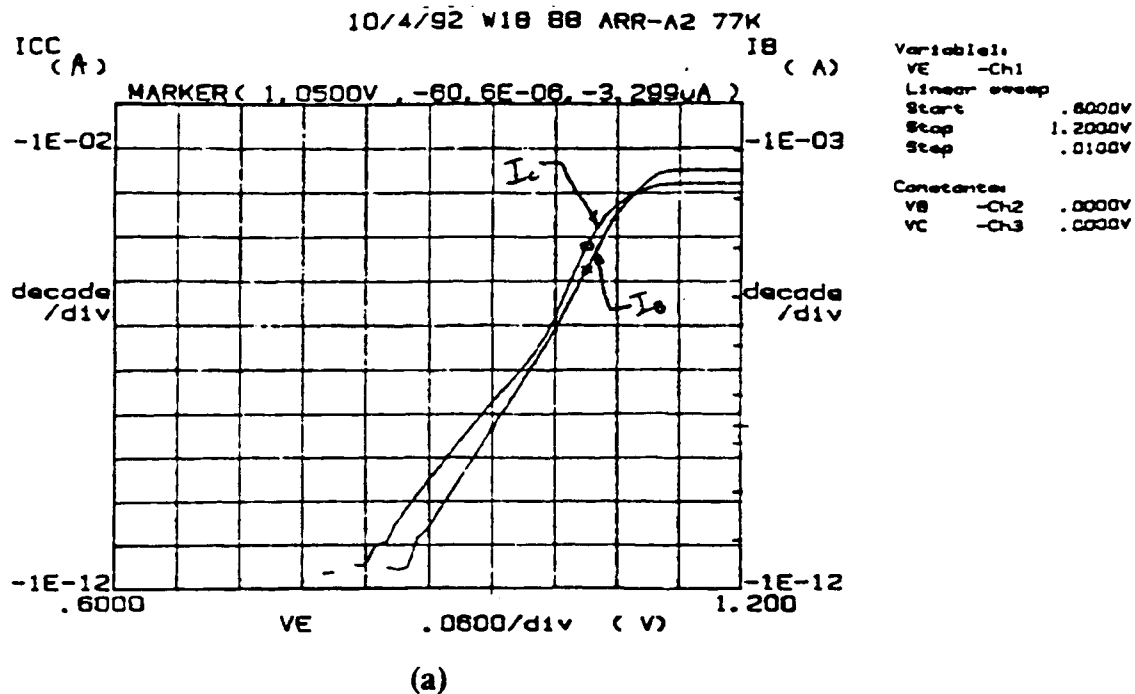
Figure 4.11: (a) Gummel plot and (b) transistor curves for a PNP from wafer #18 at 77 K, after completion of the YBCO deposition and all microbolometer processing, including the rapid thermal anneal. This transistor has three emitter contacts (layout type A). The dimension of each emitter contact is 12 μm x 16.5 μm. The current gain for V_{ec} = 4.0 V and I = 4 μA is 20.6.
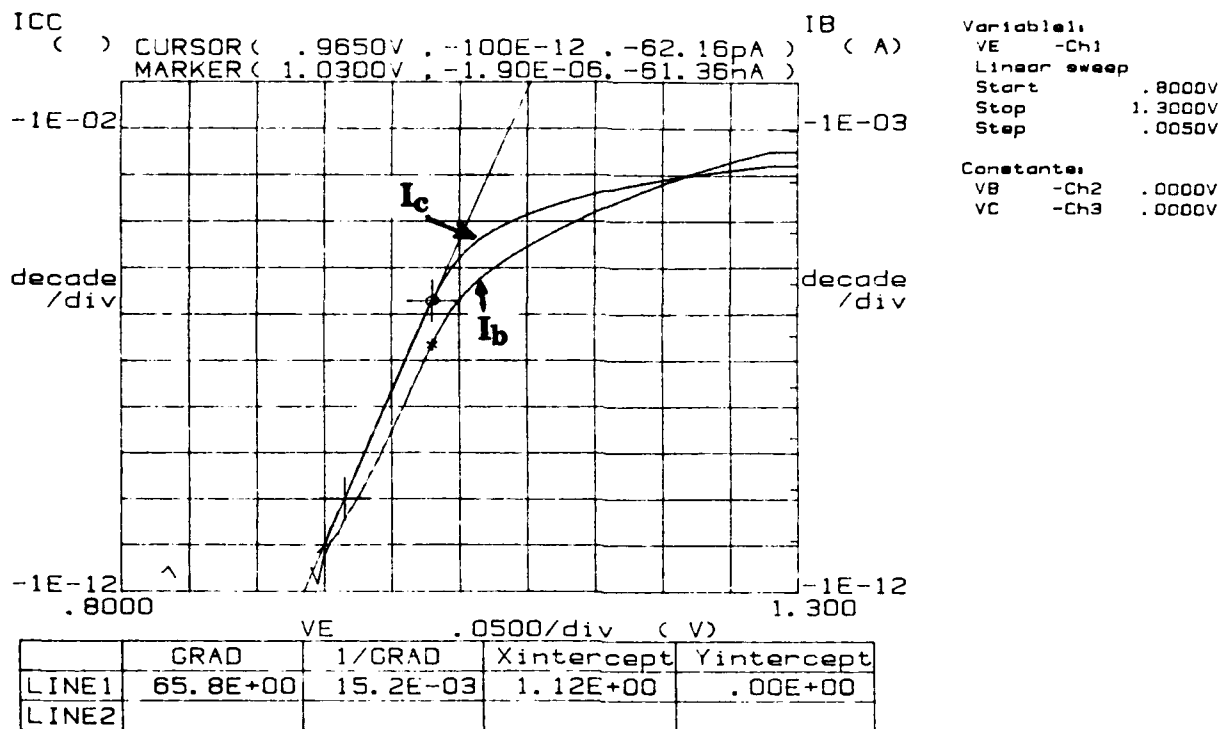
(a)
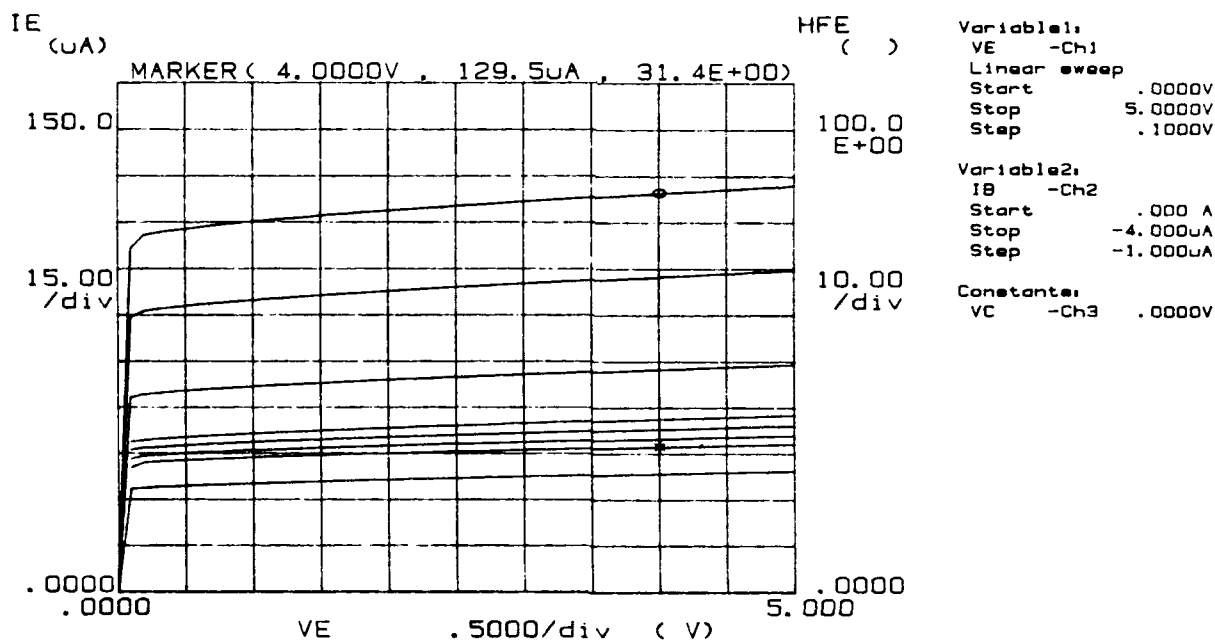
(b)

Figure 4.12: (a) Gummel plot and (b) transistor I-V curves at 77 K for a PNP transistor with the type D layout (small contact-sinker stripe) from wafer #24, after completion of the YBCO deposition and all microbolometer processing, including the rapid thermal anneal. The current gain for V_{ec} = 4.0 volts and I_b = 4 μA is 31.4.

Table 4.5
Low temperature (77 K) current gains for the three types of PNP transistors measured on wafer #24, after completion of the YBCO deposition and all microbolometer processing, including the rapid thermal anneal. The current gain was measured at V_{ec} = 4 volts, I_b = 4μA.

Transistor Layout Type	Current Gain (h_{fe})
A (small contact-emitter stripe)	26.6
B (large contact-emitter stripe)	16.8
D (small contact-sinker stripe)	31.4

the transistor turns on, with $V_{ec} = 4.0$ volts. These are operating voltages that could be used in a large imaging array of superconducting microbolometers.

4.6 Discussion

The results reported above demonstrate that bipolar PNP transistors at low temperature (77 K) can have current gains high enough to meet the requirements for a large imaging array of superconducting microbolometers, even after completion of the YBCO film deposition at ~700°C and all microbolometer processing. The leakage current of these transistors at 77 K is negligible.

For a large imaging array, it is desirable to use NPN, as well as PNP, bipolar transistors in the addressing and readout electronics that is monolithic with the array. The performance of NPN bipolar transistors at low temperature was not measured on this contract. It is also important that the PNP switching transistors at each pixel contribute very little noise compared to the microbolometer noise. The noise in the PNP transistors was not measured on this contract. Future work should include low temperature measurements of NPN transistors and of noise in the PNP transistors. However, it is not anticipated that these areas will present serious obstacles to the development of a large imaging array using bipolar transistors.

5.0 Study of Electrical Noise at the Transition Edge of High-T$_c$ Superconducting Films (E. Nowak, N. Israeloff, and A. M. Goldman, University of Minnesota)

5.1 Introduction

Research on high-T$_c$ (HTSC) materials is driven by applications which include microwave devices, infrared detectors, and magnetic sensors based on superconducting quantum interference devices (SQUIDs). There has been a corresponding impact on science which is focused on understanding a possible unusual mechanism, and unusual magnetic properties which embrace new magnetic paradigms such as vortex lattice melting and the vortex glass. The focus of research on these new materials is on characterizing their electrical and magnetic properties, and relating them to structural and chemical features. This report describes excess voltage noise measurements which have been carried out as a dynamical probe of electromagnetic properties. The technological implications of the work are important as intrinsic electrical noise will govern the sensitivity of all devices, including bolometers. The scientific problem of understanding vortex dynamics through noise measurements may elucidate the physical understanding of the onset of resistance in high temperature superconductors, an issue of technological signficance in other contexts.

There is a long history to the study of electrical noise in metallic[1] and semiconducting[2] thin films. In metals, noise is frequently attributed to mobility fluctuations which result from the motion of defects or impurities. In semiconductors where the carrier density is lower, it may be a consequence of a fluctuating number of charge carriers as well as mobility fluctuations. The noise spectral density, S$_v$, due to the resistance fluctuations can be represented by the expression given by Hooge[3] which is of the form

$$S_v(f) \propto \frac{\gamma V_{dc}^2}{N_c f^\alpha}$$

Here f is the frequency, V$_{dc}$ is the dc bias voltage across the sample, γ is a parameter called the Hooge parameter, and N$_c$ is the number of carriers. Since the parameter N$_c$ is a volume density, the spectral density depends inversely on sample volume.

Usually noise spectral densities vary as $f^{-\alpha}$, where $0.8 < \alpha < 1.2$ for a large variety of physical systems. When a system has a linear current-voltage characteristic and the magnitude of the noise depends on V$_{dc}^2$, then resistance fluctuations are not current generated. However, a transport current is necessary to monitor them. It was formerly thought that the Hooge parameter was a universal parameter as experiments on both metals and semiconductors showed $\gamma \approx 2 \times 10^{-3}$. Although there is considerable understanding of resistance fluctuations, detailed knowledge of their microscopic origin is largely unavailable. The Hooge formula is only a phenomenolgical formula used to characterize data.

64

The widely varying results of electrical noise studies of high temperature superconducting (HTSC) thin film[4,5] and bulk[6] samples are probably attributable to variations in specimen quality. The noise can be described by the Hooge formula if γ is allowed to be weakly temperature dependent ($\gamma \propto T^2$). In HTSC films the value of γ is usually 10^3 to 10^7 times larger than that of metals. Excess noise is also enhanced in the transition region. This can manifest itself as a peak in the noise spectral density at temperatures near the midpoint of the resistive transition. However, in the films discussed in this manuscript, the noise peak is usually found in the tail of the transition. The conventional explanation for a peak at the midpoint of the transition is that it is a consequence of thermal fluctuations which are coupled to the resistance through the large value of the parameter $\beta = dR/dT$. This is the model of Voss and Clarke.[7] A noise peak in the tail of the transition can not be explained by the thermal fluctuation model, and is essentially without explanation.

The work carried out under this contract was concerned with the study of low frequency voltage fluctuations in thin films of $DyBa_2Cu_3O_{7-x}$ (DBCO) and $YBa_2Cu_3O_{7-x}$ (YBCO). The work was directed at characterizing the noise which might be an impediment to the development of HTSC microbolometer infrared detectors. The major finding is that the excess noise can indeed be represented by the Hooge expression with the value of the temperature-dependent γ (at the midpoint of the resistive transition) ranging from 50 for films grown on a yttria-stabilized zirconia (YSZ) buffer layer on amorphous Si_3N_4 to at most 10 for films grown on single - crystal $SrTiO_3$.

An extensive study of the magnetic field dependence of the noise was also carried out and the results appear to have direct bearing on the nature of the vortex dynamics in the mixed state. Two distinct noise mechanisms have been observed. Analysis of the frequency dependence and voltage time traces in moderate fields (H < 5 kG) imply vortex motion is responsible for the random telegraph signal noise (RTSN) observed and the non-Arrhenius temperature dependence to the RTSN kinetics. At larger magnetic fields, RTSN is suppressed and for the most part the noise is featureless in frequency space. It typically has a power law dependence and no Lorentzian components. Whether this second, featureless noise component is related to models of the vortex glass transition of disordered superconductors has not been established.

5.2   Experimental Techniques

5.2.1 Films

Two types of films were investigated. Films of DBCO were prepared at the University of Minnesota using ozone-assisted molecular beam epitaxy (MBE).[8] This involved the co-evaporation of Dy, Cu, and Ba onto (100) $SrTiO_3$ or (100) $LaAlO_3$ substrates. The substrate temperature was maintained at 730°C during deposition, after which the film was allowed to cool down to room temperature with the ozone flowing. The films produced this way required no post-deposition

65

anneal and displayed sharp superconducting transitions with an onset temperature of 91 K and a zero-resistance temperature of 89 K. X-ray diffraction patterns indicated that the films were c-axis oriented (~90%). Scanning electron microscope (SEM) and transmission electron microscope (TEM) studies indicated that the films were granular with mean grain sizes on the order of 500Å to 2000Å. There also appeared to be evidence of a-axis grain outgrowths from the surface. Direct Coupled Plasma Atomic Emission Spectroscopy was used to measure the chemical composition of thin films grown on quartz substrates placed adjacent to the $SrTiO_3$ substrates during the deposition. The results would seem to indicate that although the films exhibited excellent superconducting properties, they were somewhat off-stoichiometry. The chemical composition of a typical high quality film was $Dy_{1.0}Ba_{2.5}Cu_{5.3}O_x$, that is, Ba and Cu rich. Unless otherwise noted, subsequent references to films produced at the University of Minnesota on $SrTiO_3$ or $LaAlO_3$ substrates should be understood to mean c-axis oriented films grown on (100) $SrTiO_3$ and (100) $LaAlO_3$ substrates.

Films ranging from thicknesses of 600Å to 1000Å were deposited onto 1/4" square substrates. After deposition the films were patterned using conventional photolithography or a stainless steel shadow mask and Ar ion mill as shown in Figure 5.1a. The patterning process did not degrade the sharpness of either the superconducting transition or the transition temperature. After patterning and ultrasonically cleaning in a toluene and methanol bath, 700Å thick silver contact pads were evaporated onto portions of the pattern. Wire lead attachments to these contact pads were made using pressed indium dots. The resulting contact resistance was approximately 1 Ω per pad at the transition temperature.

Films of YBCO were grown at Honeywell, as described in section 2.0 of this report. These were deposited using an ion beam sputtering technique in which the elemental constituents were mounted as Y_2O_3, BaO_2, and Cu targets on a rotating lazy-Susan. By controlling the dwell time of the beam on each target, a stoichiometric superconducting thin film was grown. The technique for oxygen loading involved the use of an ozone/oxygen mixture. The development of superconducting transition edge bolometers integrated into silicon - based integrated circuit technology has required the use of a Si_3N_4 layer on the silicon wafers, and a buffer layer of YSZ over the Si_3N_4. Typically, a 2000 Å thick YBCO film was deposited onto a 600 Å thick YSZ buffer layer, which was earlier deposited onto a 3000 Å thick Si_3N_4 layer. The latter was formed on a 3 inch diameter Si wafer. During the course of patterning and processing, the silicon below the microbolometer pixel was anisotropically etched in order to lower its thermal conductance to the silicon substrate. This enhanced thermal isolation allows for better responsivity of the bolometer. The HTSC thin films were close to stoichiometry, and were composed of highly c-axis oriented grains.

After a uniform film was deposited onto a 3 inch wafer, conventional photolithography and ion milling were used to pattern the film into many microbolometer pixels to form an array. After patterning and additional processing, a film of Ag 700 Å thick was evaporated onto a pixel's patterned contact pads and pressed indium dots were used to make wire lead attachments.
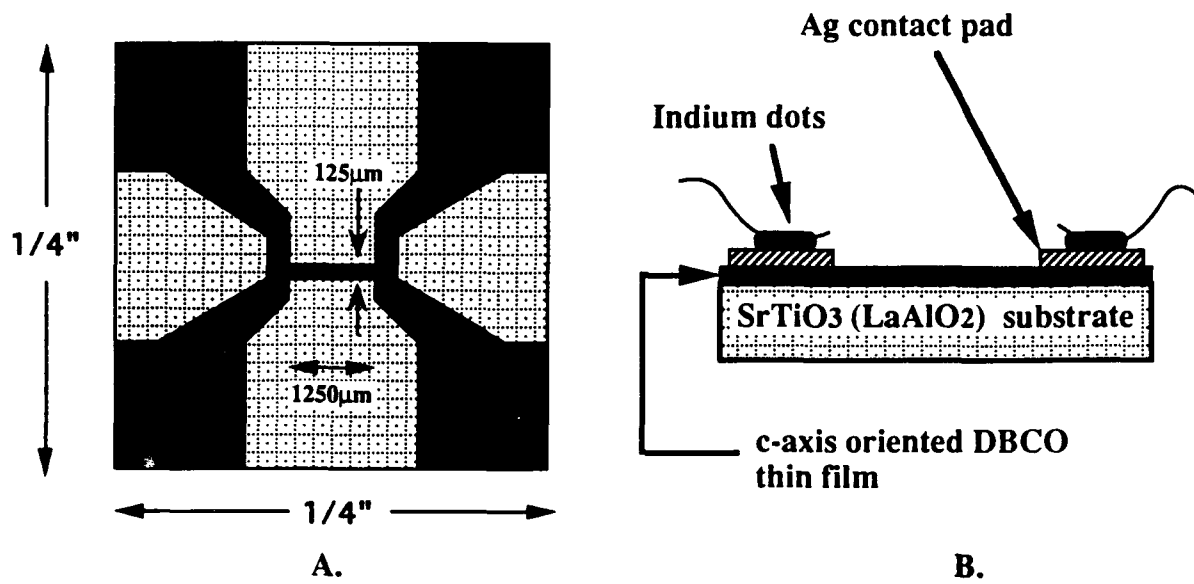
Figure 5.1: (A) The thin film pattern used for noise measurements at the University of Minnesota. (B) Crossection of DBCO thin film on SrTiO$_3$, showing the electrical connections.

Due to difficulties in matching the impedance of the thin film samples with the low noise preamplifier, extensive noise studies of films grown at the University of Minnesota were carried out on films that were patterned in the form of a single narrow line (125 μm x 1250 μm or 5 μm x 200 μm) onto which silver electrodes were evaporated. Noise in thermally isolated structures was not characterized at the University.

5.2.2 Measurement Techniques and Apparatus

The patterned samples were mounted on a Cu block using Apiezon N grease. The latter was attached to the end of a cryostat using nylon rods which provided a weak thermal link to the reservoir containing the cryogen . The block was positioned inside an evacuated Cu vacuum can. This apparatus is illustrated in Figures 5.2 and 5.3.

Two separate low temperature measuring sysems were constructed for these noise measurements. The first employed liquid nitrogen as a coolant and was equipped with a copper wire solenoid capable of reaching a maximum field of 250 Gauss. The latter was used to study the effect of an applied magnetic field on the noise. The system was shielded from stray fields using a double-walled mu-metal shield consisting of a high permeability inner wall and lower permeability (high saturation) outer wall. After finding anomalous field-dependent features in the noise, a liquid helium cooled apparatus equipped with a superconducting magnet capable of achieving fields of up to 6 Tesla was assembled.

The instrumentation consisted of a custom-built, ultra-low noise preamplifier, a programmable current source and a Hewlett Packard 3561A spectrum analyzer. A Quantum Design model 1802 temperature controller was used to set and control the sample temperature. After a dc current was passed through the sample, the voltage fluctuations were ac coupled into the preamplifier and passed to the spectrum analyzer for analysis. Figure 5.4 shows a schematic diagram of the instrumentation.

In the LN_2 cooled apparatus the long-term temperature stability was ± 4mK whereas in the LHe apparatus the stability was ± 10mK. Due to the digital operation of the temperature controller, it was necessary to condition the sensor excitation and heater output power lines through a filtering buffer circuit before passing the signals into the cryostat.

A programmable current source, which was also custom-built, allowed for switchable full scale current ranges from 2 microamps to 16 milliamps. Each current range was divided into 128 programmable currents. In all the noise measurements, the current noise was always less than 1.5 pA/√Hz. A carefully designed buffer amplifier was connected to the voltage lines and allowed the monitoring of the dc voltage across the sample at the same time noise measurements were being carried out, without injecting excess noise into the sample. A Keithley model 181 nanovoltmeter was used to measure the dc voltage.

COPPER ADAPTER attaches to bottom of 1K pot

Copper heat sink slugs for wiring

nylon posts for thermal isolation

nylon guide for electrical wiring feedthrough

COPPER SAMPLE BLOCK

threaded mounting holes for components and slugs

detachable bottom plate w/ thermometer clamp

YBaCuO sample

(a)

recessed platforms for hall probe and sample

Hall Probe

DyBaCuO sample

thermometer clamp

mounting holes to sample block

Platinum thermometer

Hall Probe

Copper heat sink slugs

Resistive heaters

heat sink slugs

Carbon glass thermometer

(b)

(c)

Figure 5.2: Structure for mounting samples in the liquid helium cooled cryostat. (a) Copper sample block, showing detachable bottom plate and attachments to the 1 K pot. (b) Side view of the sample block with bottom plate detached. (c) Side and top view of the sample block's bottom plate.
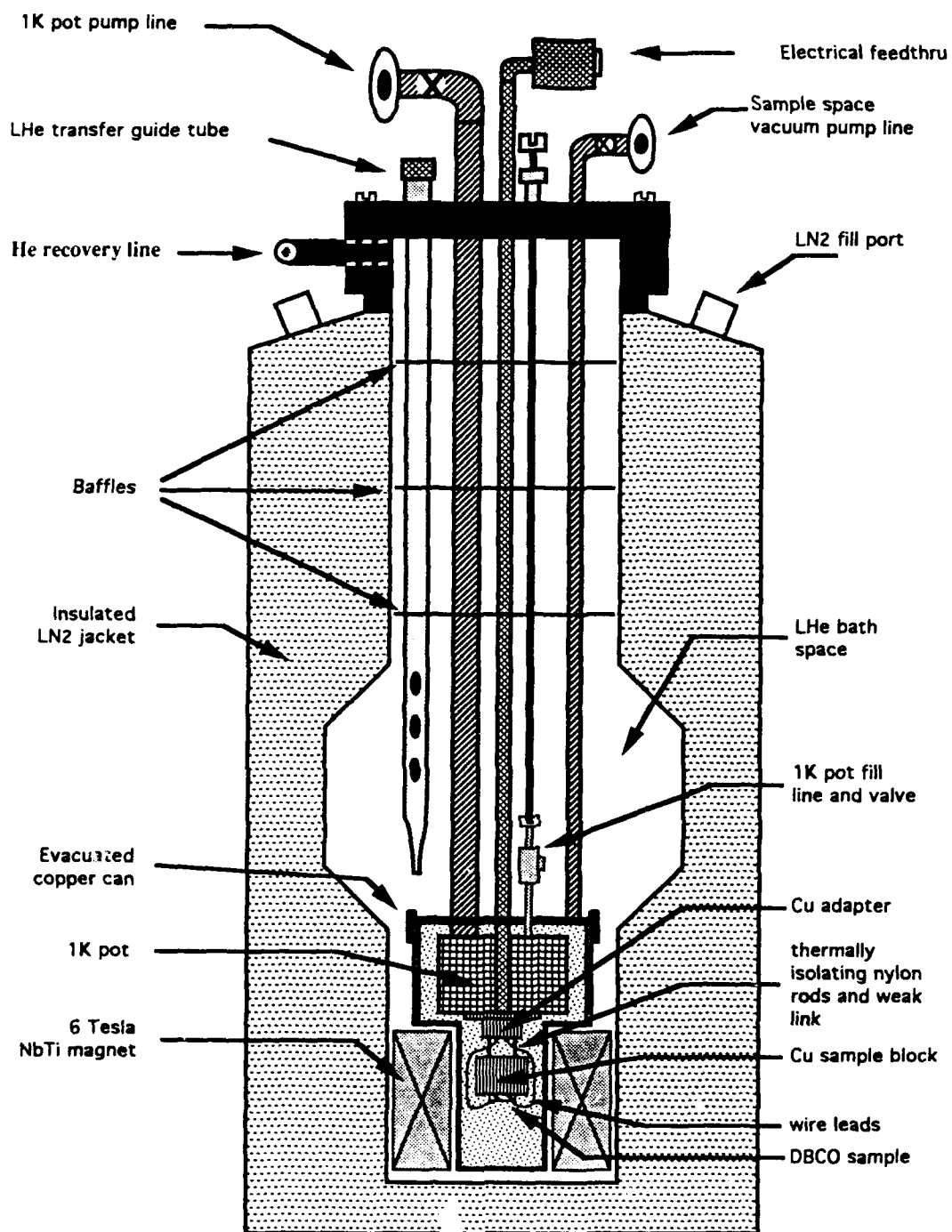
Figure 5.3: Liquid helium cryostat at the University of Minnesota for noise measurements on high-T_c superconductors in fields up to 6 Tesla.

Magnetically shielded electronics
Input voltage noise: 0.6nV/√Hz
Bandwidth: 1Hz to 100kHz

Sample, thermometer, and
heater mounted on copper block
weak-linked to liquid cryogen

Figure 5.4: Instrumentation used at the University of Minnesota for noise measurements on high-T_c superconductors.

The preamplifier employed eight matched bipolar transistor pairs (LM394 or MAT02) strung in parallel to achieve a 0.6 nV/√Hz noise level at the inputs. The measurement bandwidth was from 1 Hz to 100 kHz with a $1/f$ corner frequency of 4 Hz. The gain of the amplifier was fixed at 20,000. Dual inline package (DIP) switches for the input coupling 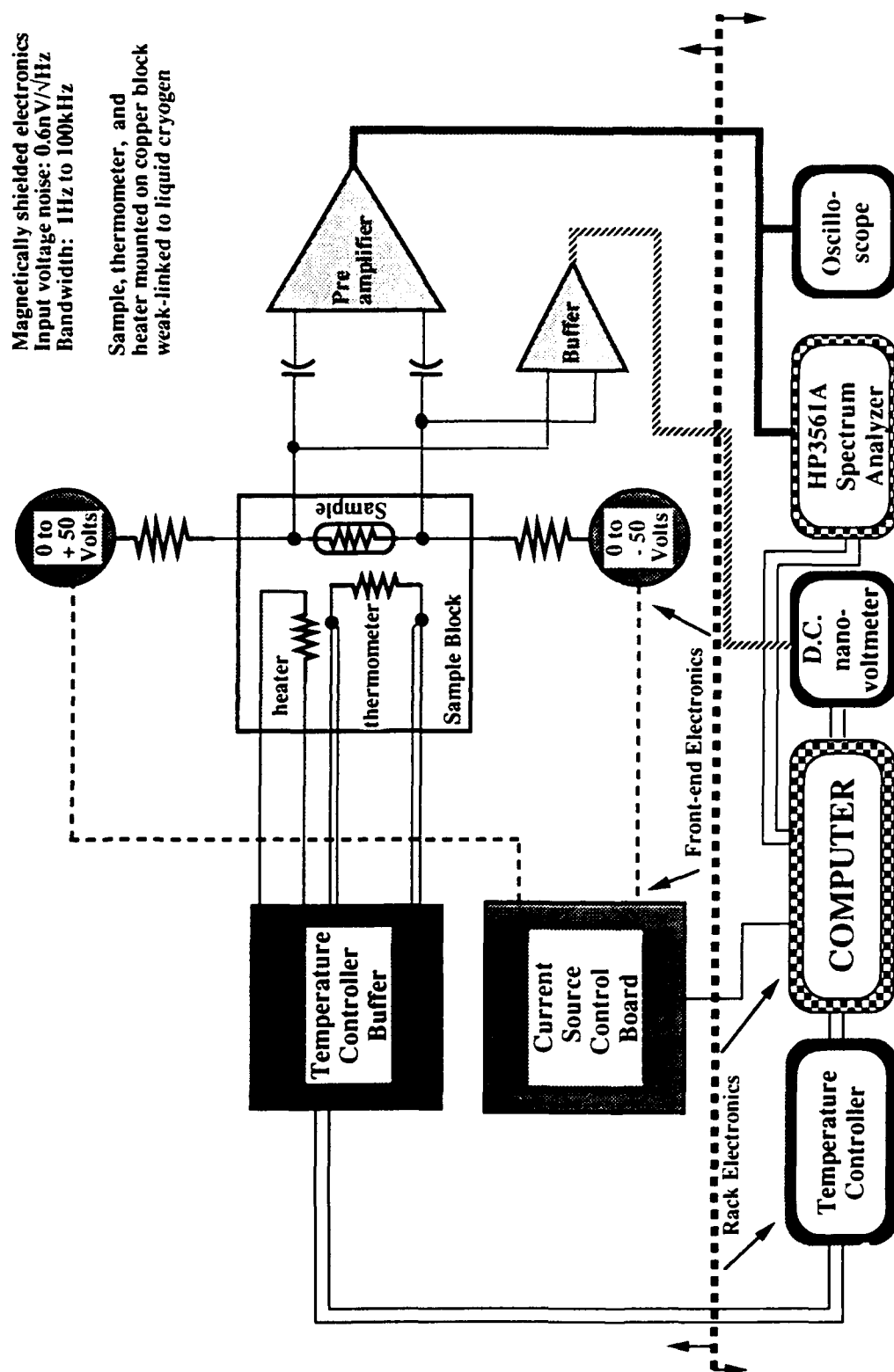capacitors, input impedance, and collector currents in the transistors permitted the optimization of the amplifier's performance over a wide range of sample impedances. The pre-amplifier, current source, and buffer board were packaged together, enclosed in a mu-metal shield and mounted as close to the electrical feedthrough of the cryostat as possible in order to minimize interference pickup. If a specific sample's excess noise was anticipated to be large, then a battery-powered current source and a Stanford Research model SR552 pre-amplifier were substituted for the custom-made electronics.

The output of the pre-amplifier was fed directly into the spectrum analyzer and could also be monitored using an oscilloscope. The analyzer averages the Fast Fourier Transforms (FFTs) of a series of time records and displays the root mean square (rms) voltage noise magnitude versus frequency. The spectra are then downloaded into a computer for analysis. The spectrum analyzer's bandwidth is from 125 µHz to 100 kHz.

The samples were studied using a conventional four probe configuration with a dc current supplied through two of the contacts. If a magnetic field was applied, it was always directed perpendicular to the substrate. This is parallel to the c-axis for a c-axis oriented film. To ensure that contacts were not contributing to the noise spectra the output impedance of the current source was kept at least 1000 times larger than the resistance across the current leads. Also, spectra were taken for at least two different output impedances, but with identical currents. Data were deemed to be satisfactory only if the differences in the results obtained in the two configurations were negligible. If the symmetry of the sample permitted, the current and voltage leads were interchanged as a further test for contact noise.

Unless otherwise noted, all noise spectra shown are excess noise spectra $S_v(f)$ with units of V^2/Hz. The excess noise was determined by measuring the background noise at zero bias current and subtracting it from the spectrum taken at a particular non-zero bias current. The background noise (with $I=0$) results from amplifier noise, the Johnson noise of the sample, and the electromagnetic pickup from the environment. When appropriate, the excess noise is normalized to V_{dc}^2 and to the sample volume to facilitate comparisons between different films. This normalized quantity is denoted as $S_n(f)$. It should be understood that the excess noise's inverse scaling with volume was not experimentally demonstrated for the films which will be discussed, but has been subsequently verified on similiar thin films which exhibited comparable noise characteristics.

5.3   Results

5.3.1   Films on Conventional Substrates

Low-frequency voltage noise measurements as a function of temperature, frequency, current, and magnetic field on DBCO and YBCO thin films have emphasized two important directions. First, an exhaustive effort was carried out to understand the "intrinsic" noise present in DBCO thin films grown on $LaAlO_3$, $SrTiO_3$, as well as vicinal $SrTiO_3$ substrates. The feature which was studied in detail was the peak in the excess spectral density at the foot of the resistive transition. The second direction was the study of patterned YBCO thin films grown on YSZ/SiN/Si substrates in a configuration suitable for bolometric applications.

Previous measurements of the noise voltage spectral density, S_v, have shown that a magnetic field applied parallel to the c-axis of DBCO thin films plays an important role in determining the magnitude and spectral dependence of the voltage noise peak. This is shown in Figure 5.5. Two noise regimes as a function of applied magnetic have been identified which we attribute to the details of the vortex kinetics. For low fields (H < 5 kG), the noise exhibits a broadened orentzian frequency dependence which is associated with a two-level fluctuator ⅼ the voltage vs. time trace. An example of this behavior is shown in Figures 5.6 and 5.7. The two-level fluctuator kinetics are non-Arrhenius in their temperature dependence, and are strongly dependent on current and field.

The magnitude of the two-level fluctuator can be characterized by the quantity $\delta R/R_{dc}$, where δR is the change in resistance induced by the two-level fluctuator, and R_{dc} is the average dc resistance. Values of $\delta R/R_{dc}$ as large as 10^{-3} have been observed in relatively large sample volumes of 10^{-8} cm^3. Flux vortex motion could explain such large changes in resistance only if $\sim 10^5$ vortices were moving cooperatively. This implies that electrical transport may be percolative in nature with the vortex motion modulating *inter*granular critical currents. In fact, the variation of S_v with magnetic field, measured at constant temperature, reveals what appears to be a noise fingerprint for the sample. That is, such a trace is very reproducible and ⅼhe peaks and valleys in the magnitude of S_v correspond to the presence or absence of distinct two-level fluctuators, which presumably are related to the details of the sample's defect, and thus vortex pinning structure. An example of this noise fingerprint is shown in Figure 5.8. The inset to Figure 5.8 shows the exponential decrease in noise as a function of magnetic field for fixed resistance in a different sample of somewhat larger volume. We are currently modeling this behavior within the context of a disordered Josephson junction array. In such an array it has been shown that the transition temperature (T_c) oscillations decay as a function of magnetic field[9]. Also, these T_c oscillations are found to decay to zero at a disorder dependent critical field. A similiar behavior to the noise is found in the case of the HTSC thin films. The analogy between the decay of T_c oscillations in the arrays and the decay of the noise in the HTSC films requires further investigation.
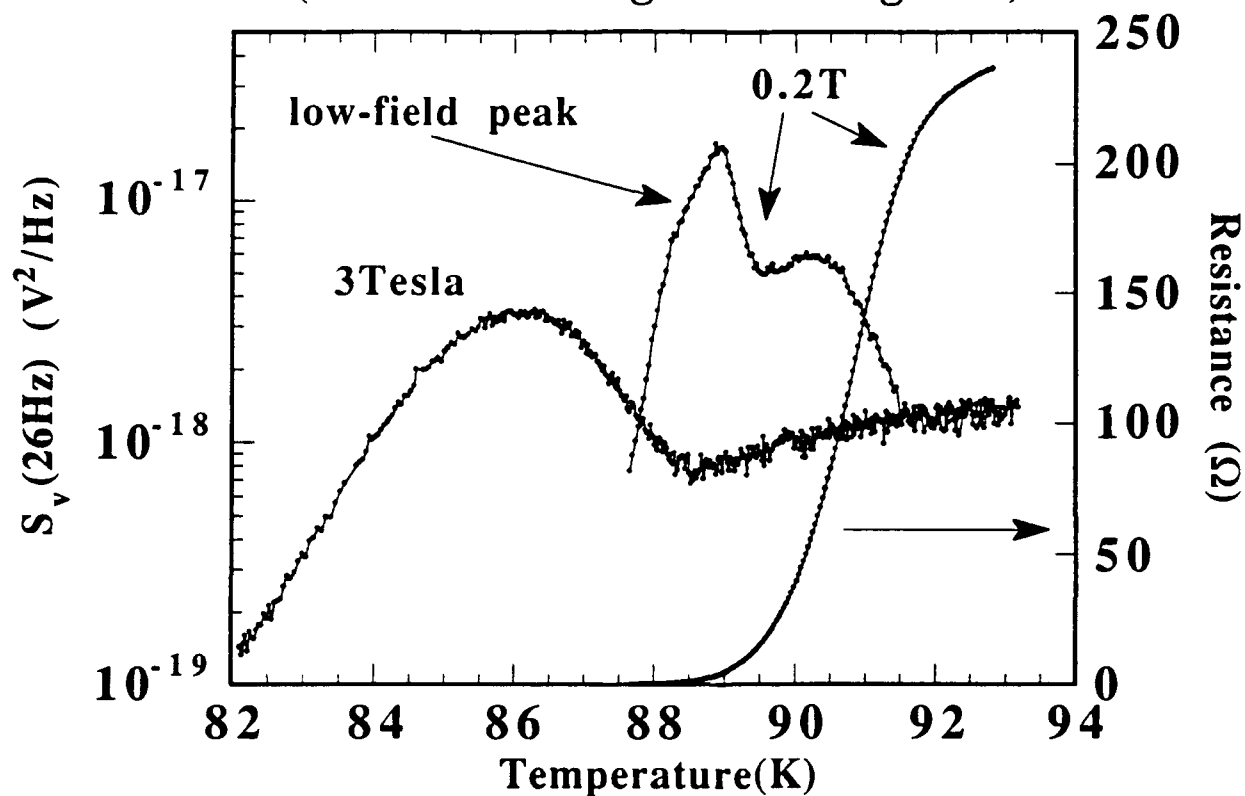
Figure 5.5: Noise power spectral density vs. temperature in low - field (0.2 Tesla) and high - field (3 Tesla) regimes, and the resistance vs. temperature in 0.2 Tesla magnetic field.
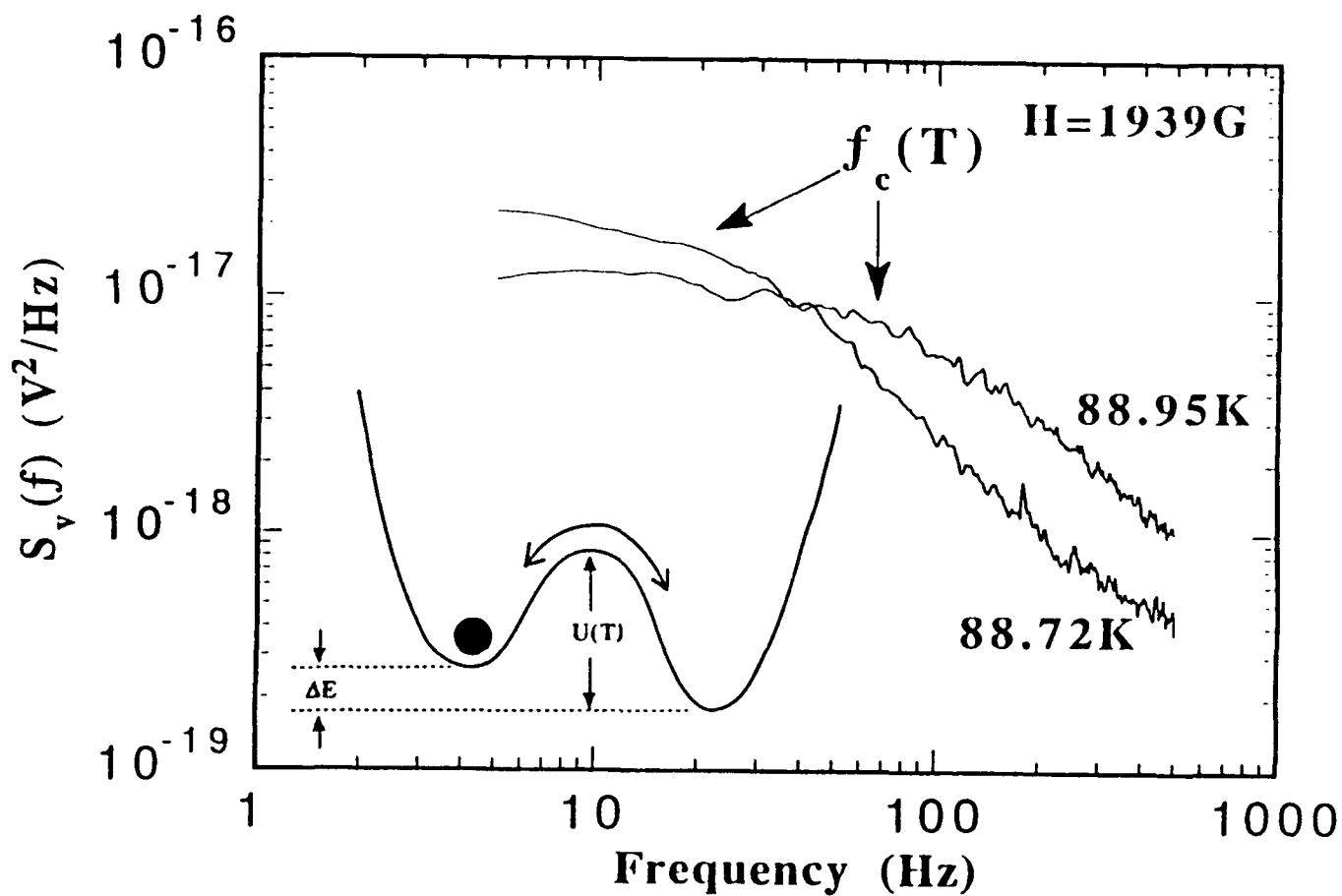
Figure 5.6: Broadened Lorentzian noise spectra in a magnetic field of 1939 Gauss at two different temperatures. Inset: Illustration of the possible origin of the Lorentzian spectra, showing hopping of a vortex in an asymmetric double well potential.
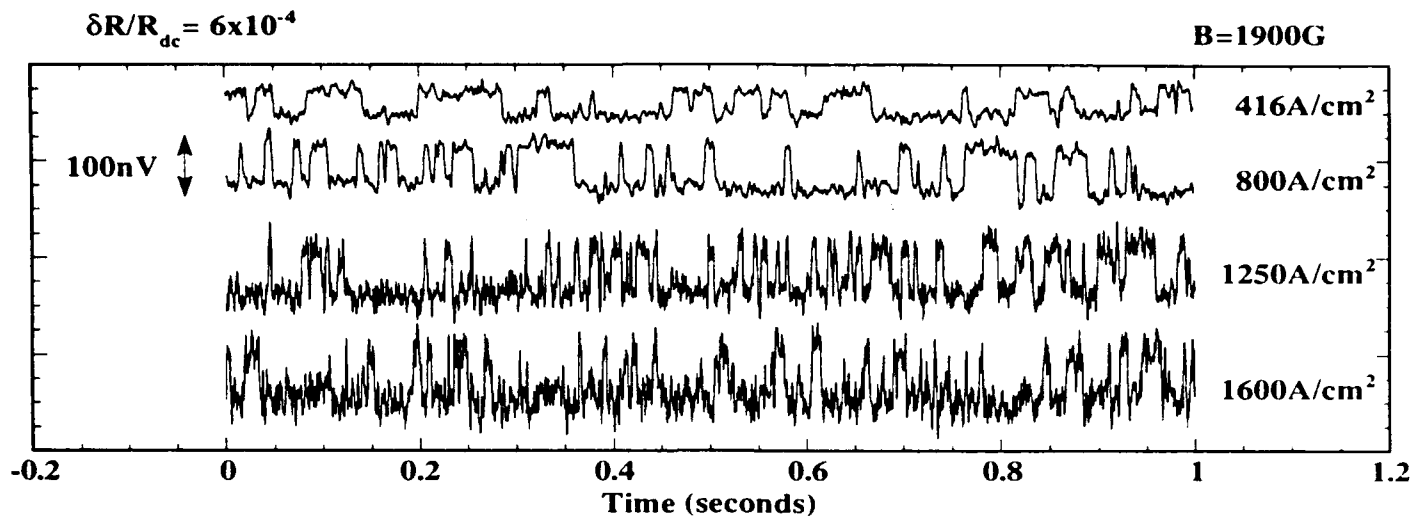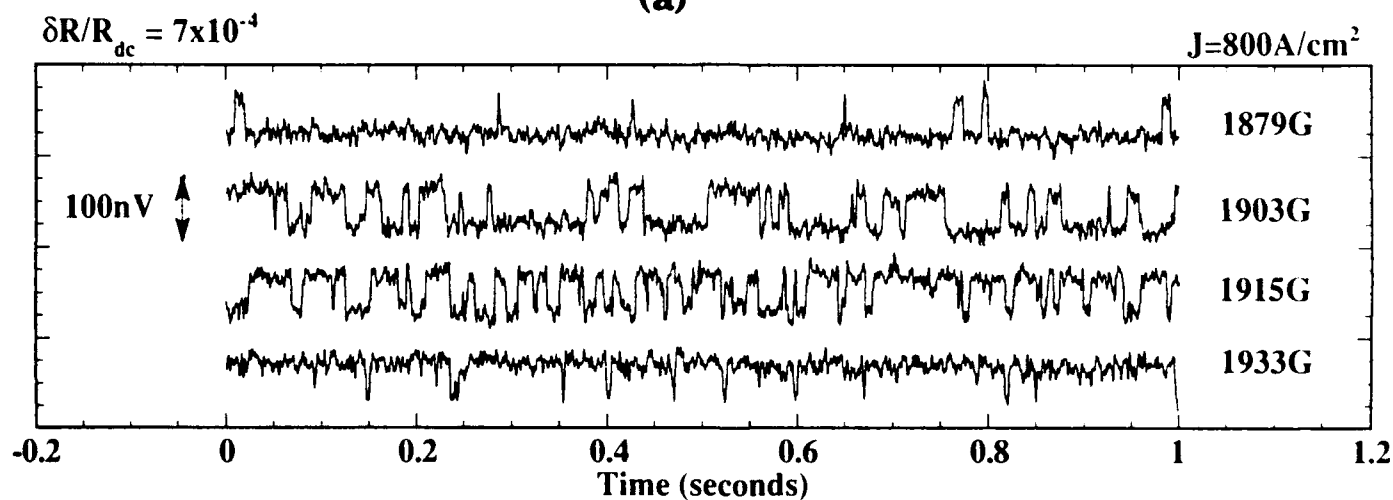
Figure 5.7: Random telegraph signal noise (RTSN). (a) The noise for several current densities. (b) The noise for several magnetic fields.
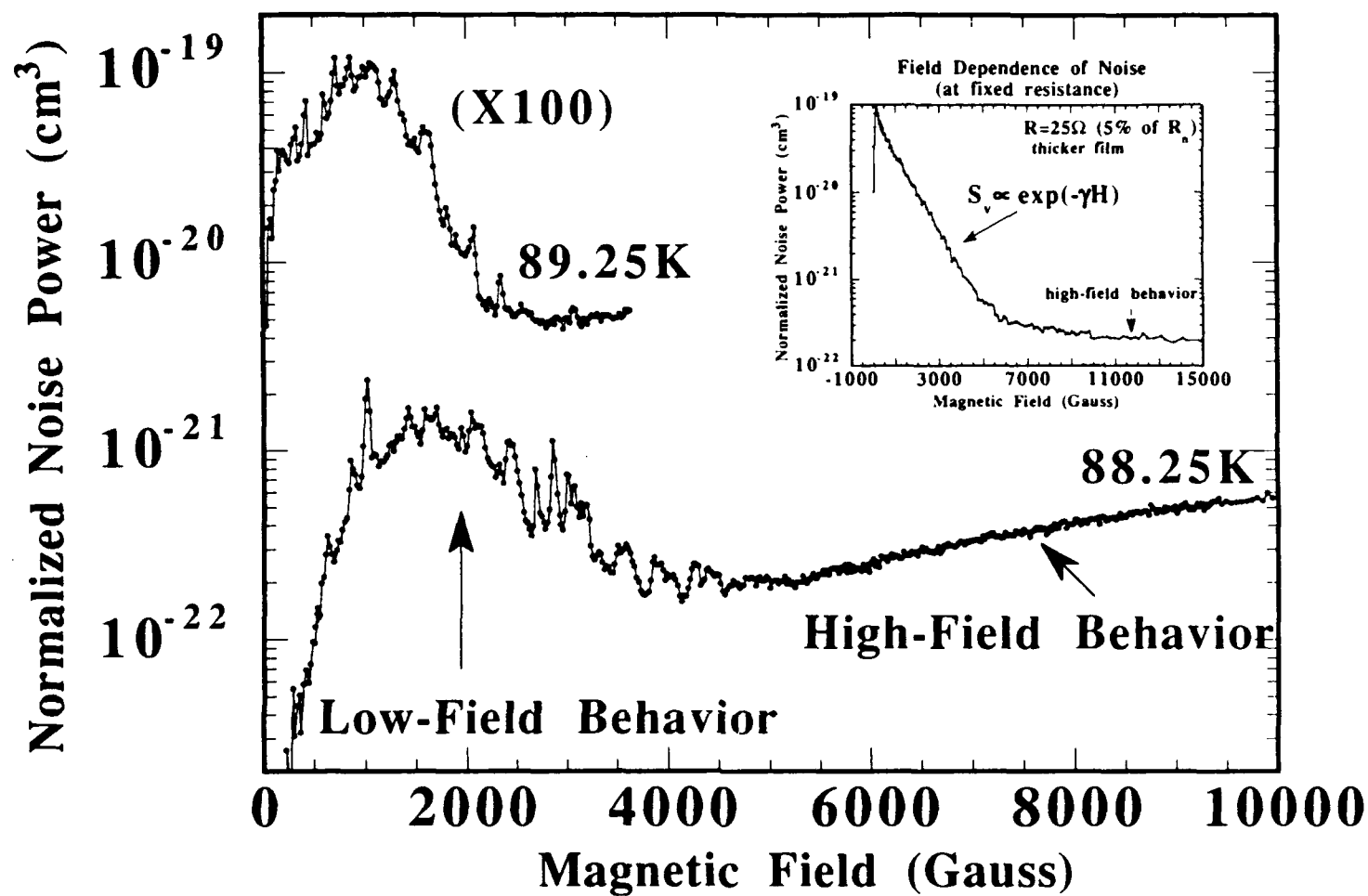
Figure 5.8: Normalized noise power as a function of magnetic field at two different temperatures. The structure in these traces is reproducible and unique to each sample, thus they have been called "noise magneto - fingerprints". Inset: Dependence of the noise on magnetic field, at fixed resistance.

Interestingly, for magnetic fields above 5 kG all evidence of two-level fluctuators and other properties associated with the low-field behavior is suppressed and S_v is found to scale as $I_{dc}^{1.2}f^{-0.75}$. In contrast to the low field behavior, the high field behavior of the noise is quite regular and systematic, as is shown in Figure 5.9. It is also found that for a given resistance, at least in the tail of the superconducting transition, S_v is independent of magnetic field. An example of these data is shown in Figure 5.10. The origin of this effect is puzzling. In the context of the vortex-glass model[10], we have attempted to relate this noise behavior to that of the critical fluctuations of the vortex excitations. We have determined the glass transition temperature, T_g, by an analysis of the current-voltage (I-V) characteristics of a film in a magnetic field[11] as shown in Figure 5.11. The glass temperature is taken to be that temperature at which the I-V curves exhibit $V \propto I^3$ power law behavior. The noise spectral density is then found to behave as $S_v \propto |T-T_g|^{-6.8}$, see Figure 5.12, which is what might be expected for noise in the vicinity of a glass transition. However, comparison with theory is not presently possible as no detailed predictions exist for noise near the glass transition. It is our view that the noise should be related to the dynamics of the vortices near the transition. We are also considering other possible physical origins of this noise such as the possibility that it is a simple consequence of vortex motion in a granular system.

5.3.2 Films on YSZ/Si₃N₄ Buffer Layers

Voltage noise power characterizations of a patterned YBCO thin film (18 μm x 600 μm x 0.2 μm) grown on a YSZ/Si$_3$N$_4$ double buffer layer obey the Hooge relation; that is, the noise power, as shown in Figure 5.13, is proportional to V_{dc}^2 with a frequency dependence of f^{-1} from T = 300 K to $T_c(R \approx 0$ Ohms). The noise measurements were made with current densities of 10^3-10^4 Amps/cm^2, typical of those necessary for operation of a microbolometer. The Hooge parameter, γ, which reflects the relative noise magnitude of the sample is found to decrease upon cooling from room temperature down to the onset of the resistive transition. However, within the transition region, γ is found to increase as the resistance decreases. Much of this increase is the result of the strong dependence of resistance on temperature and does not reflect the raw noise power which is weakly temperature dependent in the transition region. Values of γ range from approximately 125 at 300 K down to 2 at the onset of the resistive transition and 50 at the midpoint of the resistive transition. The temperature dependences of γ and resistance for a particular film are illustrated in Figure 5.14. These values indicate a considerable improvement over previous samples which exhibited values of γ on the order of 1000.

Noise measurements have demonstrated their usefulness as a gauge of film quality as well as an important probe for gaining a deeper understanding of the nature of electrical transport and the essential physics of the postulated vortex phases in high-T_c thin films. For bolometric applications involving the integration of high-T_c thin film sensors with silicon technology, the substrate plays a crucial role. Detailed X-ray studies of the in-plane orientation of the crystallites may reveal the microscopic details that determine noise properties
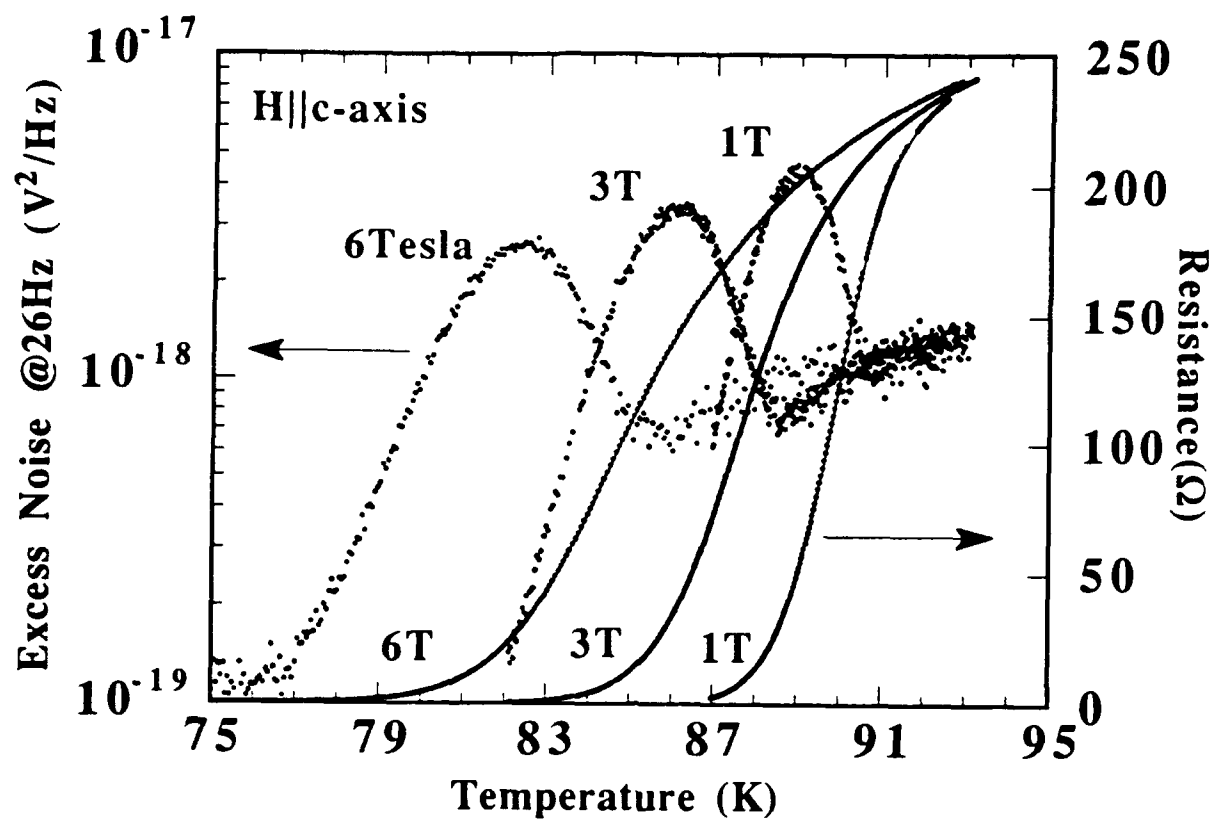
Figure 5.9: Dependence of the noise and resistance on temperature, for three values of magnetic field in the high - field regime.
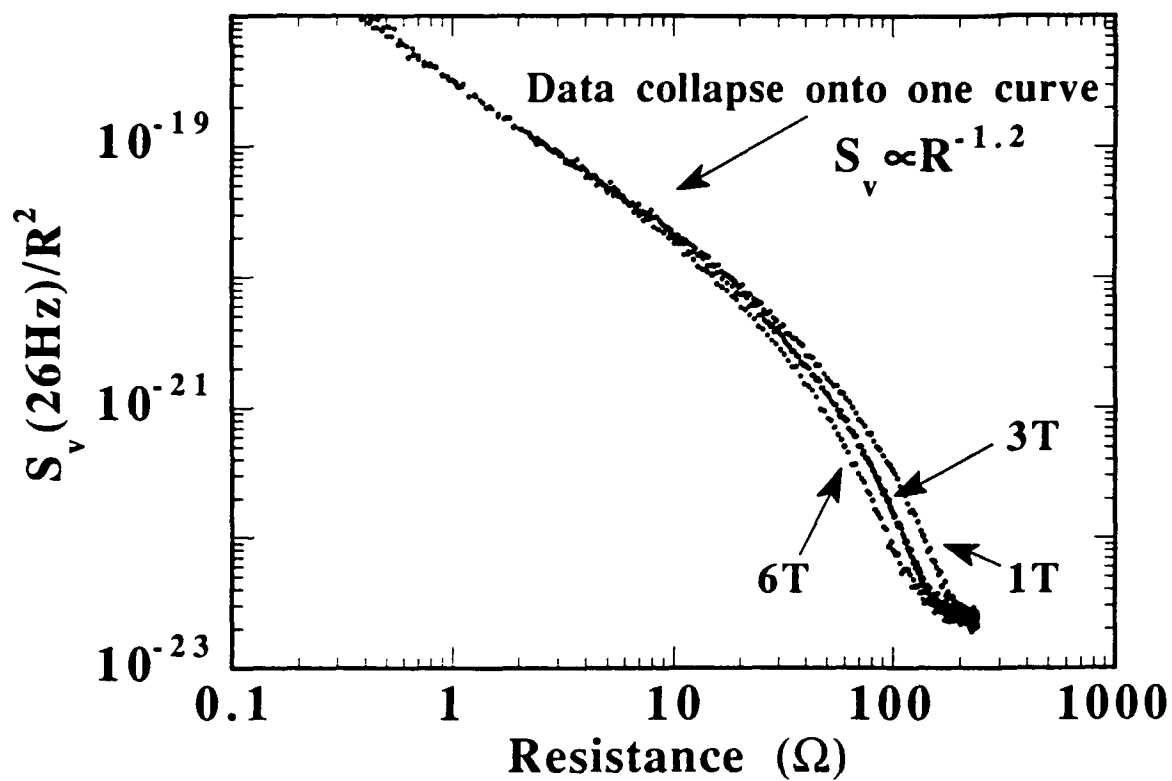
Figure 5.10: Noise (normalized by the square of the resistance) as a function of sample resistance, for three values of magnetic field in the high - field regime.
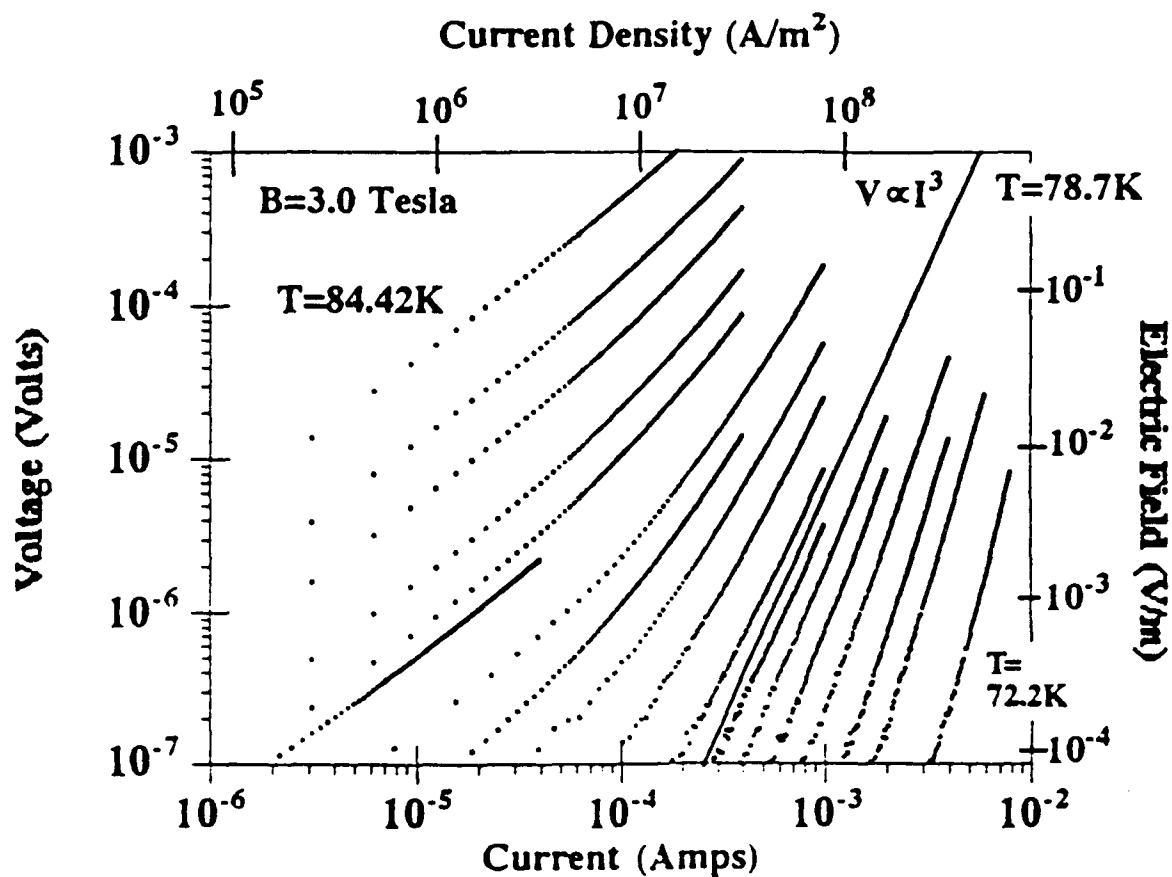
Figure 5.11: I - V curves for several temperatures, in a field of 3 Tesla, showing the change in the functional dependence of voltage on current with temperature. The vortex glass transition temperature, T_g, defined as the temperature at which the voltage is proportional to I^3, is 78.7 K.
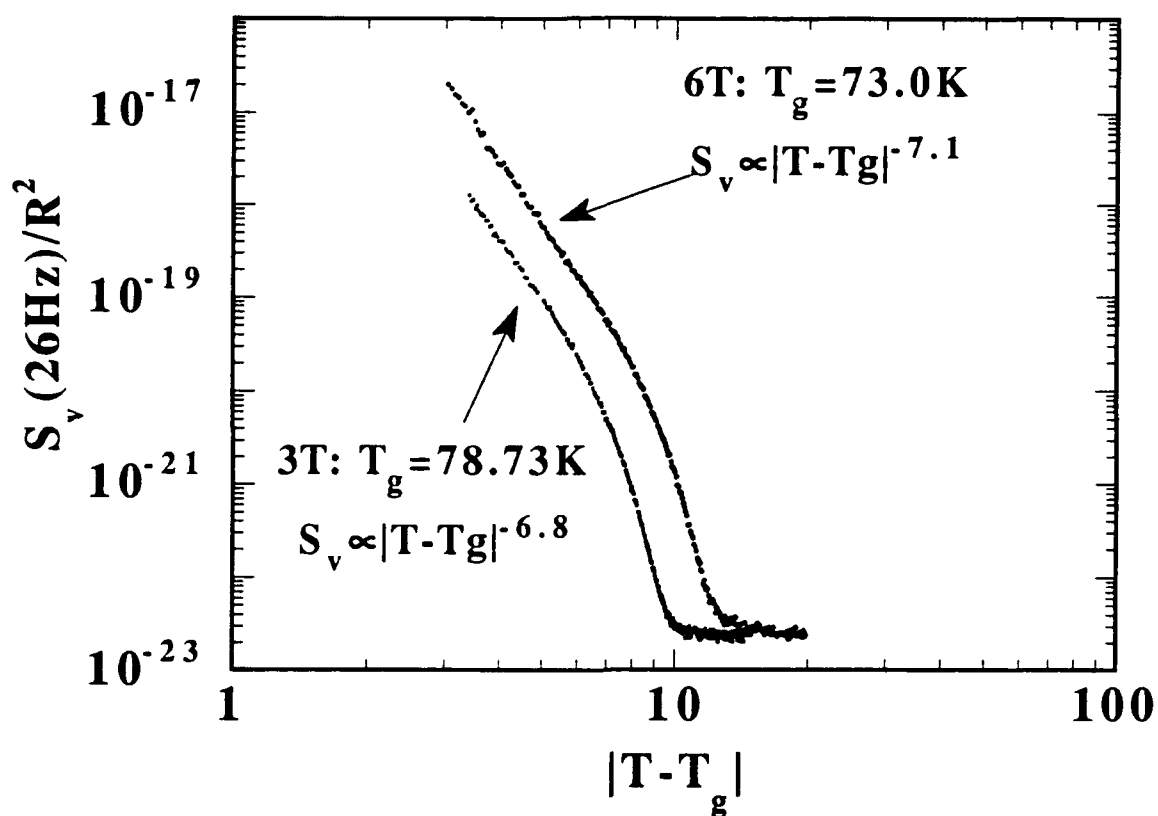
Figure 5.12: Normalized noise power spectral density as a function of $|T - T_g|$ for two values of magnetic field.
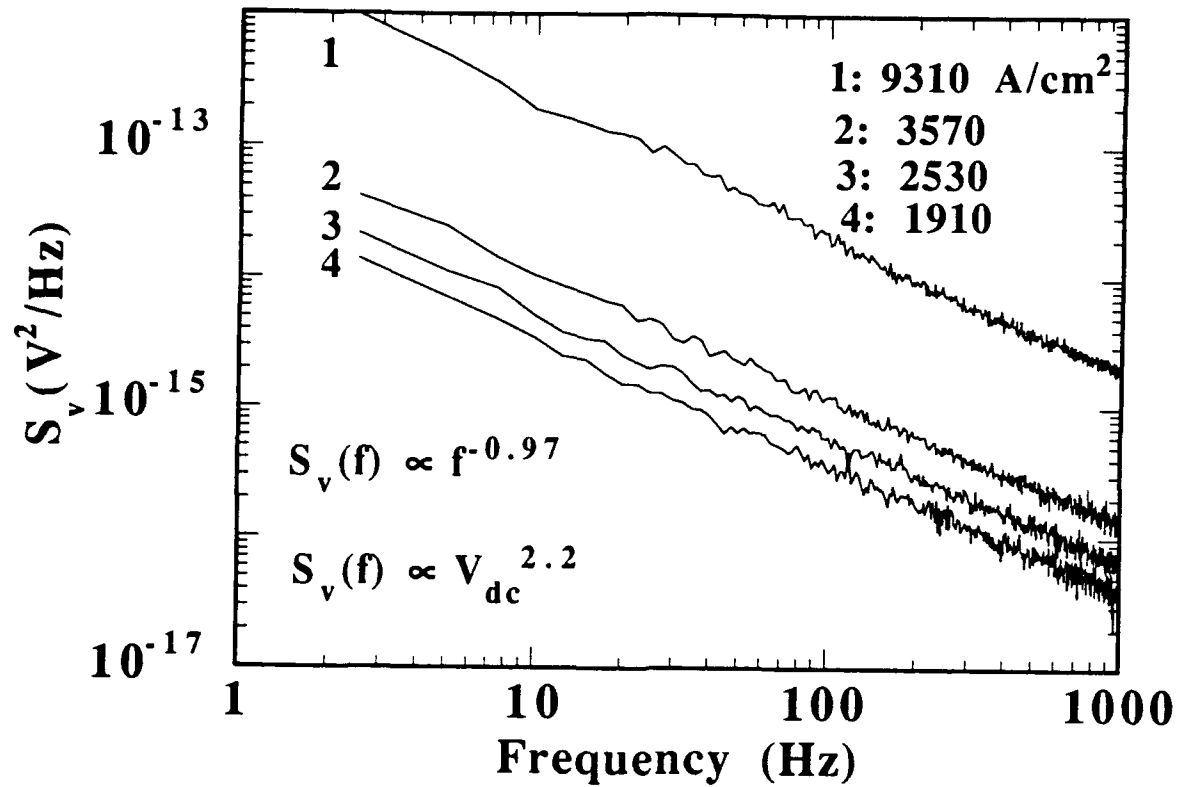
Figure 5.13: Noise spectrum for a YBCO film grown at Honeywell on a YSZ/Si₃N₄ buffer layer on silicon, at four different current densities, at the midpoint of the superconducting transition. The data are described accurately by the Hooge formula.
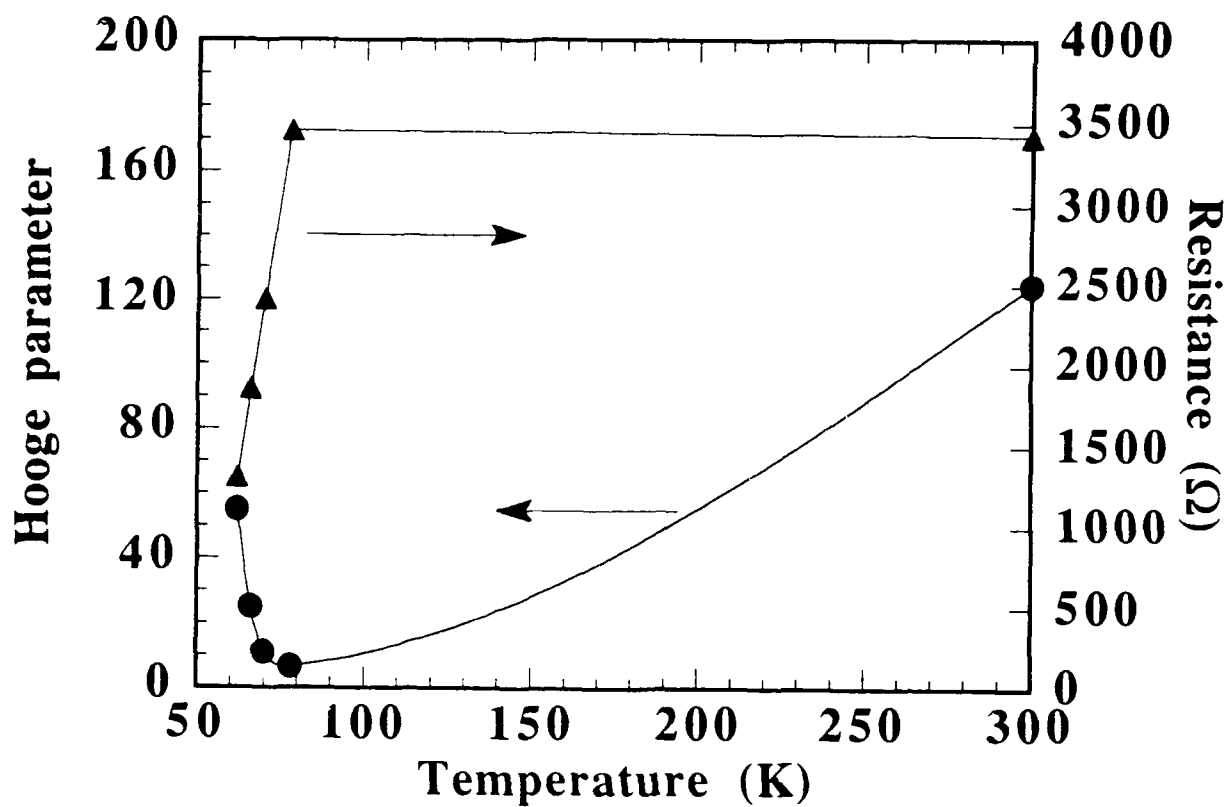
Figure 5.14: The Hooge parameter and resistance as functions of temperature for a YBCO film grown at Honeywell on a YSZ/Si_3N_4 buffer layer on silicon (sample HTS-133).

and overall bolometric performance. In Figure 5.15, a phi scan of one of the (308) peaks of a high quality DBCO film on $SrTiO_3$ shows that the full width half maximum (FWHM) of the in-plane misorientation is approximately 2.5 degrees. This spread corresponds exactly to the optical phi resolution that is available on the diffractometer in its present configuration and is an upper bound on the actual misorientation. Films grown by other groups[12] on YSZ buffer layers on silicon typically have displayed much broader phi scans along with the presence of 45 degree misoriented crystallites between the (308) peaks.

The studies of noise in YBCO films on YSZ/Si_3N_4 buffer layers on silicon clearly indicate that substantial progress has been achieved in growing quality films on these buffer layers and there is reason to believe that additional room for improvement exists.

Acknowledgements

References

1. P. Dutta and P.M. Horn, *Rev. Mod. Phys.* **53**, 497 (1981) and M. B. Weissman, *Rev. Mod. Phys.* **60**, 537 (1988).

2. A. L. McWhorter, in *Semiconductor Surface Physics*, 1957, edited by R. H. Kingston (University of Pennsylvania, Philadelphia), p. 207.

3. F. N. Hooge, *Phys. Lett. A* **29**, 139 (1969).

4. P. Rosenthal, *et al.*, *IEEE Trans. Mag.* **25**, 973 (1989); R. D. Black, *et al.*, *Appl. Phys. Lett.* **55**, 21 (1989); and J. H. Lee, *et al.*, *Phys. Rev. B* **40**, 10 (1989).

5. R. C. Lacoe, *et al.*, pre-print.

6. J. A. Testa, *et al.*, *Phys. Rev. B* **38**, 4 (1988).

7. R. F. Voss and J. Clarke, *Phys. Rev. B* **13**, 556 (1976).

8. D. D. Berkeley, *et al.*, *Appl. Phys. Lett.* **53**, 1973 (1988); B. R. Johnson, *et al.*, *Appl. Phys. Lett.* **56**, 1911 (1990).

9. S.P. Benz, M. G. Forrestor, M. Tinkham, and C. J. Lobb, *Phys. Rev. B* **38**, 2869 (1988).

10. M. P. A. Fisher, *Phys. Rev. Lett.* **62**, 1415 (1989).
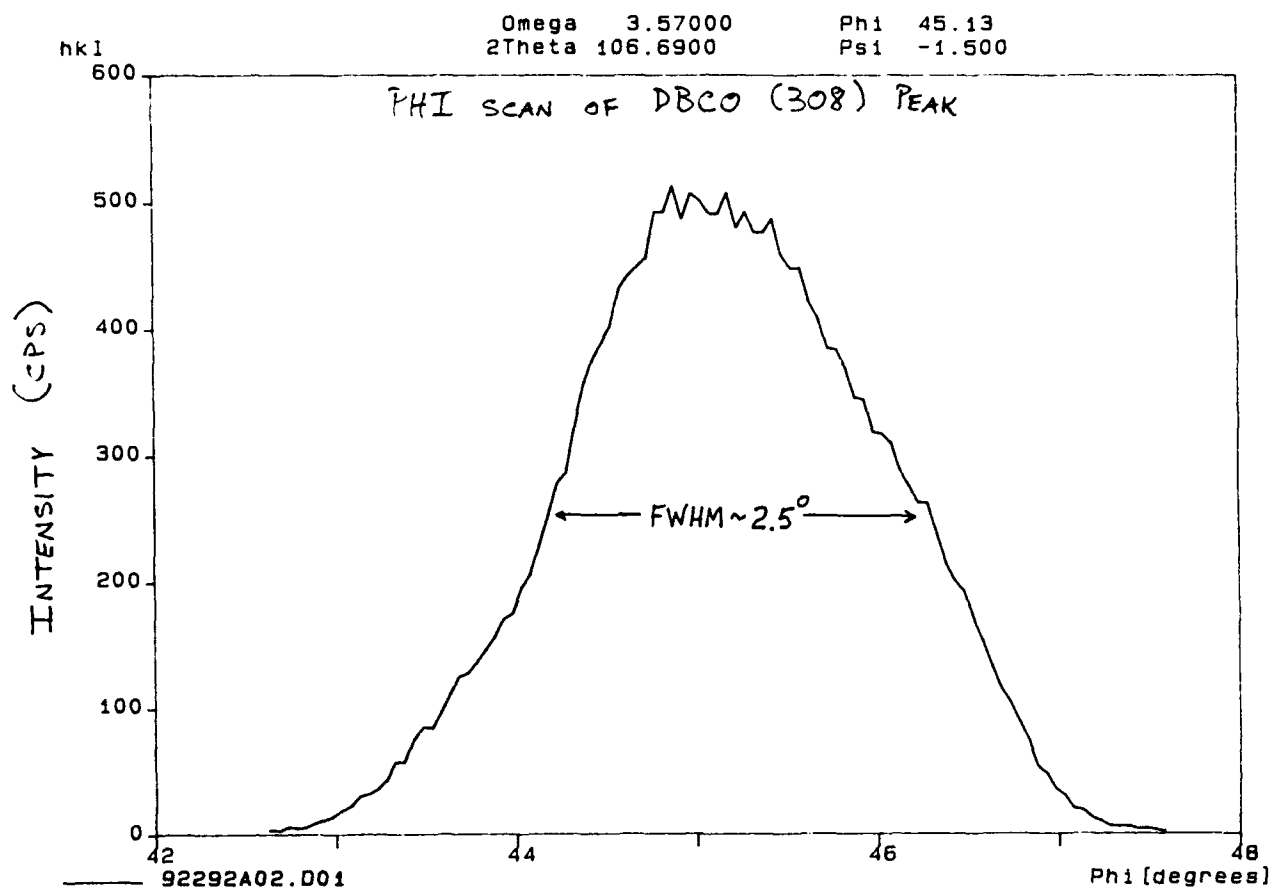
Figure 5.15: X-ray phi scan of the (308) peak of a DBCO film grown at the University of Minnesota on a single-crystal SrTiO3 substrate. The width of the peak is the instrumental resolution.

11. R. H. Koch, *et al.*, *Phys. Rev. Lett.* **63**, 1511 (1989).

12. D. K. Fork, *et al.*, *Physica C* **162-164**, 121 (1989).

APPENDICES

A.   List of Publications

B.   Reprints

C.   Theory of High T_c Transition Edge Superconducting Microbolometers

Appendix A
List of Publications

Papers Published in Refereed Journals

None

Papers Published in Conference Proceedings

B.R. Johnson, T. Ohnstein, H. Marsh, S.B. Dunham and P.W. Kruse, "YBa$_2$Cu$_3$O$_7$ Superconducting Microbolometer Linear Arrays," to be published in SPIE Conference Proceedings volume 1685, Infrared Detectors and Focal Plane Arrays.

B.R. Johnson, C-J Han, R.E. Higashi, P.W. Kruse and R.A. Wood, "Monolithic Silicon Focal Planes with High-T$_c$ Superconductor IR Sensors," to be published in the Proceedings of the IRIS Specialty Group Meeting on Infrared Detectors, NASA Ames, August 18-21, 1992.

B.R. Johnson, T.R. Ohnstein, C-J Han, R.E. Higashi, P.W. Kruse, R.A. Wood, H. Marsh and S.B. Dunham, "High-T$_c$ Superconductor Microbolometer Arrays Fabricated by Silicon Micromachining," presented at the Applied Superconductivity Conference, Chicago, IL, August 24-28, 1992. To be published in IEEE Transactions on Applied Superconductivity, Spring 1993.

Presentations

a. Invited

   B.R. Johnson, "Superconducting Microbolometer Infrared Detector Arrays on Silicon Microstructures," presented at the International Superconductor Applications Convention, San Diego, CA, January 14-16, 1991.

   P. W. Kruse, "Focal Plane Arrays Based Upon Thermal Detection Mechanisms," JASON Imaging Infrared Detector Workshop, LaJolla, CA, June 29, 1992.

   Paul W. Kruse, "Focal Plane Arrays Based Upon Thermal Detection Mechanisms," Defense Sciences Research Council Workshop on Multispectral Infrared Systems, LaJolla, CA, July 14, 1992.

   B.R. Johnson, T.R. Ohnstein, C-J Han, R.E. Higashi, P.W. Kruse, R.A. Wood, H.A. Marsh, and S.B. Dunham, "High T$_c$ Superconducting Microbolometer Arrays Fabricated by Silicon

Micromachining," Applied Superconductivity Conference, Chicago, IL, August 24-28, 1992.

b.   Contributed

B.R. Johnson, C-J Han, T.R. Ohnstein, B.E. Cole and P.W. Kruse, "Monolithic Integration of Semiconductor and Superconductor Components," DARPA Second Annual High Temperature Superconductors Workshop, Sheraton Tara Hotel and Resort, Danvers, MA, October 3-5, 1990.

B.R. Johnson, T.R. Ohnstein, P.W. Kruse and S.B. Dunham, "$YBa_2Cu_3O_7$ Films for Infrared Bolometers on Silicon Microstructures," DARPA Third Annual High Temperature Superconductors Workshop, Hyatt Bellevue Hotel, Bellevue, Washington, September 30 - October 2, 1991.

B.R. Johnson, P.W. Kruse, and S.B. Dunham, "$YBa_2Cu_3O_7$ Films For Infrared Bolometers on Silicon Microstructures," Materials Research Society Fall Meeting, Boston, MA, December 2-6, 1991.

P.W. Kruse, "Fundamental Limits of Infrared Detectors and Arrays," JPL Innovative Long Wavelength Detector Workshop, Pasadena, CA, April 7-9, 1992.

B.R. Johnson, T.R. Ohnstein and P.W. Kruse, "High T_c Superconducting Microbolometer Linear Arrays," JPL Innovative Long Wavelength Detector Workshop, Pasadena, CA, April 7-9, 1992.

B.R. Johnson, P.W. Kruse, T.R. Ohnstein, C-J Han and R.E. Higashi, "High T_c Superconductor Infrared Bolometers on Silicon Microstructures," American Ceramic Society Meeting, Minneapolis, MN, April 13-17, 1992.

B.R. Johnson, T.R. Ohnstein, H.A. Marsh, S.B. Dunham and P.W. Kruse, "$YBa_2Cu_3O_7$ Superconducting Microbolometer Linear Arrays," SPIE OE/Aerospace Sensing Meeting, Orlando, FL, April 20-24, 1992.

B.R. Johnson, C-J Han, R.E. Higashi, P.W. Kruse and R.A. Wood, "Monolithic Silicon Focal Planes with High-T_c Superconductor IR Sensors," IRIS Specialty Group on Infrared Detectors Meeting, NASA Ames, Moffett Field, CA, August 18-21, 1992.

B.R. Johnson, P.W. Kruse, S.B. Dunham, H.A. Marsh, C.J. Han and R.E. Higashi, "$YBa_2Cu_3O_{7-x}$ Microbolometer Arrays Fabricated by Silicon Micromachining," to be presented at Materials Research Society Fall Meeting, Boston, MA, November 30-December 4, 1992.

Appendix B
Reprints

Attached are reprints of scientific papers resulting from contract N00014-90-C-0226.

YBa$_2$Cu$_3$O$_7$ superconducting microbolometer linear arrays[*]

B.R. Johnson, T. Ohnstein, H. Marsh, S.B. Dunham and P.W. Kruse

Honeywell Sensor and System Development Center
Bloomington, Minnesota 55420

ABSTRACT

Single pixels and linear arrays of microbolometers employing the high-T$_c$ superconductor YBa$_2$Cu$_3$O$_7$ have been fabricated by silicon micromachining techniques. The substrates are 3-in. diameter silicon wafers upon which buffer layers of Si$_3$N$_4$ and yttria-stablized zirconia (YSZ) have been deposited. The YBa$_2$Cu$_3$O$_7$ was deposited by ion beam sputtering upon the yttria-stablized zirconia (YSZ), then photolithographically patterned into serpentines 4 μm wide. Anisotropic etching in KOH removed the silicon underlying each pixel, thereby providing the necessary thermal isolation. When operated at 70°K with 1 μA dc bias, the D* is 7.5x10^8 cm Hz$^{1/2}$/Watt with a thermal response time of 24 msec.

1. INTRODUCTION

Following the discovery of high-T$_c$ superconductors, investigations began into their use in transition edge bolometers[1-8]. One of the most promising applications of such bolometers is in arrays for thermal imaging systems.[9-11] Such systems today employ linear arrays of cryogenic photon detectors such as Hg$_{0.8}$Cd$_{0.2}$Te. Known as FLIR's (Forward Looking InfraRed), these systems employ a moving mirror to scan the infrared image of a scene over a linear array of photon detectors. The output of the detectors is amplified, multiplexed, and displayed on a video screen at 30 frames per second.

In order to develop a thermal imaging system of similar performance based upon thermal detectors rather than photon, the following requirements must be met:

- The detectors must respond to the wavelength region of interest, usually 8-12 μm for terrestrial viewing;
- The detectors must be capable of being fabricated in linear arrays;
- The responsivity must be high;
- The electrical noise over the system bandwidth must be low;
- The response time must be no greater than about 30 msec.

The YBa$_2$Cu$_3$O$_7$ array development described below is directed toward meeting these requirements.

2. THEORY

The figure of merit which describes the performance of infrared imaging arrays is the NETD (Noise Equivalent Temperature Difference). It is the difference in temperature of two large objects in the scene being viewed, each having an emissivity of unity, which generates a signal-to-noise ratio difference of unity when imaged on an array. The NETD is expressed in degrees centigrade (deg C) and is given by

$$NETD = \frac{(4F^2 + 1)V_N}{A_D \tau_o R(T_s)(\Delta P / \Delta T_s)_{\lambda_1 - \lambda_2}} \quad ; \qquad (1)$$

where F is the numerical aperture of the lens used to image the scene upon the array, V$_N$ is the noise voltage within the system bandwidth, A$_D$ is the area of one pixel, τ_o is the transmittance of the lens, R(T$_s$) is the responsivity of a pixel to radiation from a black body at temperature T$_s$, and $(\Delta P/\Delta T_s)_{\lambda_1-\lambda_2}$ is the change in radiant power per unit area emitted by a black body at temperature T$_s$ with respect to a change in T$_s$ measured over the spectral interval between λ_1 and λ_2. The value of $(\Delta P/\Delta T_s)_{\lambda_1-\lambda_2}$ for 300°K ambient temperature over the 8 μm - 12 μm spectral interval is 2.62 x 10^{-4} W/deg K.

To obtain a low NETD, which is desirable, one needs small F/no., highly transparent optics, large pixel area, high pixel responsivity and low noise. The expression for the responsivity of a bolometer is

$$R(T_s) = \frac{I_b \alpha R_e \eta}{G(1 + \omega^2 \tau^2)^{1/2}} \quad .$$

(2)

Here I_b is the bias current, R_e is the pixel resistance, η is the optical absorptance of the pixel, G is the thermal conductance between the sensitive area of the pixel and the thermally heat sunk substrate, ω is the angular modulation frequency of the radiation falling on the pixel, α is the temperature coefficient of resistance (TCR) of the pixel, given by

$$\alpha = \frac{1}{R_e} \frac{dR_e}{dT} \quad ;$$

(3)

and τ is the thermal response time of the pixel, given by

$$\tau = \frac{C}{G}$$

(4)

where C is the heat capacity of the pixel.

A figure of merit describing the signal-to-noise ratio of a pixel is the detectivity $D^*(T_s)$, given by

$$D^* = \frac{R(T_s)(A_p B)^{1/2}}{V_N} \quad ;$$

(5)

where V_N is the electrical noise within the bandwidth B.

In order for the bolometer to have a high responsivity, so that the NETD will be low and the D^* will be high, it is necessary to have a high TCR and a highly thermally isolated pixel. A high TCR is the reason for operating at the transition edge of a superconductor. The TCR of $YBa_2Cu_3O_7$ near the superconducting transistion temperature is roughly 100 times higher than that of semiconductors and 1000 times higher than that of metals.

The requirement for excellent thermal isolation dictates the structure of the pixel. That used here consists of a Si_3N_4 membrane upon which is deposited YSZ, then $YBa_2Cu_3O_7$. Infrared radiation falling on the pixel causes a minute rise in temperature. The heat is conducted away through the Si_3N_4 to the surrounding Si. The thermal decay time τ, which is required to be no greater than about 30 msec to be TV frame rate compatible, thus gives rise to a need for a very small pixel heat capacity.

3. ARRAY FABRICATION

Fabrication of the single pixels and linear arrays begins with 3 in. diameter Si wafers which have been coated with a layer of Si_3N_4 3000 Å thick. The wafers are loaded into an ion beam sputtering system capable of depositing both YSZ and $YBa_2Cu_3O_7$. A rotating target assembly is employed to first deposit a layer of YSZ 600 Å thick, then a layer of $YBa_2Cu_3O_7$ 2000 Å thick at 735°C using ozone and oxygen. The $YBa_2Cu_3O_7$ is deposited by sputtering from 8 inch targets of Y_2O_3, BaO_2, and Cu in a timed sequence in order to control the film stoichiometry. The entire sequence is repeated once every 8 seconds.

A small amount of Ag is co-sputtered with the Cu in order to increase the critical current and reduce the noise in the $YBa_2Cu_3O_7$ films. The resulting films are c-axis oriented. A final layer of YSZ 300 Å thick is deposited on top of the $YBa_2Cu_3O_7$ to passivate the superconductor against damage in subsequent processing steps. The $YBa_2Cu_3O_7$ is then patterned into serpentines 4 μm wide by standard photolithography and ion milling. Silicon nitride 7500Å thick is then deposited to provide further passivation and to provide structural strength for the thermally isolated microstructures. The

$YBa_2Cu_3O_7$ on the electrical contact pads is exposed by plasma etching and ion milling, and gold is sputter deposited to make electrical contact to the superconductor. The final step is a KOH anisotropic etch which removes the Si underneath the Si_3N_4. Figure 1 is a photomicrograph of a microbolometer made in this manner. The thermally isolated area is approximately 85 μm x 115 μm with an average thickness of 1.2 μm. The overall pixel area is 125 μm x 125 μm.

4. PERFORMANCE

Figure 2 illustrates the resistance as a function of temperature for seven thermally isolated pixels and one thermally heat sunk pixel from one linear array. Six of the seven thermally isolated pixels have nearly identical resistance vs. temperature characteristics. It is not known why one of the thermally isolated pixels has an anomalous resistance. The thermally isolated pixels are heated by background radiation from the inner walls of the cryostat vacuum can, resulting in a lower apparent superconducting transition than the heat sunk pixel. The pixel resistance does not go to zero below the transition edge due to resistance at the $Au/YBa_2Cu_3O_7$ contacts.

Figure 3 illustrates the TCR of one thermally isolated pixel from the same array as a function of temperature. The peak value of about 0.34/deg K occurs at about 72°K. Although the TCR of $YBa_2C_3O_7$ films on lattice-matched substrates is nearly ten times higher, it is difficult to obtain steep transitions for films on polycrystalline YSZ over amorphous Si_3N_4. Furthermore, a very steep edge reduces the dynamic range of the system and makes temperature stabilization at the midpoint more difficult.

Figure 4 illustrates the responsivity as a function of temperature, comparing it to αR_s as a function of temperature. The radiation source was a 1000°K black body illuminating the sample through a 1 Hz chopper and a sapphire window. The maximum responsivity of 62,000 V/W measured at 16 μA bias is found at 70°K. There is significant self-heating of the pixel when a dc bias current of 16 μA is used. This enhances the peak height, makes the peak narrower, and shifts it to lower temperature relative to the peak in responsivity at low bias current. For example, the peak in responsivity with 1 μA dc bias is 1,300 V/W, at a temperature of 73°K.

Noise measurements on the pixels show a $1/f$ power law dependence from 50 Hz to 1000 Hz, for a dc bias current of 100 μA with a small amount of gas in the cryostat to enhance the thermal conductance and reduce the amount of self-heating of the pixel. The noise voltage is proportional to bias current, as expected for resistance fluctuations. Two-probe and four-probe noise measurements on test structures on the same wafer reveal most of the excess noise to be associated with the $Au/YBa_2Cu_3O_7$ contacts.

Frequency response measurements reveal a thermal response time (3db on rolloff) of 24 msec for small bias current (1 μA). With larger bias current, self-heating causes a longer time constant. The measured D^* for a 1 μA dc bias current at a frequency of 7 Hz (the 3db rolloff frequency) is 7.5×10^8 cm $Hz^{1/2}$/Watt. It should be mentioned that the noise bandwidth in a large thermal imaging array can be of order 100 kHz. Thus, the noise per unit bandwidth at 7 Hz where $1/f$ noise dominates, is much larger than the average noise per unit bandwidth of a typical thermal imager.

5. DISCUSSION

While not yet exhibiting performance equivalent to $Hg_{0.8}Cd_{0.2}Te$ arrays, these results are nevertheless very promising. Many areas of improvement are possible.

- The NETD is limited by $1/f$ power law noise from the contacts. Contacts with lower resistance (and presumably, lower noise) can be fabricated by in-situ deposition of Au on the $YBa_2Cu_3O_7$. This should reduce the total noise voltage by a factor of 10. Reductions in the $YBa_2Cu_3O_7$ noise are also possible.
- The optical absorption is low. By employing free space impedance matching absorbers (190 ohms/square) and anti-reflection coatings, the absorption can be raised by a factor of 2.
- Joulean heating limits the responsivity. Under low duty cycle pulsed bias the peak responsivity will increase by at least 10 times.

For a thermal imaging system with 125 μm pixels, 0.1 Hz to 100 KHz noise bandwidth, using 100 μA pulsed bias current, F/1.0 optics, imaging in the 8 μm to 12 μm wavelength band, the present pixels would give a NETD of 17 mK. If the above improvements are made, the NETD for an array of these 125 μm pixels could be reduced to 1 mK.

The performance of such an array would be fully competitive with not only $Hg_{0.8}Cd_{0.2}Te$ linear arrays but also $Hg_{0.8}Cd_{0.2}Te$ staring arrays. Fabricated by Si processing, the production cost should be much less than $Hg_{0.8}Cd_{0.2}Te$.

6. REFERENCES

1. P.L. Richards, et al., Appl. Phys. Lett. 54, 283 (1989).

2. P.L. Richards, et al., IEEE Trans. Magn. 23, 283 (1989).

3. L. Xizhi, et al., Int. J. Infrared and Millimeter Waves 10, 445 (1989).

4. J. C. Brasunas, et al., J. Appl. Phys. 66, 4551 (1989).

5. J.C. Brasunas, et al., SPIE Proceedings 1292, 155 (1990).

6. B. Dwir, et al. Supercond. Sci, Technol. 2, 314 (1989).

7. S. Verghese, et al., SPIE Proceedings 1292, 137 (1990).

8. S. Verghese, et al., IEEE Trans. Magn. 27. 307 (1991).

9.. T.G. Stratton, et al., Appl. Phys. Lett. 57, 99 (1990).

10. P.W. Kruse, SPIE Proceedings 1292, 108 (1990.

11. B.E. Cole, SPIE Proceedings 1394, 126 (1991).
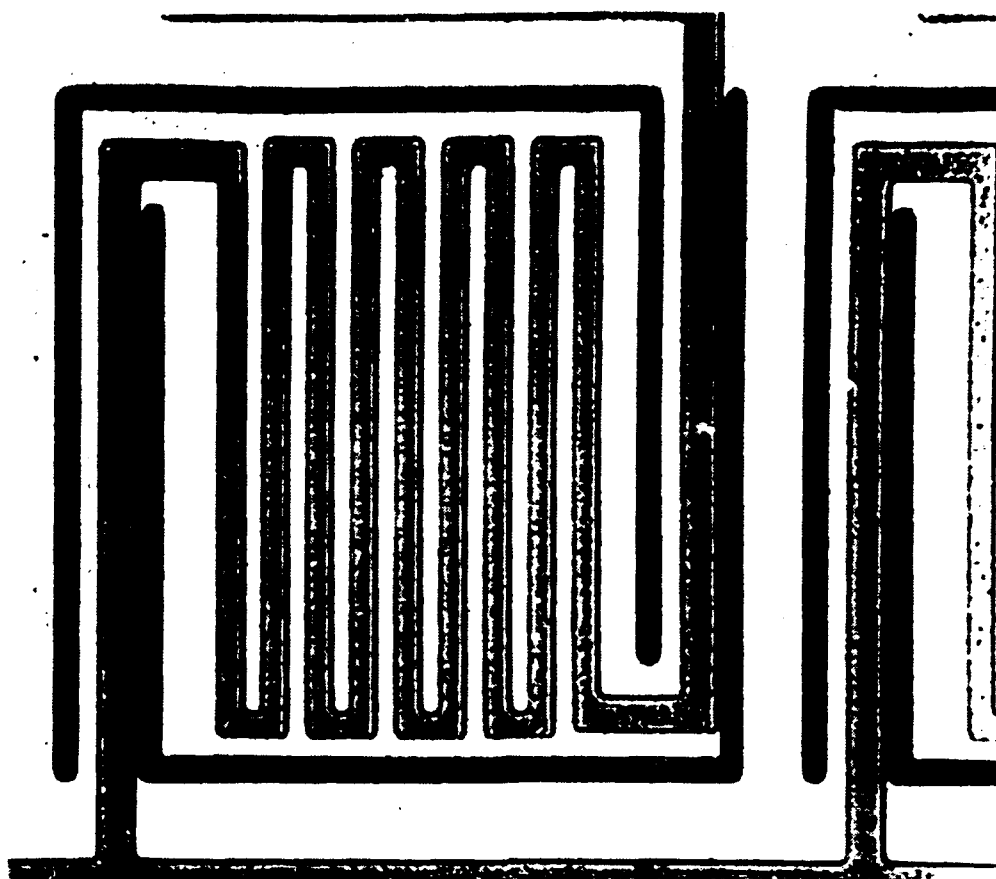
Figure 1. One Pixel of a YBaCuO Superconducting
Microbolometer Array
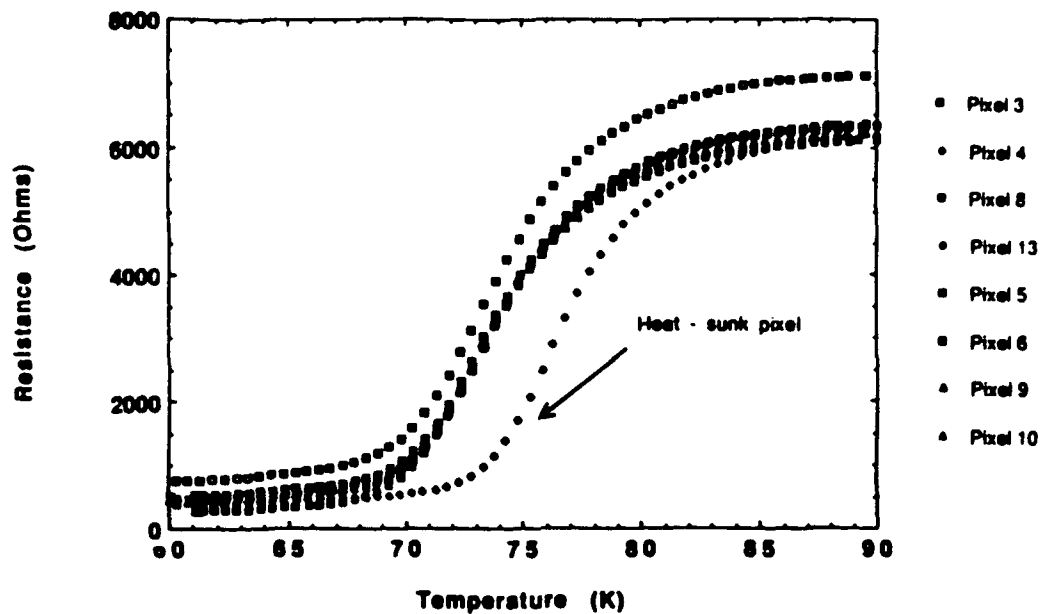
Figure 2. Resistance Vs. Temperature for Several Pixels

Figure 3. Resistance and TCR vs. Temperature

97

File B70316uArsp&dRdT.gra   3/17/92
Pixel #3, Die B7, wafer 2-15
16 μA Bias, Chopper 1.04 Hz
Note: At Responsivity peak, IR peak to peak
signal is 40% of bias voltage!

Figure 4. Responsivity and dR/dT vs. Temperature at 16 μA Bias

HIGH - Tc SUPERCONDUCTOR MICROBOLOMETER ARRAYS FABRICATED BY SILICON MICROMACHINING

B.R. Johnson, T. Ohnstein, C.J. Han, R. Higashi, P.W. Kruse,
R.A. Wood, H. Marsh, and S.B. Dunham
Honeywell Sensor and System Development Center
Bloomington, MN 55420

Abstract--Linear arrays of YBa$_2$Cu$_3$O$_7$ transition edge microbolometers have been fabricated on silicon substrates using silicon micromachining to produce microbolometer structures with good thermal isolation. These bolometers, measuring 100 μm x 100 μm x 1 μm, have a noise equivalent power of 1.3×10^{-12} Watts/Hz$^{1/2}$ (neglecting contact noise) and a thermal time constant of 24 msec. Thi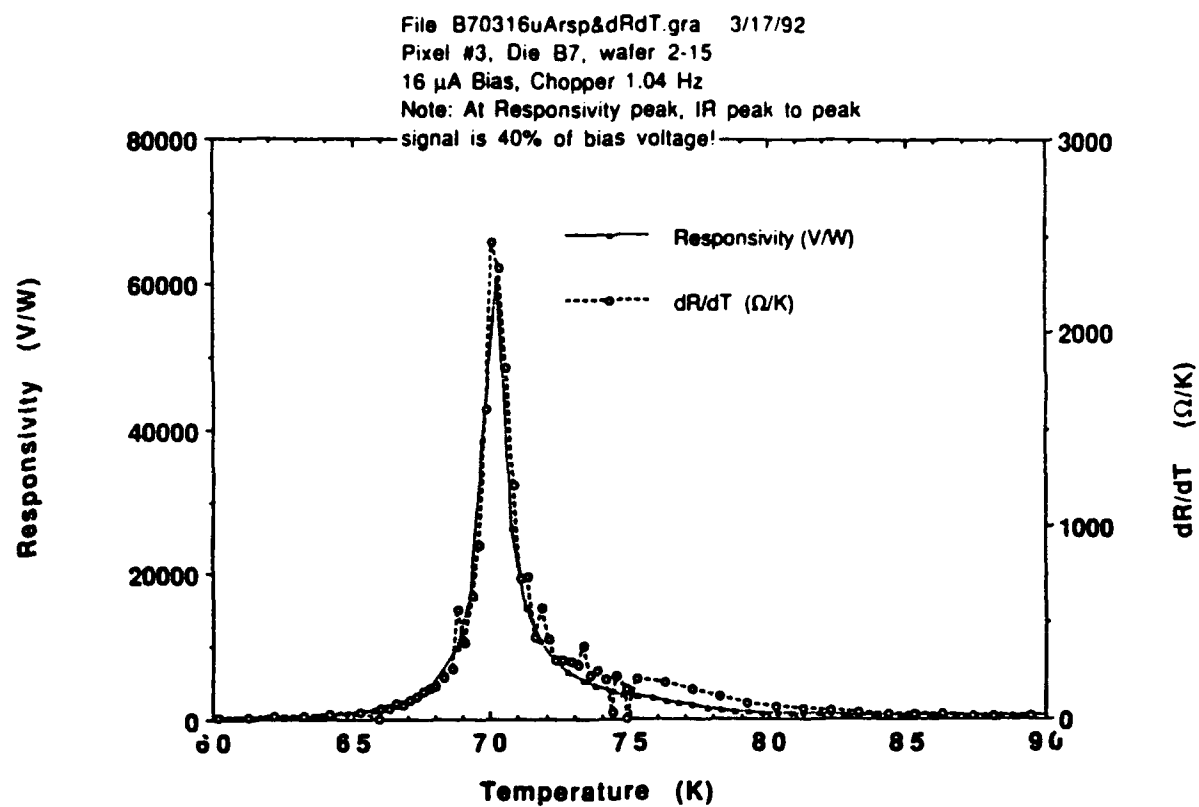s performance indicates that a 2D staring focal plane array of superconductor microbolometers could have a performance comparable to HgCdTe staring focal plane arrays without further improvements in the sharpness of the superconducting transition or reductions in the YBa$_2$Cu$_3$O$_7$ electrical noise. The use of silicon processing technology to fabricate the superconductor microbolometers results in a significant cost advantage over HgCdTe, and there is no long wavelength cutoff in the sensitivity of a superconductor microbolometer.

I. INTRODUCTION

The responsivity (see Eq. 1) of a microbolometer is inversely proportional to the thermal conductance between the thermally isolated region which is sensitive to the radiation and the heat sink to which it is attached. By using silicon micromachining techniques, structures with very low thermal conductances can be fabricated. By making these structures very small, fast thermal response can also be achieved. In addition, fabricating these structures on silicon allows integration with monolithic electronics, low substrate cost, and use of standard silicon processing techniques. These features have allowed fabrication of large staring two - dimensional focal plane arrays (FPA's) of micromachined microbolometers using a semiconductor resistive material at room temperature [1,2]. These FPA's have yielded high quality infrared imaging at a 30 Hz frame rate. The microbolometers in these arrays are addressed with monolithic transistor switches located at each pixel. It is expected that the sensitivity of these FPA's can be increased substantially by using a superconductor at its transition temperature as the temperature - sensitive resistor material on the microbolometer.

In this paper, we report progress toward fabrication of such a superconductor microbolometer FPA by fabricating linear arrays of YBa$_2$Cu$_3$O$_7$ (YBCO) microbolometers on silicon substrates. In an earlier paper, we reported fabrication of a single microbolometer by a process which was difficult to reproduce [3]. The high sensitivity of the microbolometers

reported here and their successful fabrication on large area silicon wafers by silicon micromachining techniques is a signifcant first step toward the fabrication of a superconductor microbolometer FPA for infrared imaging.

II. YBCO FILM GROWTH

The substrate and buffer layer materials for YBCO film growth were dictated by the silicon micromachining requirements. Silicon nitride was used as the primary structural material supporting the thermally isolated microstructures that formed the microbolometers. Silicon nitride also passivated the YBCO against etching by the hot KOH solution used to remove the silicon underneath the microbolometers. A 3000 Å thick layer of sputtered Si$_3$N$_4$ was the first film to be deposited onto the 3 - inch silicon wafers. A buffer layer of yttria - stabilized zirconia (YSZ) 600 Å thick was then deposited by ion beam sputtering, followed by a 2000 Å thick layer of ion beam sputtered YBCO.

The YBCO film stoichiometry was controlled by a rotating target assembly containing 8-inch targets of Cu, BaO$_2$ and Y$_2$O$_3$. Material was sputtered from the three targets in a precisely timed sequence by rotating the target assembly with a stepper motor controlled by a computer. The film was grown at 730°C while flowing 3 sccm of ozone and 8 sccm of oxygen to produce a combined ozone/oxygen pressure of 5×10^{-4} Torr. Although deposition of Y, Ba, and Cu was sequential, only 3 Å of material was deposited during each cycle through the three targets, so the cations in the film were well-mixed. A small piece of silver foil was placed on the copper target in an attempt to enhance the critical current and reduce the electrical noise in the film. The YBCO film had its c-axis oriented perpendicular to the substrate.

The silicon nitride film underneath the YBCO was amorphous, causing the YSZ buffer layer to be polycrystalline (with its (111) axis oriented perpendicular to the substrate). Thus, it was not possible to grow epitaxial superconductor films on the Si$_3$N$_4$/YSZ buffer layers.

III. MICROBOLOMETER PROCESSING

After deposition of the YBCO film, a layer of YSZ 300 Å thick was deposited in-situ for passivation of the YBCO film during subsequent processing steps. The YBCO film was then patterned by ion milling. Silicon nitride passivation 7500 Å thick was then deposited over the YBCO and YSZ.

The first steps in forming contacts to the superconductor were to plasma etch the Si$_3$N$_4$ down to the top layer of YSZ

and to ion mill to remove the YSZ. Gold contact metal was then deposited onto the YBCO and patterned by lift off. The TiW/Au pad metal was then deposited and patterned. Finally, the underlying silicon was exposed by plasma etching through the Si₃N₄, and the silicon under the detector elements was etched from the frontside of the wafer (the side with the YBCO film) by immersing the wafer in a 45% solution of KOH in water at 85°C for about 1 hour.

An optical micrograph of one of the resulting microbolometers is shown in Fig. 1. The thermally isolated area sensitive to incoming radiation is 85 μm x 115 μm x 1.05 μm average thickness. Two legs support the sensitive region. These legs, visible in Fig. 1, are 100 μm long x 12 μm wide x 1.05 μm average thickness. The superconductor meander line is 4 μm wide and about 1100 μm long with a resistance of about 5500 Ω at 90 K.

$$R = \frac{I_{bias} r \beta \alpha}{G(1 + \omega^2 \tau^2)^{1/2}} \quad (1)$$

where I_{bias} is the bias current, r is the pixel resistance, $\beta = (dr/dT)/r$ is the temperature coefficient of resistance, α is the absorptance, G is the thermal conductance between the microbolometer and the heat sunk substrate, ω is the angular modulation frequency of the incident radiation, and τ is the pixel thermal time constant. The responsivity was measured using a 1000 K blackbody source illuminating the microbolometer through a sapphire window. The blackbody source was chopped at a frequency of 1.0 Hz. The dc bias current was 1 μA. During the measurement of resistance as a function of temperature, it was necessary to eliminate the 1.0 Hz modulation of the microbolometer temperature by half-covering the aperture of the blackbody source with a stationary blade of the chopper. As expected, the responsivity is proportional to the derivative of resistance with respect to temperature.
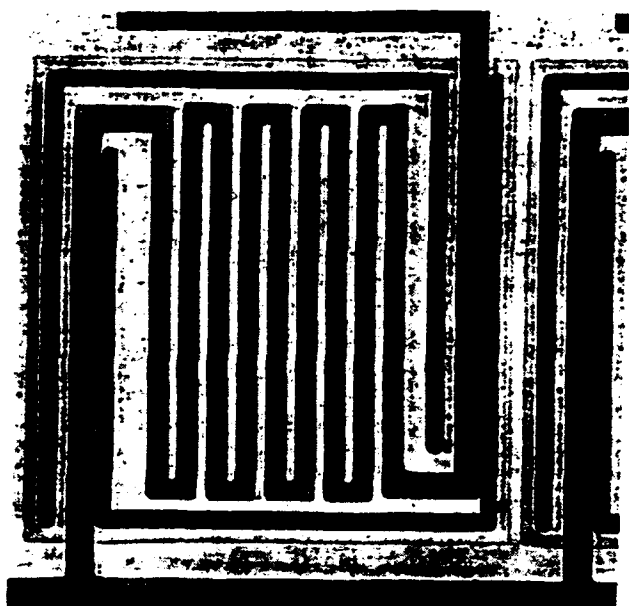

Fig. 1   Photomicrograph of one microbolometer in a 12-element linear array. The YBCO meander line is 4 μm wide. The two narrow black regions are openings into the etch pit.

Fig. 2   The resistance (o) and responsivity (▲) as functions of temperature for a microbolometer in a 12-element linear array, measured using a dc bias current of 1 μA.

IV. PERFORMANCE

The resistance as a function of temperature is shown in Fig. 2 for one microbolometer in a 12-element linear array. The resistive transition on the microbolometer is similar to that measured on freshly grown films deposited under similar conditions, indicating that the microbolometer processing steps have not caused significant damage to the YBCO. The resistance does not go to zero at low temperature because of contact resistance in the Au/YBCO contacts.

The infrared responsivity is also shown in Fig. 2. The responsivity is given by

The responsivity of nearly all the pixels in the 12-element linear array containing the microbolometers of Fig. 1 and Fig. 2 was close to that shown in Fig. 2. Fig. 3 shows the resistance as a function of temperature for seven thermally isolated microbolometers and one heat sunk meander line ("pixel #13") identical to the meander line on the microbolometers, and located adjacent to pixel #12. The 3 K temperature offset between the majority of the thermally isolated microbolometers and pixel #13 is due to heating of the of the microbolometers by thermal radiation from the walls of the cryostat and the sapphire window. It is not known why one of the microbolometers (pixel 6) shows a higher resistance than the others. The resistance as a function of temperature has been measured for eleven of the twelve pixels in the array
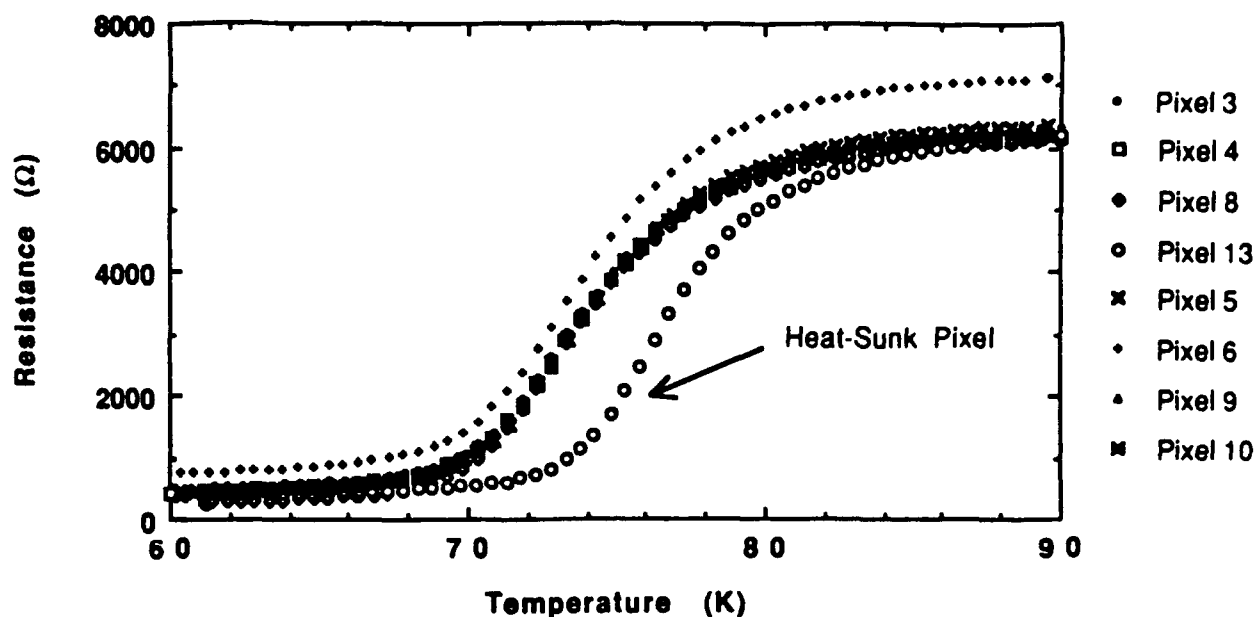
Fig. 3 Resistance as a function of temperature for seven of the microbolometers in a 12-element linear array, illustrating the pixel-to-pixel uniformity. Pixel #13 is a heat sunk YBCO meander line identical to the one on the microbolometers.

All of the measured pixels have nearly identical curves for resistance as a function of temperature, except pixel #6.

Measurements of responsivity as a function of frequency gave a thermal time constant of 24 msec. The thermal conductance, G, was measured by heating the microbolometer of Fig. 1 and Fig. 2 with several values of bias current and measuring the resistance change as a function of bias current. The temperature change was then inferred from the resistance change. At 72 K, the thermal conductance was measured to be 2.0×10^{-7} Watts/K. This is comparable to the value of 2.6×10^{-7} Watts/K measured at 95 K, well above the superconducting transition temperature. By using the relation $\tau = C/G$, the heat capacity, C, was calculated to be 4.8×10^{-9} Joules/K at 72 K.

The dc bias current of only 1 μA used to take the data of Fig. 2 causes a temperature rise of only 10 mK on the microbolometer. Much higher responsivity can be achieved by increasing the bias current and allowing the temperature of the microbolometer to increase substantially. For example, Fig. 4 shows the responsivity and resistance as functions of temperature when a bias current of 16 μA is used. The non-linear dependence of the maximum responsivity on bias current can be modeled as a decrease in the effective thermal conductance with increasing bias current due to self - heating of the microbolometer [4]. This decrease in effective thermal conductance also causes an undesirable increase in the thermal time constant. However, in a large FPA of microbolometers, a pulsed bias current several μsec long would be used to read out a microbolometer. In this case, large bias currents (of order 100 μA) could be used without significant self - heating. The responsivity would be proportional to bias current, with a temperature dependence given by the data of Fig. 2.
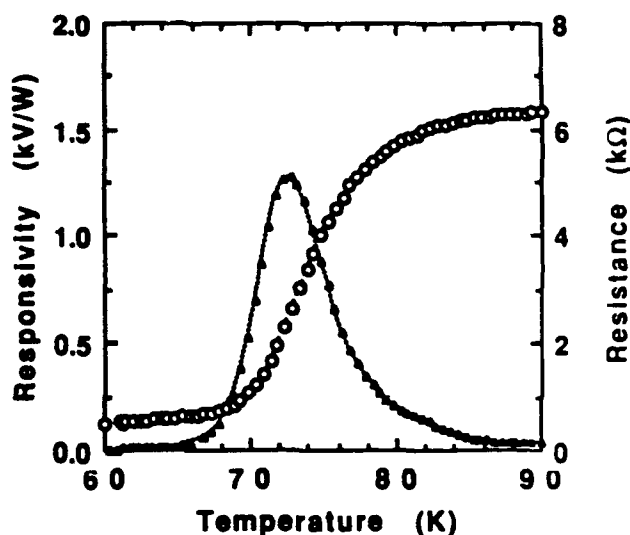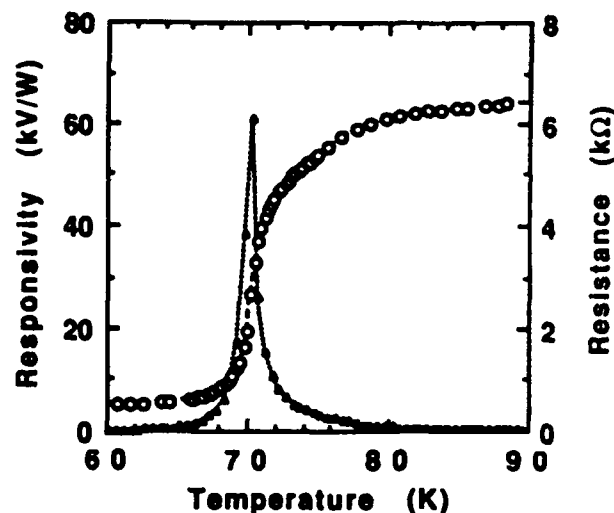

Fig. 4 The resistance (o) and responsivity (▲) as functions of temperature for a microbolometer in a 12-element linear array, measured using a dc bias current of 16 μA.

The noise in the microbolometers was dominated by noise in the Au/YBCO contacts. This was determined by comparing the microbolometer noise with the much lower noise voltage measured in a 4 - probe configuration in a patterned YBCO line 800 μm long and 4 μm wide. The patterned YBCO line was fabricated on the same wafer as the 12 - element linear array, and was located only 6 mm away from the array. The contact noise and the YBCO noise measured in the patterned line had a spectral density proportional to $1/f$ and I_{bias}^2, as expected for resistance fluctuation noise. Thus, the noise can be described by the Hooge formula [5]:

101

$$V_n^2 = \frac{\gamma \, I_{bias}^2 \, r^2}{n_c \, \Omega \, f} \quad (2)$$

where V_n^2 is the noise spectral density, γ is the dimensionless Hooge parameter, n_c is the density of charge carriers, Ω is the sample volume, and f is the frequency at which V_n^2 is measured. The noise spectral density was observed to be approximately independent of temperature in the transition region (except near where the resistance goes to zero, where there is a noise peak), despite the fact that the resistance is a strong function of temperature. Thus, Eq. 2 shows that the parameter $\gamma \rho^2/n_c$, where ρ is the resistivity, is approximately independent of temperature. This parameter is also independent of the sample geometry, and it incorporates n_c, so it provides a useful way to compare the 1/f noise in YBCO samples of various dimensions, or samples prepared by various methods, possibly in different laboratories. The value of $\gamma \rho^2/n_c$ was measured to be $1.0 \times 10^{-29} \, \Omega^2 \cdot cm^5$ for the YBCO in the patterned line. Eq. 2 was used to calculate the noise voltage in the YBCO in the microbolometers from the value of $\gamma \rho^2/n_c$ measured in the patterned YBCO line and the known dimensions of the meander lines in the microbolometers. The noise equivalent power (NEP) was calculated to be 1.3×10^{-12} Watts/Hz$^{1/2}$ at a frequency of 7 Hz, using a bias current of 1 μA (neglecting contact noise). This corresponds to a detectivity, D^*, defined as (detector area)$^{1/2}$/NEP, of 7.5×10^9 cm Hz$^{1/2}$/Watt (neglecting contact noise). The contact noise voltage is about ten times larger than the YBCO noise voltage in the microbolometers.

Using the data from the present superconductor microbolometers, the performance of an imaging system using a large FPA can be estimated. For this purpose, it was assumed that no improvements are made in the sharpness of the resistive transition of the YBCO, the resistivity of the YBCO, the noise of the YBCO, or the thermal conductivity of the materials used to support the microbolometer. The contact noise was assumed to be negligible. This should be achievable with straightforward improvements in the contact fabrication process [6]. The absorptance of the microbolometer over the 8 μm to 12 μm wavelength band was assumed to be 80%. The electronics readout noise was assumed to be similar to that of the present room temperature FPA's. The size of the microbolometers was assumed to be reduced to 50 μm x 50 μm, from the present 125 μm x 125 μm. The smaller size is close to that of the microbolometers in the existing imaging FPA's [1,2].

The noise equivalent temperature difference (NETD), defined as the temperature difference on an imaged scene required to produce a signal - to - noise ratio of 1 at the FPA, was calculated. With the above conservative assumptions, the NETD is calculated to be 7 mK for a FPA ▓▓▓▓▓▓ operating at a 30 Hz frame rate viewing a 300 K scene with F/1.0 optics in the 8 μm to 12 μm wavelength band. This value of NETD is comparable to that of HgCdTe imaging

systems. However, a YBCO microbolometer FPA on silicon would be significantly less costly to manufacture than HgCdTe two - dimensional staring arrays, especially for large arrays. In addition, the YBCO microbolometer, unlike HgCdTe, is a broadband detector with high sensitivity at long infrared wavelengths.

V. SUMMARY

Linear arrays of YBCO microbolometers have been fabricated by silicon micromachining. The high sensitivity of these devices and the fact that they are fabricated by relatively conventional silicon processing steps demonstrates the potential for fabricating a superconductor microbolometer staring focal plane array for IR imaging with performance comparable to HgCdTe staring arrays, but at much lower cost. Furthermore, the YBCO microbolometer is a broadband detector, so its performance is superior to HgCdTe detectors at long infrared wavelengths. Further improvements in responsivity and noise should be possible with improved YBCO films.

REFERENCES

[1] C.J. Han, R.A. Wood, B.E. Cole, R.E. Higashi, J. Holmen, J. Ridley, B. Johnson, D. Nielsen, "Uncooled Microbolometer IR Focal Plane Array", to be published in *Proceedings IRIS Passive Sensors 1992*.

[2] R.A. Wood, C.J. Han, P.W. Kruse, "Integrated Uncooled Infrared Imaging Arrays", in *IEEE Solid State Sensor and Actuator Workshop*, Hilton Head, South Carolina, June 1992, pp. 132-135.

[3] T.G. Stratton, B.E. Cole, P.W. Kruse, R.A. Wood, K. Beauchamp, T.F. Wang, B. Johnson, A.M. Goldman, "High - Temperature Superconducting Microbolometer", *Applied Physics Letters*, vol. 57, pp. 99-100, July 1990.

[4] P.L. Richards, J. Clarke, R. Leoni, Ph. Lerch, S. Verghese, "Feasibility of the High T_C Superconducting Bolometer", *Applied Physics Letters*, vol. 54, pp. 283-285, January 1989.

[5] F.N. Hooge, and A.M.H. Hoppenbbrouwers, "1/f Noise in Continuous Thin Gold Films", Physica vol. 45, p. 386 (1969)

[6] J.W. Ekin, "Ohmic Contacts to High-T_c Superconductors," in SPIE vol. 1187 *Processing of Films for High Tc Superconducting Electronics* (1989), pp. 359-364.

UNCLASSIFIED

Monolithic Silicon Focal Planes with High-T$_c$ Superconductor IR Sensors* (U)

B.R. Johnson, C.J. Han, R.E. Higashi, P.W. Kruse and R.A. Wood
Honeywell Sensor and System Development Center
Bloomington, MN 55420

This paper is UNCLASSIFIED in its entirety.

ABSTRACT

Silicon micromachining techniques have been employed to prepare single pixels and linear arrays of superconducting microbolometers. A thin film of the high transition temperature superconductor $YBa_2Cu_3O_{7-x}$ on a Si_3N_4 membrane over a Si etch pit provides a high temperature coefficient of resistance and excellent thermal isolation. When operated at 1 μA dc bias at 73°K, the D* is 7.5 x 10^8 cm Hz$^{1/2}$/W with a 24 msec thermal response time. Eliminating the noise from the contacts would increase the D* to 7.5 x 10^9 cm Hz$^{1/2}$/Watt. The NETD of a proposed staring focal plane array of superconducting microbolometers similar to Honeywell's HIDAD focal plane arrays is estimated to be 7 mK.

1.0 INTRODUCTION

The advent of silicon micromachining technology made possible the preparation of high performance staring focal plane arrays based upon thin film bolometers. Honeywell's HIDAD (High Density Array Development) program resulted in the development of an uncooled silicon microstructure staring focal plane array in which detection occurs in a semiconductor thin film.[1] Containing 80,000 pixels on a 50 μm pitch , Honeywell's HIDAD has a noise equivalent temperature difference (NETD) of 0.1°C when operated at 30 frames/sec with an f/1 lens.

Because the temperature coefficient of resistance of a superconductor near its superconducting transition temperature can be 100 times that of a semiconductor, a HIDAD-like superconducting microbolometer focal plane array can have an NETD in the millikelvin range. With the discovery of high-temperature superconductivity, it became theoretically possible to achieve such performance above liquid nitrogen temperature. Thus Honeywell began an effort under DARPA funding in 1988 to develop high-temperature superconducting microbolometer arrays employing $YBa_2Cu_3O_{7-x}$ on silicon microstructures.[2-5] The measured performance of linear arrays of such microbolometers is presented herein. Using these measurements, an estimate is made of the performance of a proposed two-dimensional focal plane array.

---

[1] R.W. Wood, et al., Silicon Uncooled Focal Planes for the High Density Array Development (HIDAD) Program, 1991 Meeting of the IRIS Specialty Group on Infrared Detectors, Boulder, CO, August 13-16, 1991.
2 T.G. Stratton, et al., Appl. Phys. Lett. 57, 99 (1990).
3 P.W. Kruse, SPIE Proceedings 1292, 108 (1990).
4 B.E. Cole, SPIE Proceedings 1394, 126 (1991).
5 B.R. Johnson, et al., SPIE Proceedings 1685 (1992).

UNCLASSIFIED

2.0 THEORY

The responsivity R of a bolometer is given by

$$R = \frac{i_b \alpha R_e \eta}{G(1 + \omega^2 \tau^2)^{1/2}} \quad ;$$

where i_b is the bias current, R_e is the electrical resistance, η is the optical absorptance, ω is the angular modulation frequency and G is the thermal conductance between the bolometer and the substrate. Here α, the temperature coefficient of resistance (TCR), is given by

$$\alpha = \frac{1}{R_e} \frac{dR_e}{dT} \quad ;$$

where T is the absolute temperature. The thermal time constant τ is given by

$$\tau = \frac{C}{G} \quad ;$$

where C is the heat capacity of the bolometer. Thus high responsivity is obtained at low frequencies by having a high TCR and a low thermal conductance. The heat capacity must be small such that the ratio of heat capacity to thermal conductance, i.e., the thermal time constant, meets the system requirements.

The detectivity D* is given by

$$D^* = \frac{R(A_D B)^{1/2}}{V_N}$$

where A_D is the detector area and V_N is the electrical noise in the bandwidth B. For imaging arrays, the appropriate figure of merit is the noise equivalent temperature difference, NETD, given by

$$NETD = \frac{(4F^2 + 1)V_N}{A_D \tau_o R(\Delta P / \Delta T)_{\lambda_1 \cdot \lambda_2}} \quad ;$$

where τ_o is the transmittance of the optics and $(\Delta P / \Delta T)_{\lambda_1 \cdot \lambda_2}$, is the rate of change of power per unit area with respect to temperature of a black body, measured between wavelengths λ_1 and λ_2. Within the 8-14 μm spectral interval the value for a 300°K blackbody is 2.62×10^{-4} Watts cm^{-2}(deg K)$^{-1}$.

The above expressions show that to have a small value of NETD for a given pixel size it is desirable to have a high responsivity, a fast lens, and low noise.

3.0 ARRAY DESIGN AND FABRICATION

The need for high responsivity dictates a pixel design providing high thermal isolation (low thermal conductance G). Honeywell's design employs a thin Si_3N_4 membrane upon which is a thin film of $YBa_2Cu_3O_{7-x}$. The membrane is connected laterally to the Si substrate by "legs" consisting primarily of Si_3N_4. The Si beneath the pixel is etched away so that heat flows from the membrane to the substrate only through the legs. Thus the thermal conductance G is controlled by the physical dimensions and thermal conductivity of the legs.

Fabrication of the arrays begins with a 3-inch diameter Si wafer upon which has been deposited a 3000Å thick layer of Si_3N_4. The wafers are then loaded into an ion beam sputtering system. A 600Å thick buffer layer of yttria stabilized zirconia (YSZ) is sputtered over the Si_3N_4. On this is then sputtered a 2000Å thick layer of $YBa_2Cu_3O_{7-x}$ at 735°C in an ozone and oxygen atmosphere. A small amount of Ag is co-sputtered with the $YBa_2Cu_3O_{7-x}$ to increase the superconducting critical current and reduce the noise. Finally, a 300Å thick layer of YSZ is sputtered over the $YBa_2Cu_3O_{7-x}$ to passivate it. Using conventional photolithographic techniques, and ion milling, the arrays are then patterned, each pixel incorporating a 4 μm wide serpentine of the $YSZ/YBa_2Cu_3O_{7-x}/YSZ$ structure. Over all of this is deposited a 7500Å thick Si_3N_4 film to provide further passivation and structural strength for the microstructure. Plasma etching and ion milling are employed to expose the $YBa_2Cu_3O_{7-x}$ on the electrical contact pads, upon which Au is then sputter deposited. Finally, the wafers undergo a KOH anisotropic etch which removes the Si underlying each pixel. Figure 1 illustrates one pixel of a 12-element linear array of 125 μm x 125 μm pixels having a thermally isolated area of 85 μm x 115 μm and an average thickness of 1.2 μm.

4.0 PERFORMANCE

Figure 2 illustrates the resistance vs temperature and the TCR vs temperature of one pixel of a 12-element linear array. All but one of the eleven pixels measured in this array have resistance vs temperature curves nearly identical to the one shown in Figure 2. Because Si_3N_4 is amorphous and YSZ is polycrystalline, the $YBa_2Cu_3O_{7-x}$ is polycrystalline (with the c-axis oriented perpendicular to the substrate). Thus the transition edge is not as steep as those seen in $YBa_2Cu_3O_{7-x}$ films deposited on lattice-matched single crystal substrates. However, if the transition edge is too steep, the dynamic range of the microbolometer will suffer and it will be difficult to stablize the temperature of the film at the midpoint of the transition. In addition, the temperature fluctuation noise increases as the transition edge becomes steeper (higher TCR). When the TCR is high enough that the temperature fluctuation noise is the dominant source of noise, there is no further improvement in performance with increasing TCR, because the signal and the noise are both proportional to the TCR. For a HIDAD-like focal plane array with a noise bandwidth of 100 kHz using superconducting microbolometers, the temperature fluctuation noise becomes equal to the Johnson noise for a TCR of only 0.3 K^{-1}. In such a system, increasing TCR beyond 0.3 K^{-1} gives a significant improvement in performance only if there is a large amount of 1/f noise or readout electronics noise. As shown in Figure 2, the present microbolometers exhibit a TCR of 0.3 K^{-1} near 72°K.

Figure 3 illustrates the responsivity at 1 μA bias as a function of temperature. The radiation source was a 1000°K black body irradiating the sample through a sapphire window using a 1 Hz chopper. A responsivity of 1300 V/W was obtained at 73°K with a

dc bias current of only 1 μA. At 16 μA bias the maximum responsivity increased to 62,000 V/W, see Figure 4. This nonlinear dependence of responsivity on bias current is caused by a bias-dependent sharpening of the transition edge due to self-heating of the microbolometer which reduces the effective thermal conductance.[6] In a large HIDAD-like focal plane array, a low duty cycle pulsed bias current would be used. In this case, very large bias currents (~100 μA) could be used without significant self-heating.

Noise measurements at 100 μA bias between 50 Hz and 1 kHz show a $1/f$ power law behavior. (For these measurements, the pressure in the cryostat vacuum can was increased so that the temperature rise of the microbolometer at the high bias current was negligible.) Two-probe and four-probe noise measurements on test structures on the same wafer show that most of the excess noise arises at the $Au/YBa_2Cu_3O_{7-x}$ contacts.

Frequency response measurements show a thermal time constant, τ, of 24 msec at 1 μA bias. The measured D^* for a 1 μA bias at 7 Hz (3 db rolloff frequency) is 7.5×10^8 cm $Hz^{1/2}$/W at 73°K. The noise measurements on the $YBa_2Cu_3O_{7-x}$ test structures indicate that eliminating the noise in the $Au/YBa_2Cu_3O_{7-x}$ contacts would increase D^* to about 7.5×10^9 cm $Hz^{1/2}$/W. The performance measurements are summarized in Table 1.

5.0   DISCUSSION

There are several straightforward ways in which the performance of the superconducting microbolometers can be improved. The contact resistance and contact noise can be greatly reduced by depositing gold for electrical contacts on the $YBa_2Cu_3O_{7-x}$ film immediately after the $YBa_2Cu_3O_{7-x}$ film is deposited.[7] The calculated optical absorptance of the present microbolometers is only 0.43. By using free space impedance matching absorbers (188 ohms/square) and antireflection films, the absorptance can be increased to greater than 80%. The thermal conductance can be reduced further by using microbolometer structures similar to those already being used in Honeywell's HIDAD program.

It will be very difficult to completely eliminate the $1/f$ noise in the $YBa_2Cu_3O_{7-x}$ films as long as the films are polycrystalline. The polycrystalline nature of the $YBa_2Cu_3O_{7-x}$ films is probably unavoidable without eliminating the amorphous Si_3N_4 layer that forms the lower surface of the thermally isolated structure. In Honeywell's HIDAD focal plane arrays, $1/f$ noise arising from the semiconductor film contributes little to the total noise because the noise bandwidth is ~100 kHz and the total noise over that entire bandwidth is largely Johnson noise. The noise bandwidth and Johnson noise of a staring focal plane array of superconducting microbolometers is expected to be similar to that of Honeywell's HIDAD arrays.

The development of the $YBa_2Cu_3O_{7-x}$ microbolometer linear arrays is intended as a first step in the development of a HIDAD-like staring focal plane array using superconducting microbolometers. The performance of such an array has been estimated using the measurements on linear arrays reported above. It was assumed that the material properties (thermal conductance, resistivity, TCR, transition temperature, and $1/f$ noise) of the $YBa_2Cu_3O_{7-x}$, YSZ, and Si_3N_4 are unchanged from those measured in the present

[6] P.L. Richards, J. Clarke, R. Leoni, Ph. Lerch, S. Verghese, Appl. Phys. Lett. 54, 283 (1989).

[7] J.W. Ekin, SPIE Proceedings 1187 359 (1989).

microbolometers. The shape of the microbolometers in the HIDAD-like array was assumed to be identical to that of the microbolometers in the present linear array, but the dimensions of the microbolometer were assumed to be scaled down to fit on a 50 μm pitch with a 50% fill factor. The operating conditions were assumed to be similar to that of Honeywell's HIDAD focal plane arrays: 100 μA pulsed bias current, 30 Hz framerate, 100 kHz noise bandwidth, f/1 optics, and absorptance of 80% over the 8 μm to 12 μm spectral interval. It was also assumed that noise from the readout electronics is similar to that of the HIDAD arrays. With these assumptions, the calculated NETD is 7 mK. Reducing the $1/f$ noise in the $YBa_2Cu_3O_{7-x}$ films would give an even lower NETD. An NETD of 7 mK is competitive with staring (Hg,Cd)Te focal plane arrays. In addition, the superconducting microbolometer focal plane arrays are expected to be less expensive than (Hg,Cd)Te focal plane arrays, because they are fabricated by Si processing.
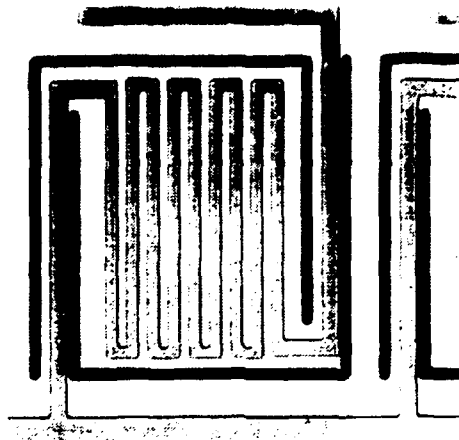
Figure 1
One Pixel of 12 Pixel Linear Array
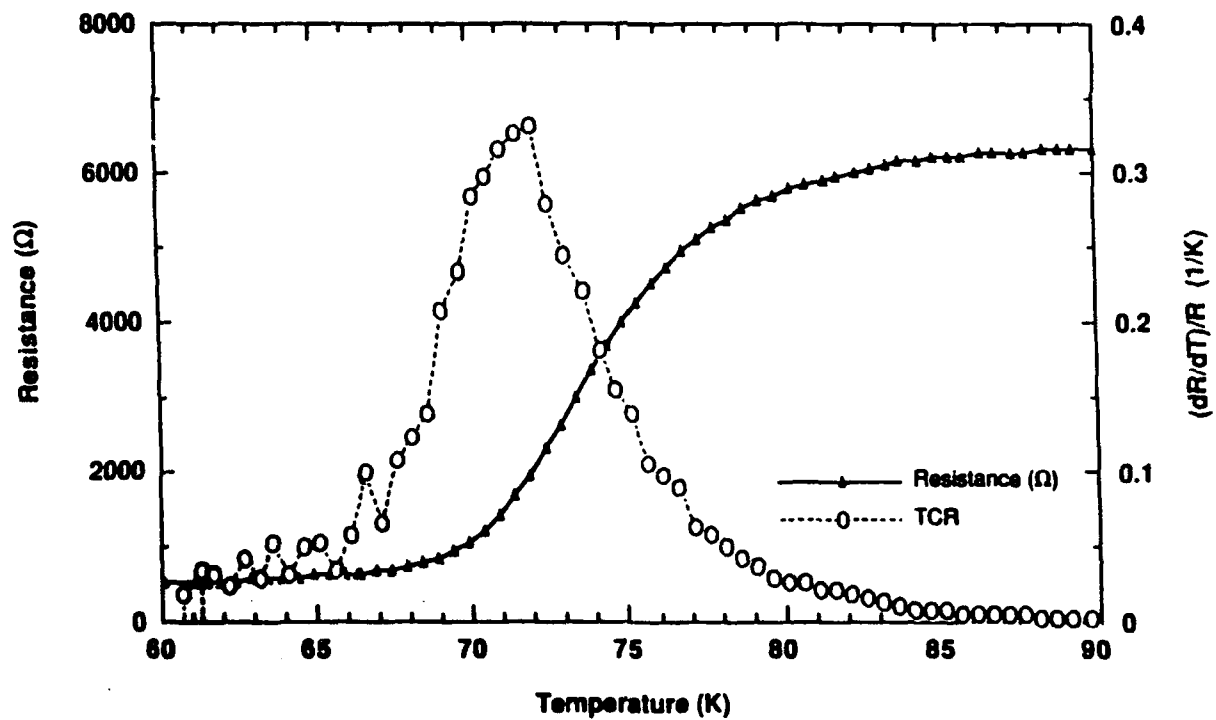
Figure 2
Resistance and TCR as Functions of Temperature
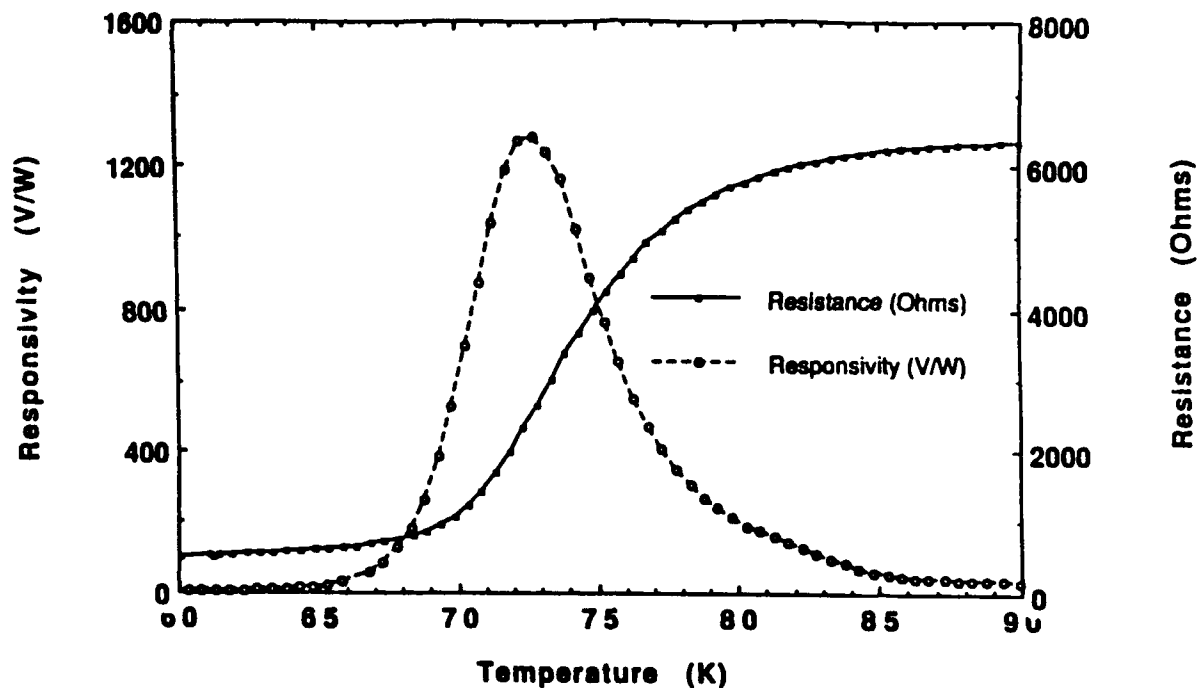**(1μA Bias Current)**

108

Figure 3
Resistance and Responsivity as Functions of Temperature
(1 μA Bias Current)
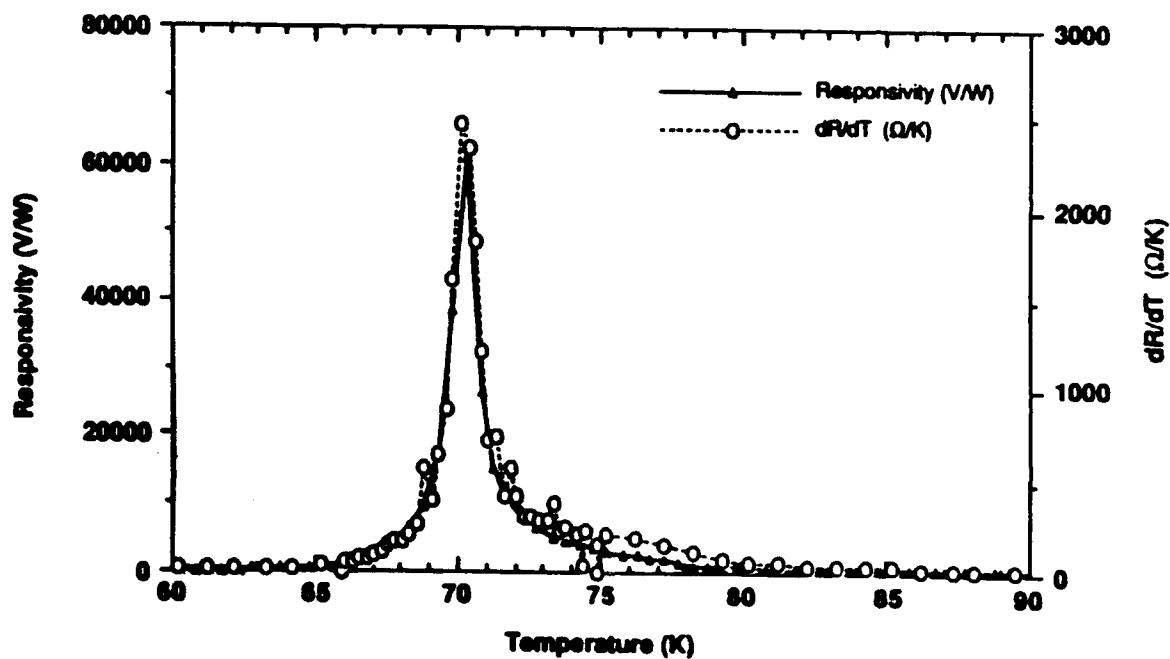
Figure 4
Responsivity and dR/dT as Functions of Temperature
(16 μA Bias Current)

109

Table 1

Measured Performance of One Pixel of 12-Element Superconducting Linear Array

Pixel area: 125 μm x 125 μm
Sensitive area: 85 μm x 115 μm

R = 1300 V/W at 1 μA bias at 73°K
   η = 0.43

D* = 7.5 x 10^8 cm $Hz^{1/2}$/W at 1 μA bias at 7 Hz modulation
   frequency. (Includes 10x excess noise from contacts).

τ = 24 msec at 1 μA bias
   G = 2 x 10^{-7} W/K
   C = 4.8 x 10^{-9} J/K

Appendix C
Theory of High T$_c$ Transition Edge Superconducting Microbolometers

NOTE: This Appendix, with minor modifications, is taken from the final report of DARPA/ONR contract #N00014-88-C-0394, "High Temperature Superconductor Film Development for Advanced IR Sensors," submitted September 14, 1991.

C.1 INTRODUCTION

A bolometer is an electrical resistor which detects electromagnetic radiation by changing its resistance in response to the temperature rise associated with the absorbed radiant power. It is a thermal detector, not a photon detector. That is, it responds to the energy content of the radiation rather than to the photon nature. A bolometer consists of two parts, the sensitive element and the substrate upon which it is mounted. Radiant power absorbed by the sensitive element causes its temperature to rise. Heat flows from the sensitive element to the substrate (assuming that the bolometer is in an evacuated enclosure and that radiant energy losses are negligible).

A microbolometer is a very small bolometer. Each microbolometer in an array of microbolometers is referred to as a pixel. A superconducting transition edge microbolometer is operated at the midpoint of the transition edge of the superconductor, i.e., where the resistance changes from the superconducting state to the normal state.

This appendix describes the theory of high-T$_c$ transition edge superconducting microbolometers including the results of a performance calculation for an imaging array of superconducting microbolometers. The theoretical principles will be discussed first, followed by design, construction and performance.

C.2 THEORY

The figures of merit commonly used to describe infrared detectors include the responsivity $\Re$ and detectivity D*. An additional figure of merit describing the performance of arrays is the noise equivalent temperature difference NETD. Each is discussed below.

Responsivity

The responsivity $\Re$ is the signal output per unit incident radiant power, usually expressed in Volts/Watt. The responsivity of any type of bolometer is given by

$$\Re = \frac{I_b \alpha R_e \eta}{G(1 + \omega^2 \tau^2)^{1/2}} \quad ; \tag{C.1}$$

where I_b is the bias current, R_e is the electrical resistance, η is the optical absorptance (fraction of the incident radiant power which is absorbed by the bolometer), G is the thermal conductance between the sensitive element and the substrate, ω is the angular frequency of modulation of the incident radiant, α is the temperature coefficient of resistance of the sensitive element and τ is the thermal time constant of the bolometer. Here

$$\alpha = \frac{1}{R_e} \frac{dR_e}{dT} \quad ; \tag{C.2}$$

where T is the absolute temperature, and

$$\tau = \frac{C}{G} \quad ; \tag{C.3}$$

where C is the heat capacity (thermal mass) of the sensitive element.

It can be seen from Eq. (C.1) that the responsivity is directly proportional to the temperature coefficient of resistance (TCR). Typical values of the TCR are as follows:

metals	0.002/deg C
semiconductors	0.02/deg C
high T_c Superconductors	2.0/deg C

The value listed above for the high T_c superconductor has been reported for a DyBaCuO film on a lattice-matched substrate at the midpoint (87 K) of the transition edge. Thus it can be seen that the responsivity of a high T_c transition edge superconducting microbolometer can be as much as 100 times greater than a semiconductor one.

Equation (C.1) also shows the responsivity to be inversely proportional to the thermal conductance between the sensitive element and the substrate. Honeywell has designed the superconducting microbolometer to have an extremely low thermal conductance. As described in the body of this report, this is achieved by depositing the high T_c superconducting film on a Si_3N_4 membrane suspended over an etch pit. Heat flows from the sensitive element through the membrane to the silicon substrate.

Equation (C.1) shows that at low modulation frequencies such that $\omega\tau \ll 1$ the responsivity is independent of frequency. At high modulation frequencies such that $\omega\tau \gg 1$, the responsivity is inversely proportional to frequency. The frequency response is thus controlled by the thermal time constant τ, given by Eq. (C.3). The value of τ is dictated by system design

considerations. Typically, two-dimensional arrays of infrared detectors used in military systems operate at 30 frames/sec, i.e., 30 Hz. Thus τ should be somewhat shorter than 1/30 sec. The value might be, say, 10 msec. In that case, the ratio of heat capacity (Joules/deg K) to thermal conductance (Watts/deg K) must be 0.01 sec. Clearly there are design tradeoffs which must be made to optimize the responsivity.

<u>Detectivity</u>

The detectivity D* of an infrared detector is given by

$$D^* = \frac{\Re(A_D B)^{1/2}}{V_N} \quad ; \tag{C.4}$$

where A_D is the detector area, B is the electrical bandwidth and V_N is the electrical noise within that bandwidth. Whereas $\Re$ is a signal voltage per Watt of incident power, D* is related to is the signal-to-noise ratio per Watt of incident power. To optimize D* it is necessary to have an analytic expression for the noise voltage V_N. If it is Johnson noise, the expression is

$$V_N = (4kTR_e B)^{1/2} \quad . \tag{C.5}$$

However, there may be excess noise near the midpoint of the transition, as discussed in Section 5 of this report. In that event, no simple expression exists for V_N.

The responsivity and detectivity of photon detectors depend upon wavelength. In that event, the wavelength λ is specified and they are written as $\Re_\lambda$ and D_λ^*. For thermal detectors including bolometers, the wavelength dependence enters through the absorptance η. As a first approximation, η is wavelength independent, so the responsivity and detectivity are written as $\Re$ and D*.

<u>Noise Equivalent Temperature Difference</u>

The noise equivalent temperature difference (NETD) describes the performance of an imaging system consisting of optics, focal plane array and readout electronics. The system views an extended area black body which fills the field of view, generating an electrical output characterized by a signal and signal-to-noise ratio. The NETD is the change in temperature of the black body which will change the output signal-to-noise ratio by unity. Expressed in deg K, the NETD is given by

$$NETD = \frac{(4F^2 + 1)V_N}{A_D \tau_o \Re(\Delta P / \Delta T_e)_{\lambda_1 - \lambda_2}} \tag{C.6}$$

where F is the f/no. of the optics, the transmittance of which is τ_0 and $(\Delta P / \Delta T_s)_{\lambda_1 - \lambda_2}$ is the rate of change with temperature of the radiant emittance of a blackbody of temperature T_s within the spectral interval between wavelength λ_1 and λ_2. For a 295 K blackbody within the 8-12 μm spectral interval, the value is 2.62 x 10^{-4} Watts/cm^2 deg K.

The importance of the responsivity, which describes the performance of one pixel, to an imaging array of pixels can be seen from Eq. (C.6). A high responsivity gives rise to a low NETD. Honeywell has calculated the performance of a superconducting microbolometer under the following conditions:

Array Size	:	240 x 336 pixels
Pixel Size	:	50 μm x 50 μm
Frame Rate	:	30 Hz
F/no.	:	1
α	:	0.3/deg K
$\lambda_1 - \lambda_2$	:	8 μm - 12μm
T	:	295 K
τ_0	:	0.9

Even with such a conservative value of α, the calculated value of the NETD is 0.004 deg K. This makes a superconducting microbolometer focal plane array superior to any cryogenic focal plane array currently in production and among the very best now under development.

C.3   DESIGN

Honeywell's design of the superconducting microbolometer employes concepts developed by Honeywell under a DARPA/CNVEOD program termed HIDAD (High Density Array Development). This program, which began in 1987, followed from an earlier one termed ASP, which began in 1985. They resulted in the development of uncooled staring focal plane arrays based upon semiconductor microbolometers prepared on silicon microstructures. Key to both ASP and HIDAD were the use of silicon wafer substrates with monolithic electronics. Silicon micromachining was used to delineate pixel structures with excellent thermal isolation. These structures consisted of a Si$_3$N$_4$ membrane over an etch pit (in the case of ASP), or a thin vacuum cavity produced by etching away a sacrifical layer (in the case of HIDAD). Ion beam sputtering was used to deposit the resistive media. These same considerations have been employed in Honeywell's development of the superconducting microbolometer.